UNIVERSITY OF CALIFORNIA

Los Angeles

High Transverse Momentum Charged Hadron Production in Au + Au Collisions at the Relativistic Heavy Ion Collider

A dissertation submitted in partial satisfaction

of the requirements for the degree

Doctor of Philosophy in Physics

by

Yu Chen

2003

The dissertation of Yu Chen is approved.

Gang Li

Ernest S. Abers

Charles A. Whitten Jr.

Huan Z. Huang, Committee Chair

University of California, Los Angeles

2003

To my very supportive family…

Especially, the three most important females in my life:

My daughter, coming into the world like an angel just in the beginning of the first RHIC/STAR data-taking period;

My wife, accompanying me in the United States without any reservation;

My mother, visiting us to provide her strong support in our busiest time.

TABLE OF CONTENTS

LIST OF FIGURES

LIST OF TABLES

ACKNOWLEDGMENTS

I would thank Professor Huan Z. Huang and Professor Charles A. Whitten Jr. for being the best advisors possible. Thanks also go to members of the UCLA Intermediate Energy Physics and Relativistic Heavy Ion Group: G. Igo, S. Trentalange, V. Ghazikhanian, O. Tsai, A. Tai, J. Kiryluk, H. Long, P. Sorensen, J. Wood, D. Thein, S. Guertin, J. Ma, J. Gonzalez, W. Dong, H. Jiang, and former graduate students S. Kelly and E. Yamamoto. I am grateful to and proud of having been a member of this very productive group for five years. Special thanks to Vahe Ghazikhanian for useful advice on my work on photomultiplier tube tests, to Oleg Tsai for helpful supervision on my work on wire tension tests and data analysis of Shower Maximum Detector beam test, and to An Tai for many helps on my thesis and paper writing and physics discussions. I would also like to thank C. Galgliardi, P. Jacobs, J. Dunlop, B. Choi, T. Ludlam, J. Klay, D. Hardtke, M. Miller, J. Gans, and other members of the STAR high p_T physics working group, and F. Wang, R. Snellings, Z. Xu, and other members of the STAR spectra physics working group for their helps with my analysis work. Thanks to T. Hallman, J. Thomas, N. Xu, A. Tang, H. Zhang, and the whole STAR Collaboration and the RHIC Operations Group.

VITA

26 May 1965	Born, Qionglai, Sichuan, The People's Republic of China
1986	B. S. in Physics Peking University Beijing, P. R. China
1989	M. S. in Physics Institute of High Energy Physics, Chinese Academy of Sciences Beijing, P. R. China
1989 — 1992	Assistant Research Institute of High Energy Physics, Chinese Academy of Sciences Beijing, P. R. China
1992 — 1998	Research Associate Institute of High Energy Physics, Chinese Academy of Sciences Beijing, P. R. China
1994	Visiting Associate California Institute of Technology Pasadena, California
1998 — 2003	Graduate Research Assistant University of California, Los Angeles Los Angeles, California
2001	The National Award of Natural Sciences, 2nd Class The State Council of the People's Republic of China
2002	The Phi Beta Kappa Alumni Award Alpha Association of Phi Beta Kappa Alumni in Southern California

PUBLICATIONS AND PRESENTATIONS

Chen Yu, Gu Yifan *et al.*, *Chinese Physics Letters* **10** (1993) 279, Dynamical Study of the Radiation Environment at the Interaction Region of BEPC.

Wang Dewu, Liu Jianfei *et al.*, *Journal of Synchrotron Radiation* **2** (1995) 113, Search for new scintillators by studying fluorescence properties of powered compounds with synchrotron radiation.

J.Z. Bai *et al.*, BES Collab., Phys. Lett. B **355** (1995) 374, A measurement of J/ψ decay widths.

J.Z. Bai *et al.*, BES Collab., Phys. Rev. Lett. **74** (1996) 4599, Direct Measurement of the Pseudoscalar Decay Constant, f_{D_s}.

J.Z. Bai *et al.*, BES Collab., Phys. Rev. D **53** (1996) 20, Measurement of the mass of the τ lepton.

BES Collab., *High Energy Physics and Nuclear Physics* **20** (1996) 481, Study of $\psi(2S)$ Decays into $\rho\pi$ and $K\bar{K}^*$.

J.Z. Bai *et al.*, BES Collab., Phys. Rev. Lett. **76** (1996) 3502, Study of $\xi(2230)$ in J/ψ Radiative Decays.

J.Z. Bai *et al.*, BES Collab., Phys. Rev. D **54** (1996) 1221, Search for a vector glueball by a scan of the J/ψ resonance.

J.Z. Bai *et al.*, BES Collab., Phys. Rew. Lett. **81** (1998) 5080, $\psi(2S)$ Hadronic Decays to Vector-Tensor Final States.

Chen Yu, Wang Zijing *et al.*, *High Energy Physics and Nuclear Physics* **23** (1999) 616, Charge Comparison Method Used to Discriminate Photons and Neutrons in Liquid

Scintillators.

K.H. Ackermann *et al.*, (J.H. Thomas for the STAR Collaboration), *Nucl. Phys.* A **661** (1999) 681c, The STAR Time Projection Chamber.

J.Z. Bai *et al.*, BES Collab., Phys. Rew. Lett. **84** (2000) 594, Measurement of the Total Cross Section for Hadronic Production by e^+e^- Annihilation at Energies between 2.6–5 GeV.

K.H. Ackermann *et al.*, STAR Collab., Phys. Rew. Lett. **86**, 402 (2001), Elliptic Flow in Au + Au Collisions at $\sqrt{s_{NN}} = 130$ GeV.

C. Adler *et al.*, STAR Collab., Phys. Rew. Lett. **87**, 112303 (2001), Multiplicity Distribution and Spectra of Negatively Charged Hadrons in Au + Au Collisions at $\sqrt{s_{NN}} = 130$ GeV.

C. Adler *et al.*, STAR Collab., Phys. Rew. Lett. **89**, 202301 (2002), Centrality Dependence of High-p_T Hadron Suppression in Au + Au Collisions at $\sqrt{s_{NN}} = 130$ GeV.

C. Adler *et al.*, STAR Collab., Phys. Rew. Lett. **90**, 032301 (2003), Azimuthal Anisotropy and Correlations in the Hard Scattering Regime at RHIC.

C. Adler *et al.*, STAR Collab., Phys. Rew. Lett. **90**, 082302 (2003), Disappearance of Back-To-Back High-p_T Hadron Correlations in Central Au + Au Collisions at $\sqrt{s_{NN}} = 200$ GeV.

‘Testing the Vector Glueball Hypothesis by an Energy Scan of $e^+e^- \to \rho\pi$ Cross Section across the J/ψ Resonance’, CCAST-WL Workshop Series: *Charm and* τ *Physics at BES/BEPC(I)*, Nov. 1992, Beijing, China.

‘Study on the ψ' Data Quality and New Measurement’, The BES Collaboration Meeting, Sep. 3, 1994, SLAC, Stanford, California.

‘Likelihood Ratio Method Used in Hypothesis Test’, The 1st National Symposium on High Energy Physics Experiment Technique, June 5–10, 1995, Guiyang, Guizhou, China.

‘Study of the “$\rho\pi$ Puzzle” in Charmonium Physics’, Invited Seminar, Sep. 25, 1997, Humboldt University, Berlin, Germany.

‘Are There Large Isospin–Violating Effects in Decays $\psi(2S) \to VP$?’, The 5th National Conference on High Energy Physics, April 21–25, 1998, Chengde, Hebei, China.

‘Systematic Studies of Number of Participants in Au+Au Collisions at RHIC Using STAR Data’, Poster Presentation P163, The 15th International Confenrence on Ultra–Relativistic Nucleus–Nucleus Collisions (Quark Matter 2001), Jan. 15–20, 2001, Long Island, New York.

‘Introduction to Empirical Determination of Collision Geometry and STAR High p_T Physics’, Invited Lecture, Summer School on *QCD & Experimental Physics Program at RHIC*, Aug. 24–27, CCAST, Beijing, China.

‘Systematic Study of High p_T Particles from Au + Au Collisions at $\sqrt{s_{NN}} = 130$ GeV’, DNP Fall Meeting of APS, Oct 9–12, 2002, East Lansing, Michigan.

‘Centrality and Pseudorapidity Dependence of High p_T Charged Hadron Production in Au + Au Collisions at $\sqrt{s_{NN}} = 130$ GeV’, APS Meeting, April 5–8, 2003, Philadelphia, Pennsylvania.

ABSTRACT OF THE DISSERTATION

High Transverse Momentum Charged Hadron Production in Au + Au Collisions at the Relativistic Heavy Ion Collider

by

Yu Chen
Doctor of Philosophy in Physics
University of California, Los Angeles, 2003
Professor Huan Z. Huang, Chair

Quantum Chromodynamics (QCD), the fundamental theory of the strong interaction, predicts a new state of matter called the Quark-Gluon Plasma (QGP). The Relativistic Heavy Ion Collider (RHIC) is dedicated to search for QGP in a laboratory/accelerator environment. The Solenoidal Tracker At RHIC (STAR) is designed to record high energy heavy ion collisions at RHIC. STAR is capable of measuring charged particles in high transverse momentum (p_T) region. High p_T hadrons can probe initial conditions of the collision system and nuclear effects in a dense and hot medium, which are critical in determining the deconfined QGP phase state.

STAR measurements of charged hadron production over a broad range of centrality in Au + Au collisions at center of mass energy per nucleon pair $\sqrt{s_{NN}} = 130$ GeV are presented. The measurements cover a phase space region of $0.2 < p_T < 6.0$ GeV/c in transverse momentum, $-1 < \eta < 1$ in pseudorapidity, and $0 \leq \phi < 2\pi$ in azimuthal angle. Inclusive transverse momentum distributions of charged hadrons in two pseudorapidity regions, $|\eta| < 0.5$ and $0.5 < |\eta| < 1$, are reported and compared with each other. We measured $dN/d\eta$ distributions, sum p_T, and mean p_T in the high p_T region

($p_T > p_T^{cut}$), which provide constraints to the collision dynamics for both longitudinal and transverse directions in the measured η region and suggest that an approximate boost invariant condition might be established in the early stage of collisions. High p_T hadron suppressions in central Au + Au collisions with respect to binary collision scaled $p+p$ and peripheral collisions are observed. Such a phenomenon is consistent with the picture of energy loss in a dense medium, suggesting that a dense matter, possibly partonic in nature, has been formed in the central Au + Au collisions at RHIC. The measurements are studied in the framework of participant scaling. The fractions of particles from hard processes extracted from two-component model in different p_T regions are obtained for various centralities, which demonstrate a suppression of hard process components in central collisions relative to $p+p$ and peripheral collisions. The STAR results are compared with model predictions; and the physics implications of these measurements are discussed.

CHAPTER 1

Introduction

Relativistic heavy ion collisions provide a unique opportunity to study the properties of highly excited hadronic matter under extreme conditions of high density and high temperature. It is generally believed that Quantum Chromodynamics (QCD) is the fundamental theory to describe and determine the equation of state of such highly excited nuclear matter. Lattice QCD indicates that when the distance scale of the strong interaction becomes comparable to the size of hadron, partons, the quark and gluon constituents of hadrons, will likely be deconfined to form a new state of matter called the Quark-Gluon Plasma (QGP). The phase transition from hadron matter to QGP can happen when the temperature is extremely high and/or when the baryon density is very large. This state of matter is believed to have existed in the early universe, about one microsecond after the Big Bang.

Motivated by QCD predictions and calculations of this new form of matter, scientists around the world have studied heavy ion collisions in which the conditions to form the QGP can be met in the laboratory. Results from the Alternating Gradient Synchrotron (AGS) at the Brookhaven National Laboratory (BNL) and the Super Proton Synchrotron (SPS) at the European Organization for Nuclear Research (CERN) have yielded some evidence which cannot be explained with existing models, for example, an excess for lepton pair production over Drell-Yan process, J/ψ suppression, and strangeness enhancement. But whether they constitute the signatures for the formation of QGP is still not universally agreed upon.

Currently, scientists are studying heavy ion collisions using the Relativistic Heavy Ion Collider (RHIC) at BNL. With center of mass energy per nucleon pair 10 times greater than previous heavy ion collisions and wider variability in the species of colliding particles, this machine offers greater opportunities in measuring the macroscopic properties of strongly interacting matter. In turn, the experimental results will help better determine the dynamics of the strong interaction and the conditions prevalent in the early universe.

This work concerns high transverse momentum (p_T) charged hadron production in Au + Au collisions at the center of mass energy per nucleon pair $\sqrt{s_{NN}} = 130$ GeV at RHIC using the Solenoidal Tracker At RHIC (STAR). The high p_T hadrons can be used to probe the initial conditions of collisions and nuclear effects in dense and hot medium. Following this introduction, the related physics will be introduced in Chapter 2. The Au + Au collision characteristics and the results from nucleon-nucleon collisions at the same energy are presented in Chapter 3. The STAR experimental setup is described in Chapter 4, and a detailed description of data analysis techniques is given in Chapter 5. In Chapter 6 results from the data analysis will be reported and compared with model calculations. Physics implications of the measurements are discussed in Chapter 7. In Chapter 8, we will summarize the presented results and physics conclusions. We provide the notations and definitions used in this dissertation for easy reference in Appendix A. In Appendix B, listed is a complete STAR Collaboration author list and scientific journal publications.

CHAPTER 2

Physics

2.1 QCD and QGP

Quantum Chromodynamics (QCD) is considered to be the underlying theory of the strong interaction, which governs hadron production in nuclear collisions. However, the strong interaction is not calculable from QCD when the momentum transfer in a process is small (soft process), though some limited calculations can be carried out numerically on the lattice (lattice QCD). For a scattering involving a high momentum transfer, perturbative methods can be applied in the QCD calculation (pQCD) due to the asymptotic freedom of the strong interaction. Such a process is related to hard-scattering of partons (hard process) and is believed to be responsible for hadron production in $p+p$ collisions at high transverse momentum (p_T), typically above ~ 2 GeV/c [Owe78, App79]. The hard processes occur in the early stage of a high energy collision and the partons from the hard processes fragment later into jets of hadrons. The production and properties of jets have been extensively studied in elementary collisions in the past two decades and have been used as a test of perturbative QCD [Ban82, Arn83, Abe89]. The transverse energy dependence of the inclusive differential jet cross sections in the central pseudorapidity region from pp and $p\bar{p}$ interactions is shown in Fig. 2.1, in which the solid curves represent Next-to-Leading order (NLO) QCD predictions for $p\bar{p}$ interactions at center of mass energy $\sqrt{s} = 630$ GeV and $\sqrt{s} = 1.8$ TeV [Hag02].

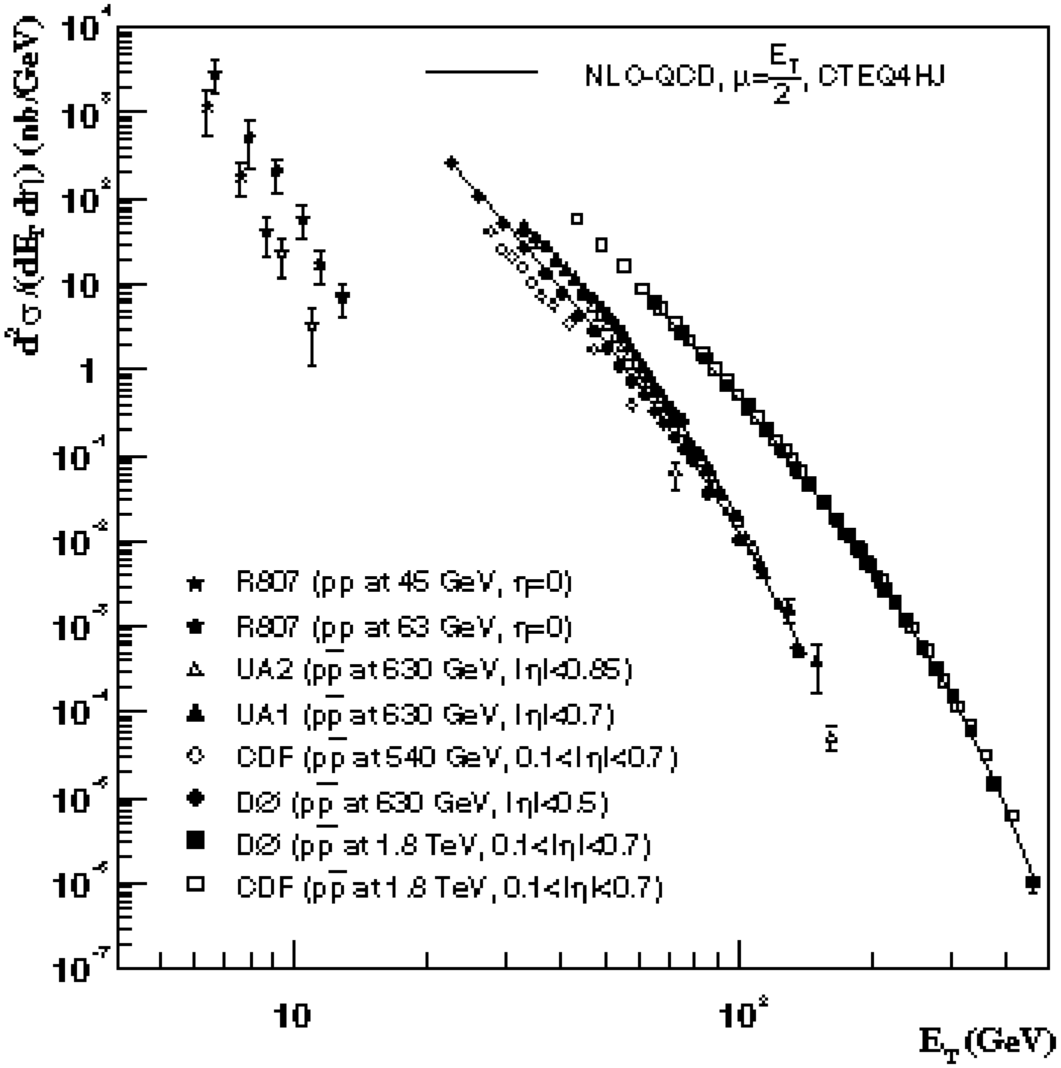

Figure 2.1: Transverse energy dependence of the inclusive differential jet cross sections in the central pseudorapidity region. Curves are NLO pQCD predictions for $p\bar{p}$ at 630 GeV and 1.8 TeV. This figure is taken from the Review of Particle Physics by Particle Data Group [Hag02].

The lattice QCD calculation [Cle86] for a stable and large system of vanishing net baryon density shows the existence of a deconfined phase of the quarks and gluons called the Quark-Gluon Plasma (QGP). The calculation consistently predicts that a phase transition from hadronic matter to the QGP will occur at a temperature of the order of $T_c = 150$ MeV, which corresponds to an energy density of 1–3 GeV/fm^3. Fig. 2.2 shows QCD phase diagram. In the early universe, the confinement transition occured at high temperature and very low baryon density. The QGP phase may exist in the present universe in the cores of neutron stars. In a laboratory/accelerator environment, such a phase transition can be achieved by increasing the energy density (heating and/or increasing the density of nuclear matter) of nucleus-nucleus collisions as shown in Fig. 2.2.

2.2 Nucleus-Nucleus Collisions

2.2.1 Collision Dynamics

The main goal of heavy ion physics is to search for the QGP phase transition in nucleus-nucleus (AB or AA) collisions. The dynamics of such a collision can be viewed from a different perspective in the space-time evolution diagram as shown in Fig. 2.3. Typically, a high energy, head-on nucleus-nucleus collision would go through the following stages: initial conditions, QGP formation, phase transition from QGP to hadron gas, freezout including chemical and kinetic freezeout. Following the initial impact of incoming nuclei, a region of hot and dense matter is generated. The interaction region immediately begins to expand longitudinally and transversely so that the highest energy density (therefore the best opportunity to form a QGP) is achieved early in the collision. With further expansion and cooling the matter hadronizes and forms a dense, interacting hadron gas. When the temperature drops to a level that the inelas-

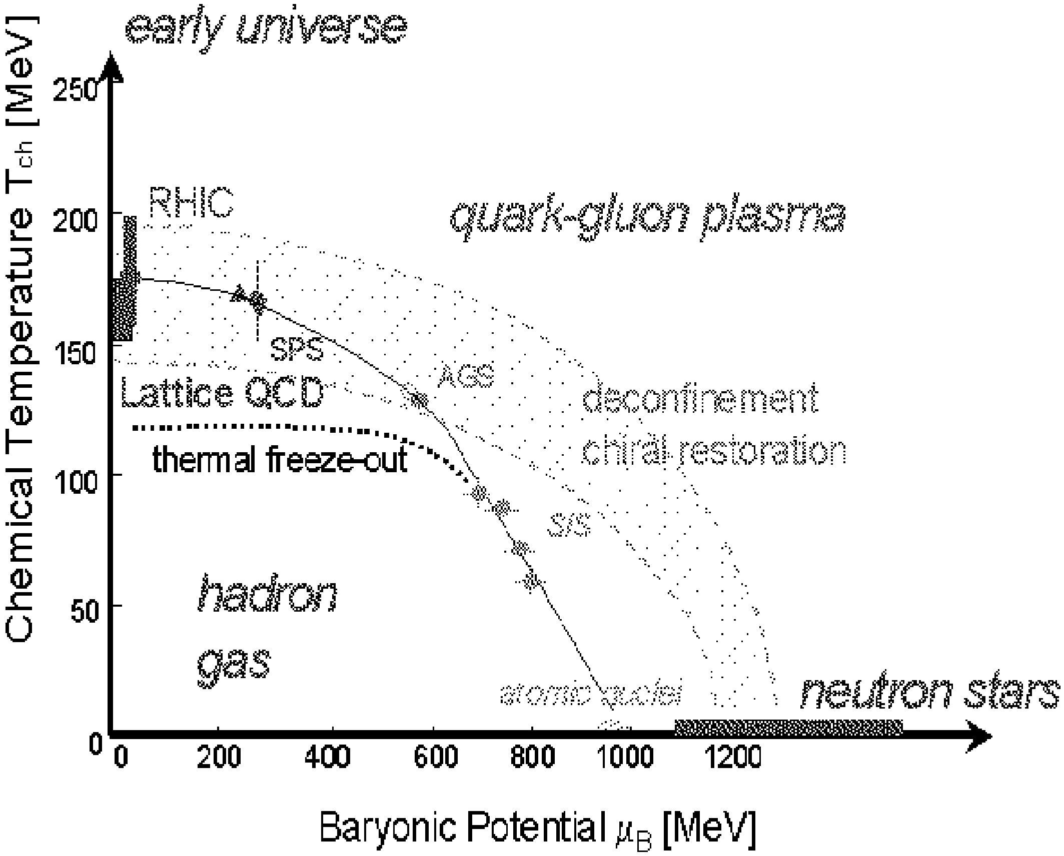

Figure 2.2: QCD phase diagram. The major features of QCD phases possibly accessible in nature and heavy ion collisions are shown.

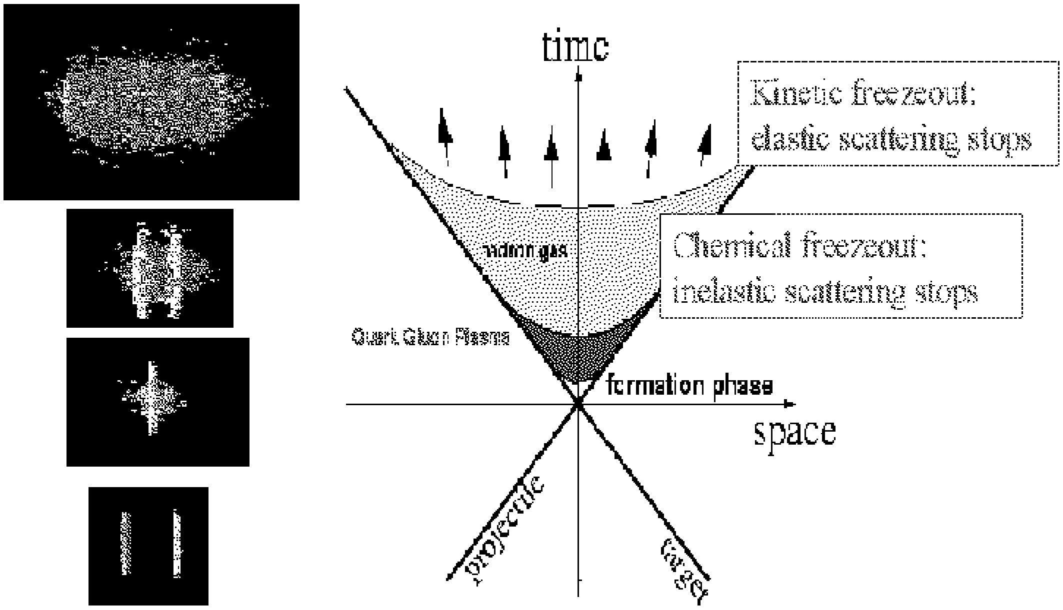

Figure 2.3: Space-time picture of a nucleus-nucleus collision.

tic scattering between hadrons stops, the system has reached chemical freezeout and the relative population of various final state hadron species is established. After the further expansion and cooling the system has reached kinetic freezeout as the elastic scattering among hadrons stops, and the final momentum spectra of hadrons observed in detectors are established.

Previous AGS and SPS experiments have made efforts to search for the signatures of QGP formation. However, with the increase of a order of magnitude of collision energies, the Relativistic Heavy Ion Collider (RHIC) experiments at the Brookhaven National Laboratory have opened a new era to investigate properties and evolution of matter at high temperature and energy density formed during nucleus-nucleus collisions. At RHIC energies, the hard processes become more important in comparison to previous heavy ion experiments and the hard scattering processes could be used to probe the early state of the collision system.

2.2.2 Two Components

The two-component model is one of the pQCD-inspired models, in which the hadron multiplicity contains the sum of yields from the soft processes and hard processes in nucleus-nucleus collisions. The soft processes are assumed to scale with the number of participant nucleons, N_{part}, and the hard processes are assumed to scale with the number of binary nucleon-nucleon (NN) collisions, N_{coll} [Wan02b, KN01]. i.e.,

$$dN/d\eta = (1-x)n_{pp}N_{part}/2 + xn_{pp}N_{coll}, \tag{2.1}$$

where n_{pp} and x are the hadron multiplicity and the fraction of hard processes in $p+p$ collisions, respectively. The fraction of hard processes in AA collisions is thus defined by

$$F = \frac{xn_{pp}N_{coll}}{dN/d\eta}. \tag{2.2}$$

In the two-component model, the momentum transfer of the soft processes is treated phenomenologically and the hard processes are calculated by pQCD. Theoretically, when one calculates the fraction of hard processes, a p_T^{min} needs to be introduced to avoid the infrared divergence of perturbative QCD calculations. Thus, the definition of hard processes depends on the choice of p_T^{min}.

2.2.3 Nuclear Modification Factor

In the absence of any nuclear effects, the production rate of hard processes is proportional to N_{coll} as represented in Eq. 2.1. Therefore, any nuclear medium effects in AA collisions with respect to NN collisions can be quantified by the deviation from unity of nuclear modification factor, which is defined as the N_{coll} scaled ratio of p_T spectra, or

$$R_{AA}(p_T) = \frac{d^2N_{AA}/dp_Td\eta}{T_{AA}d^2\sigma_{NN}/dp_Td\eta}, \tag{2.3}$$

where $T_{AA} = N_{coll}/\sigma_{in}$ accounts for the AA collision geometry, and σ_{in} is the inelastic cross section of NN collisions. The other term in the denominator of Eq. 2.3 is the p_T spectrum in NN collisions.

Novel nuclear effects in nucleus-nucleus collisions are of particular interest because they reveal the properties of the collision system and the collision dynamics. Three nuclear effects are discussed in next section. The Cronin effect, parton shadowing are considered as initial state effects while jet quenching is related to final state effect.

2.3 Nuclear Effects

2.3.1 Cronin Effect

In the middle 70's it was discovered by Cronin et. al. [Cro75] that high p_T particle production in proton-nucleus (pA) collisions is enhanced beyond simple binary collision scaling. Traditionally this enhancement, now called Cronin effect, had been parameterized as $\sigma_{pA} = A^{\alpha(p_T)}\sigma_{pp}$. A compilation of the p_T-dependent exponent $\alpha(p_T)$ from different fixed target experiments [Ant79, Gar77, Cha79, Fri83] is given in Fig. 2.4. For minimum bias pA collisions, the number of binary collisions $N_{coll} = A$, therefore, the enhancement $\alpha = 1.1$ at intermediate $p_T \sim 2-4$ GeV/c corresponds to the nuclear modification factor $R_{pAu} = 1.7$ for p+Au collisions since $R_{pA} = \sigma_{pA}/(N_{coll}\sigma_{pp}) = A^{(\alpha-1)}$ and $A_{Au} = 197$.

The Cronin effect has also been observed in heavy ion collisions. Data taken in

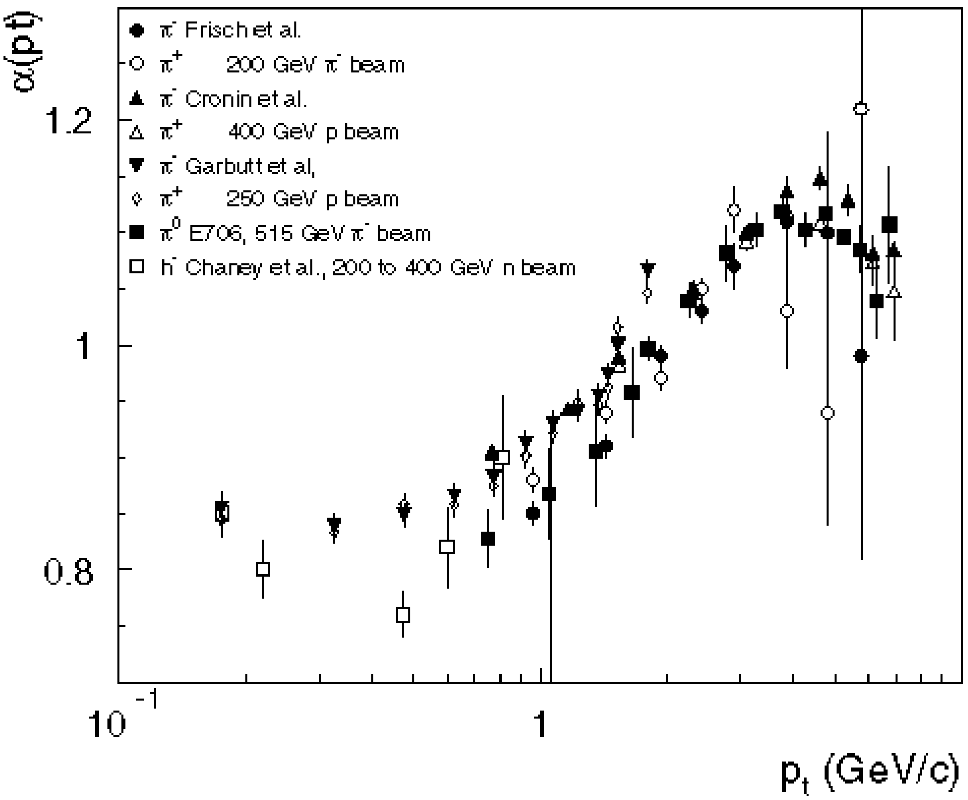

Figure 2.4: Compilation of data for the Cronin exponent $\alpha(p_T)$. The excess above binary scaling, the "anomalous nuclear" enhancement, sets around 2 GeV/*c* when $\alpha(p_T)$ increases above unity.

$\sqrt{s} \simeq 17$ GeV Pb-Pb and Pb-Au collisions at CERN-SPS [Agg98, App99, Aga00] are compiled and analyzed in terms of the nuclear modification factor [WW01a] and shown in Fig. 2.5. R_{AA} continuously increases, crosses unity around 1.5 GeV/c and eventually saturates above 2 GeV/c at a value of $R_{AA} \sim 2$. It is commonly accepted that the Cronin effect originates from initial state multiple parton scattering and a similiar behavior is expected in higher energy collisions although the effect could become smaller when the original jet spectra become much flatter.

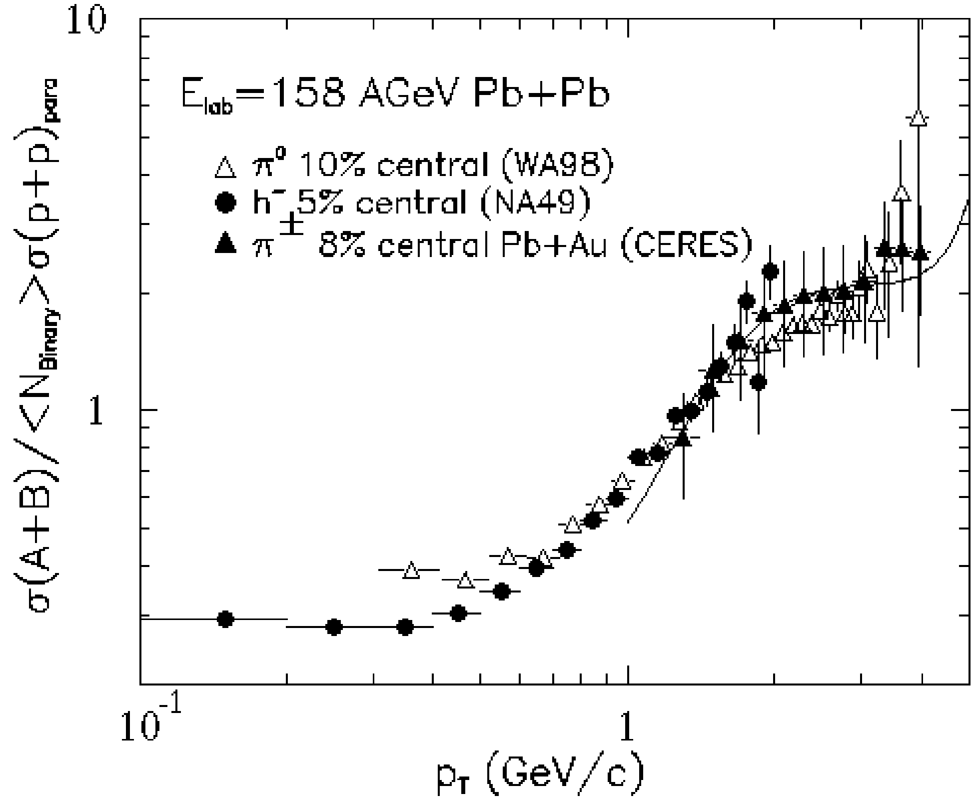

Figure 2.5: Nuclear modification factors for charged and pion data in AB collisions at SPS energy. The curve is a model calculation in [WW01a].

2.3.2 Parton Shadowing

Another important initial state effect is parton shadowing, or the modification of parton distribution functions (PDFs) inside nuclei. From deep inelastic lepton-nucleus scattering [Arn90], it is well known that the quark structure functions with small fractional momenta are depleted in a nucleus relative to a free nucleon. This depletion, usually referred to as nuclear shadowing, is also expected for the gluon structure function although there is no clear experimental evidence for that yet. There are some data derived from the evolution of quark distribution. Gluon shadowing is of interest in high energy nucleus-nucleus collisions because it could influence significantly the initial conditions in reactions with high gluon density [WG92]. A recent parameterization of the modification of the parton distributions is given by Eskola, Kolhinen, and Salgado (EKS) [EKS99] based on global fits to the most recent collection of data available and some modeling for the nuclear modification of the gluon distribution. The EKS parameterization is quite different from the HIJING parameterization [WG91, LW02]. In the EKS parameterization, the QCD evolution equation has been used to take into account the momentum transfer scale dependence of the nuclear modification, an effect which is not treated in the HIJING parameterization. The EKS parameterization also has a gluon antishadowing which is larger than any previous parameterizations.

Fig. 2.6 is taken from [Wan00] which demonstrates how the shadowing (antishadowing) affects charged hadron spectra. The nuclear modification factor R_{pAu} at RHIC energy without shadowing (solid curve) is similar to those at lower energies. The Cronin enhancement is still about 20–50% and then disappears at larger p_T. In the HIJING parameterization (dash-dotted curve), the gluon shadowing is assumed to be identical to that for quarks, reducing the hadron spectra in pA collisions significantly in the intermediate p_T range. On the other hand, hadron spectra in a large p_T range at the RHIC energy mainly come from fragmentation of gluon jets, and the gluon antishadowing becomes relevant, leading to an extra enhancement of hadron spectra (dashed curve).

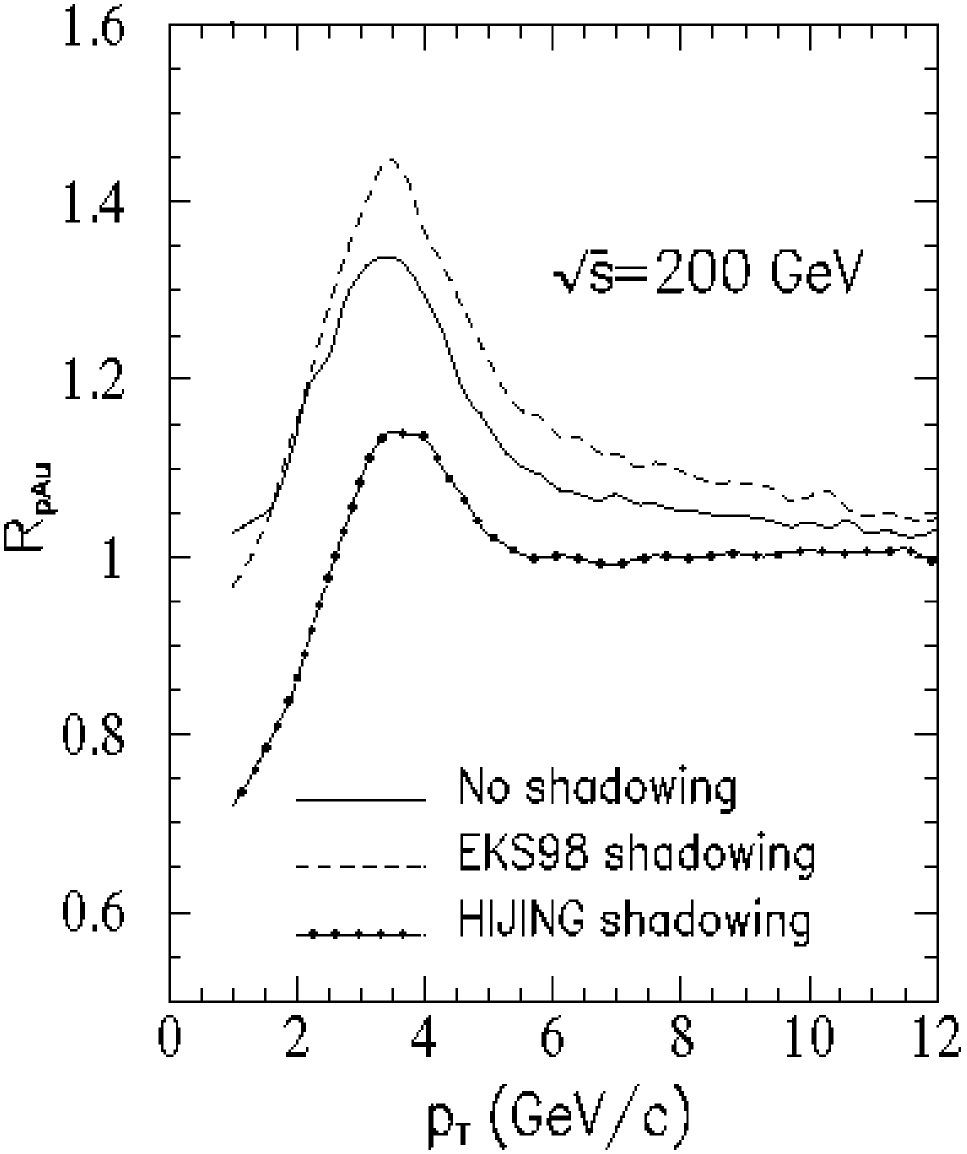

Figure 2.6: Predictions of the ratio of charged hadron spectra in $p+Au$ over $p+p$ collisions normalized by the number of binary collisions at $\sqrt{s}=200$ GeV. The different lines are for different parameterizations of shadowing.

2.3.3 Jet Quenching

It has been predicted that a high energy parton (jet) would lose energy in the hot/dense medium through gluon bremsstrahlung and multiple scatterings before its hadronization into observed hadrons [GP90, Bai95, WG92, Wan98], leading to a suppression of high p_T hadron production. This final state partonic energy loss in nuclear medium, dE/dx, is called “jet quenching”. It was also pointed out that the magnitude of the energy loss provides an indirect signature of QGP formation since the parton energy loss is directly proportional to gluon density in the early stage of the formed medium and the energy loss would be much larger in the partonic medium than in hadronic matter [BSZ00, WW02].

Jets are not easy to reconstruct directly among the large number (an order of 10^3) of produced particles in the final state of a heavy ion collision. However, one of the jet fragments will always carry a major fraction of the jet momentum. These so-called leading particles manifest themselves in a power-law shape of the transverse momentum distribution. If jets are quenched, a depletion of the high energy tail in the p_T spectrum is expected. In addition, since jets are produced through parton-parton hard scatterings, azimuthal correlations between high p_T particles from a single jet fragmentation (same side) or two scattered partons (away side) might also serve as an experimental observable.

Fig. 2.7 is also taken from [Wan00] which shows the nuclear modification factor R_{AA} in central Au+Au collisions at RHIC energy with and without parton energy loss. This figure demonstrates that the parton energy loss would dramatically suppress the charged hadron p_T spectrum in central high energy heavy ion collisions.

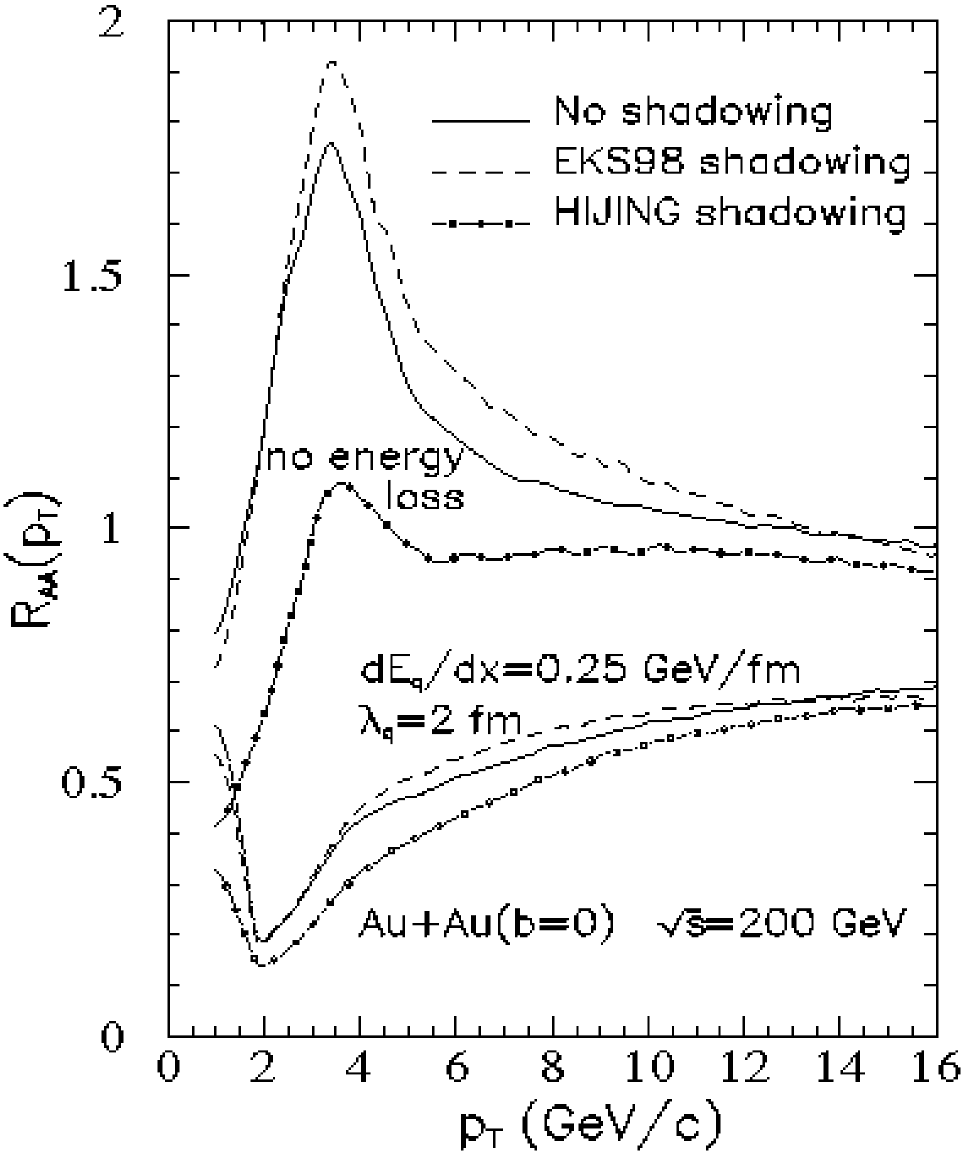

Figure 2.7: Predictions of the ratio of charged hadron spectra in central $Au + Au$ over $p + p$ collisions normalized by the number of binary collisions at $\sqrt{s_{NN}} = 200$ GeV. The different lines are for different parameterizations of shadowing. The upper set of lines is without parton energy loss and the lower set is with parton energy loss $dE_q/dx = 0.25$ GeV/fm and mean free path $\lambda_q = 2$ fm [Wan00].

2.4 High p_T Hadron Production

In this section we focus on hard processes in nuclear collisions and present pQCD-inspired parton model calculations to demonstrate how the various nuclear effects are treated in the pQCD models.

2.4.1 $p+p$ Collisions

In the absence of final state interactions the well-known lowest order invariant differential cross section for inclusive $p+p \to h+X$ is given by

$$\begin{aligned} E_h \frac{d\sigma_h^{pp}}{d^3p} &= K \sum_{abcd} \int dx_a dx_b f_{a/p}(x_a, Q_a^2) f_{b/p}(x_b, Q_b^2) \\ &\quad \times \frac{d\sigma}{d\hat{t}}(ab \to cd) \frac{D_{h/c}(z_c, Q_c^2)}{\pi z_c}, \end{aligned} \tag{2.4}$$

where $x_a = p_a/P_A$, $x_b = p_b/P_B$ are the initial momentum fractions carried by the interacting partons, $z_c = p_h/p_c$ is the momentum fraction carried by the final observable hadron, $f_{\alpha/p}(x_\alpha, Q_\alpha^2)$ is the parton distribution function (PDF) of the parton of flavor α in a nucleon, and $D_{h/c}(z_c, Q_c^2)$ is the fragmentation function (FF) for the parton of flavor c into hadron h.

The differential cross section of parton hard scattering process, $\frac{d\sigma}{d\hat{t}}(ab \to cd)$, can be more precisely calculated by pQCD at leading order (LO) of the strong coupling constant α_S. The phenomenological K factor is introduced to mimic higher order corrections, usually $K \approx 2$. The initial state PDFs and final state FFs are obtained using a factorization scheme of the parton's QCD evolution (e.g., DGLAP) to fit experimental measurements. Several parameterizations of PDF and FF exist, among which, CTEQ [Pum02], MRST [MRS02], and GRSV [GRS01] are most popularly used for parton distribution functions, and KKP [KKP00], BKK [BKK95], Kretzer [Kre00], and BFGW [BFG01] are for fragmentation functions.

One finds that Eq. 2.4 tends to underestimate the hadron spectra. This can be partially corrected via the initial k_T smearing of partons. The k_T here denotes the transverse momentum of partons. The initial k_T distribution is assumed to have a Gaussian form

$$g(k_T) = \frac{e^{-k_T^2/\langle k_T^2\rangle}}{\pi\langle k_T^2\rangle}, \tag{2.5}$$

where the width $\langle k_T^2\rangle$ is related to initial state radiation.

2.4.2 $p+A$ Collisions

In $p+A$ collisions, the Cronin effect is attributed to the initial state multiple parton scattering, which provides an additional k_T kick, leading to nuclear k_T broadening, $\langle\Delta k_T^2\rangle_A$. Therefore, the initial parton k_T distribution inside a projectile nucleon going through the target nucleon becomes

$$g_A(k_T) = \frac{e^{-k_T^2/\langle k_T^2\rangle_A}}{\pi\langle k_T^2\rangle_A}, \tag{2.6}$$

with a broadened width

$$\langle k_T^2\rangle_A = \langle k_T^2\rangle + \langle\Delta k_T^2\rangle_A. \tag{2.7}$$

The invariant inclusive hadron distribution in proton-nucleus (pA) collision can thus be given by

$$E_h\frac{dN_h^{pA}}{d^3p} \quad = \quad K\cdot T_A(b)\sum_{abcd}\int dx_a dx_b \int d^2k_a d^2k_b g_A(k_a) g(k_b)$$

$$\times S_A(x_a,Q_a^2)\, f_{a/A}(x_a,Q_a^2)\, f_{b/p}(x_b,Q_b^2)$$
$$\times\frac{d\sigma}{d\hat{t}}(ab\to cd)\frac{D_{h/c}(z_c,Q_c^2)}{\pi z_c}. \tag{2.8}$$

Here, $T_A(b)$ is nuclear overlap integral at impact parameter b, and $T_A(b)=N_{coll}/\sigma_{inel}$, σ_{inel} is the inelastic nucleon-nucleon cross section and N_{coll} is the number of binary collisions. For minimum biased $p+A$ collisions, $N_{coll}=A$. $S_A(x_a,Q_a^2)$ is the nuclear modification of parton a distribution, $f_{a/A}(x_a,Q_a^2)$, inside nucleus A, which acounts for the nuclear shadowing and antishadowing effects. The deep inelastic lepton-nucleus scattering experiments provide sets of data to extract those modifications. The well-known parameterization of the modifications for the PDFs is EKS [EKS99]. Recently, HKM has also published their parameterization results [HKM01].

2.4.3 $A+A$ Collisions

The effect of final state parton energy loss on the attenuation pattern of high p_T partons in nuclear collisions is attributed to the modification of the fragmentation function. Energy loss of the parton prior to hadronization changes the kinematic variables of the effective fragmentation function. Including multigluon fluctuations of the energy loss via an energy loss distribution $P(\varepsilon,E)$ where $\varepsilon=\sum_i\omega_i/E$ is the fractional energy loss of a jet of energy E in the rest frame of the plasma and ω_i is the jet energy loss for each scattering, the mean energy loss in the first approximation is related to P via

$$\int_0^\infty d\varepsilon P(\varepsilon,E)\varepsilon=\Delta E/E. \tag{2.9}$$

The invariant hadron distribution attenuated by fluctuating energy loss in nucleus-

nucleus (AB) collision is then given by

$$\begin{aligned} E_h \frac{dN_h^{AB}}{d^3p} &= K \cdot T_{AB}(b) \sum_{abcd} \int dx_a dx_b \int d^2k_a d^2k_b g(k_a) g(k_b) \\ &\times S_A(x_a, Q_a^2) S_B(x_b, Q_b^2) f_{a/A}(x_a, Q_a^2) f_{b/B}(x_b, Q_b^2) \\ &\times \frac{d\sigma}{d\hat{t}}(ab \to cd) \int_0^1 d\varepsilon P(\varepsilon) \frac{z_c^*}{z_c} \frac{D_{h/c}(z_c^*, Q_c^2)}{\pi z_c}, \end{aligned} \tag{2.10}$$

where $z_c^* = z_c/(1-\varepsilon)$. Here, $T_{AB}(b)$ is nuclear overlap integral at impact parameter b.

2.5 Parton Energy Loss

In this section, we will summarize most currently available pQCD models which incorporate final state partonic energy loss mechanisms.

2.5.1 VG Model

In this model [VG02, Vit03], Vitev and Gyulassy calculate the distribution $P(\varepsilon, E)$ of the fractional energy loss of a fast parton with energy E in the thin plasma opacity expansion framework GLV [GLV00] where the longitudinal Bjorken expansion is taken into account via the plasma (gluon) density $\rho(\tau) = (\tau_0/\tau)\rho_0$ where τ_0 is the proper time of plasma formation and ρ_0 is the initial plasma density at the formation time τ_0, and $\tau_0\rho_0 = (1/\pi R_A^2) dN^g/dy$ relates to the gluon rapidity density dN^g/dy produced in central A+A collisions. Using the GRV parameterization (previous version of GRSV) for the PDFs, BKK parameterization for the FFs, and the EKS parameterization for the nuclear modification (shadowing and antishawdowing) to the PDFs, the main results for central Au+Au collisions are shown in Fig. 2.8. At RHIC energy, the p_T-independent $R_{AA}(p_T)$ predicted for $dN^g/dy \sim 800-1200$ results from the competition of three nuclear effects. None of the nuclear effects alone would lead to such a flat suppresseion.

2.5.2 Wang Model

In Wang's model [Wan03], the MRS parameterization (previous version of MRST) for the PDFs, the BKK parameterization for the FFs, and the new HIJING parameterization [LW02] for the nuclear modification to the PDFs are used. The parton energy loss is calculated via a detailed balance theory [WW01b]. The corresponding energy loss in a static medium with a uniform gluon density ρ_0 over a distance R_A is $dE_0/dL = (R_A/2\tau_0)\langle dE/dL\rangle_{1d}$, where $\langle dE/dL\rangle_{1d}$ is the average parton energy loss over the distance R_A in a 1-d Bjorken expanding medium with the initial gluon density ρ_0; and an effective quark energy loss

$$\langle\frac{dE}{dL}\rangle_{1d} = \varepsilon_0(E/\mu_0 - 1.6)^{1.2}/(7.5 + E/\mu_0), \tag{2.11}$$

is used from the numerical results in [WW01b] with parameters $\mu_0 = 1.5$ GeV, $\varepsilon_0 = 1.07$ GeV/fm, and $\lambda_0 = 1/(\sigma\rho_0) = 0.3$ fm. The calculated nuclear modification factors for hadron spectra in Au+Au collisions at $\sqrt{s_{NN}} = 200$ GeV are shown in Fig. 2.9.

The flat p_T dependence of the π^0 suppression is a consequence of the strong energy dependence of the parton energy loss. The slight rise of R_{AA} at $p_T < 4$ GeV/c in the calculation is due to the detailed balance effect in the effective parton energy loss.

2.5.3 JJS Model

The JJS model [JJS03] calculates neutral pion spectra to NLO with a pQCD prediction using NLO MRS PDFs, BKK FFs, and EKS shadowing. Initial k_T smearing is not included since they restrict their calculation to the $p_T > 3$ GeV/c region. They

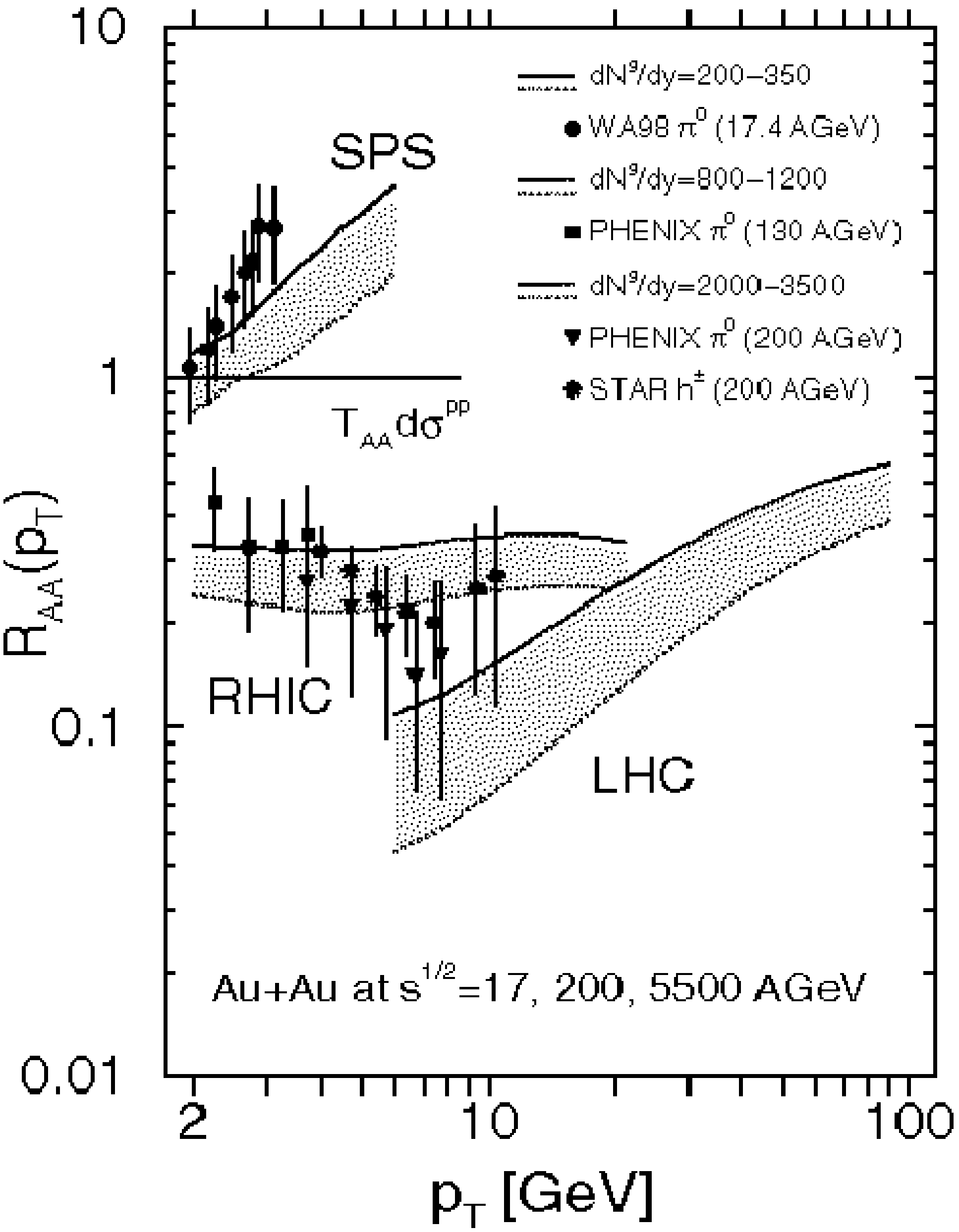

Figure 2.8: Predictions of R_{AA} in the VG model for neutral pions in central Au+Au collisions at $\sqrt{s_{NN}} = 17$, 200, and 5500 GeV. Solid (dashed) lines correspond to the smaller (larger) effective initial gluon rapidity densities at a given $\sqrt{s}$ that drive the parton energy loss.

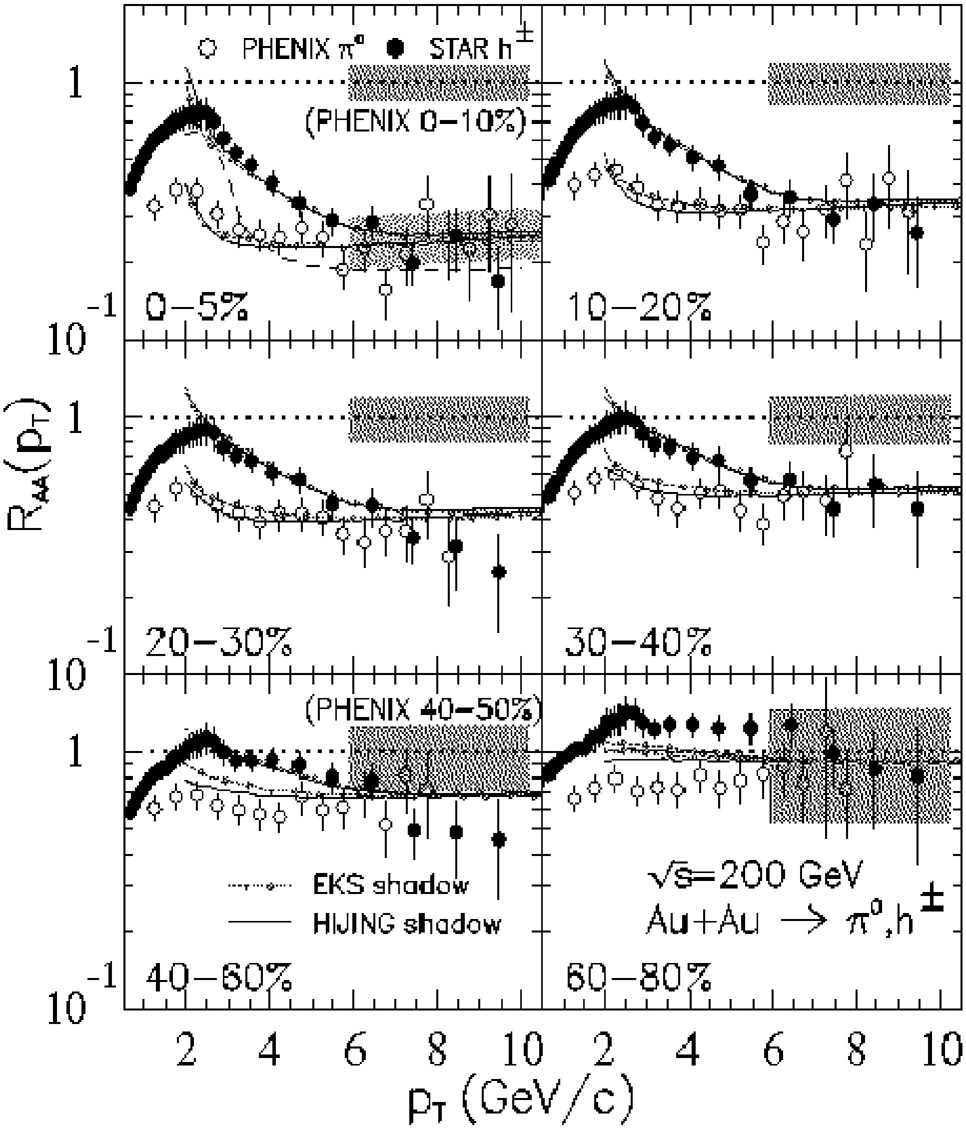

Figure 2.9: Hadron suppression factors calculated in the Wang model for charged hadrons and neutral pions in $Au+Au$ collisions at $\sqrt{s_{NN}} = 200$ GeV.

consider three cases of parton energy loss:

1) constant parton energy loss per parton scattering, $\varepsilon = const$,

2) Landau-Pomeranchuk-Migdal (LPM) energy-dependent energy loss, $\varepsilon \sim \sqrt{E}$,

3) Bethe-Heitler (BH) energy-dependent energy loss, $\varepsilon = \kappa E$.

Given the inelastic scattering mean-free-path, λ, the probability for a parton to scatter n times within a distance ΔL before it escapes the system is assumed to be given by the Poisson distribution. The effective fragmentation function is therefore modified by energy shift ε at each scattering. Mean number of scatterings is $\langle n \rangle = \Delta L/\lambda$, and $\lambda = 1$ fm, $\Delta L = R_A$ (nuclear radius).

The predictions of R_{AA} for inclusive π^0 production at $\sqrt{s_{NN}} = 200$ GeV for different choices of parton energy loss parameter ε are plotted in Fig. 2.10. For both constant and LPM energy loss, the ratio increases with p_T, while for the BH case, the ratio slightly decreases with p_T, and is very sensitive to the fraction of energy loss per scattering, κ.

2.5.4 Müller Model

Müller derives an analytical expression for the quenching (suppression) factor in the strong quenching limit where the p_T spectrum of hard partons is dominated by surface emission [M03]. It is assumed that effective energy loss, defined as the shift of the momentum spectrum of fast partons, depends on p_T and the static medium thickness, L, in the following general way:

$$\Delta p_T = \eta p_T^{\mu} L, \tag{2.12}$$

where μ is a scaling exponent. Three scaling laws are discussed:

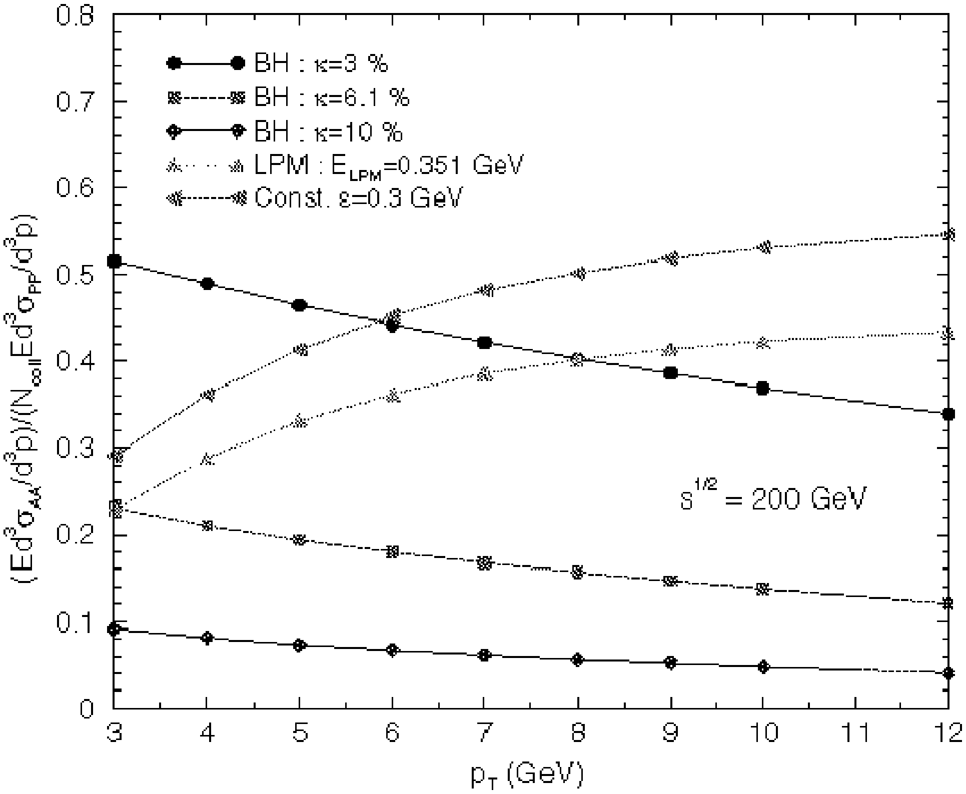

Figure 2.10: Ratio of inclusive π^0 cross sections predicted in the JJS model in $Au+Au$ collisions and in $p+p$ collisions at $\sqrt{s_{NN}} = 200$ GeV.

1) BDMS: $\Delta p_T = \eta' L_{eff}\sqrt{\rho(r,0)p_T/\nu}$, where L_{eff} is an effective medium thickness and η' is a constant.

2) Bethe-Heitler (BH): $\Delta p_T = \eta p_T (L\rho)_{eff}$, corresponding to $\mu = 1$.

2) Random Walk (RW): $\Delta p_T = \eta p_T \sqrt{(L\rho)_{eff}}$.

The predictions of the quenching factor Q with its dependence on the transeverse momentum of the fast parton in central Au+Au collisions at $\sqrt{s_{NN}} = 200$ GeV for different scaling laws are shown in Fig. 2.11. The QCD-motivated BDMS law (solid line) and the other scaling laws exhibit clearly different behaviors. This reflects the different p_T scaling of the energy loss in these models (linear for BH and RW, square-root for BDMS), in agreement with the conclusions from the JJS model in which the linear parton energy dependence is for BH and the square-root energy dependence for LPM.

The centrality depenedence of the quenching factor is shown in Fig. 2.12, plotted as the yield per half number of participant nucleons against the paticipant number. The ratios fall for the BDMS and BH laws as the collision centrality increases. An approximately flat behavior is found for the RW scaling law.

2.5.5 PY Model

The parton energy loss may also be studied from the pseudorapidity dependence of hadron production. Pseudorapidity, η, is defined by (see also Appendix A)

$$\eta = 0.5 \ln\left(\frac{p + p_z}{p - p_z}\right). \tag{2.13}$$

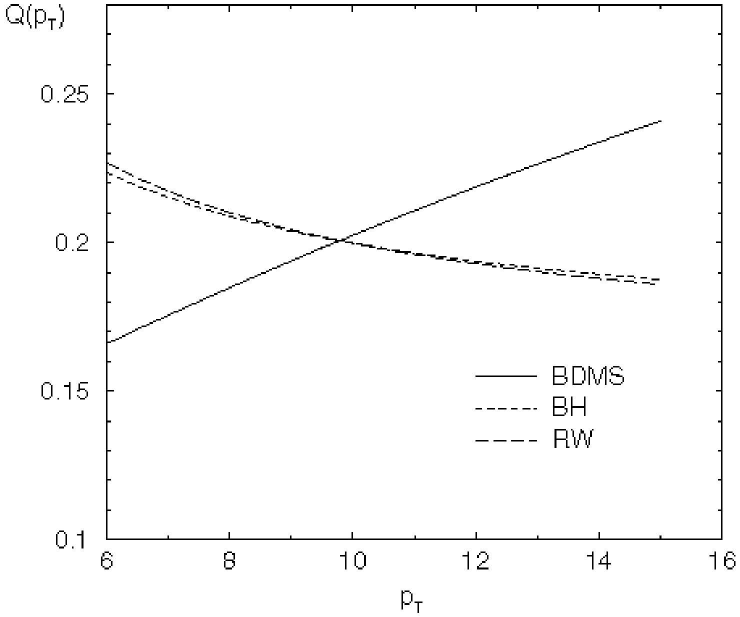

Figure 2.11: Dependence of quenching factor Q on p_T for central collisions in the Müller model. The parameter η is chosen such that $Q(p_T) \approx 0.2$ for $p_T = 10$ GeV/c in each case. The scaling laws (BH, RW) exhibit stronger quenching with increasing p_T, in contrast to the BDMS law.

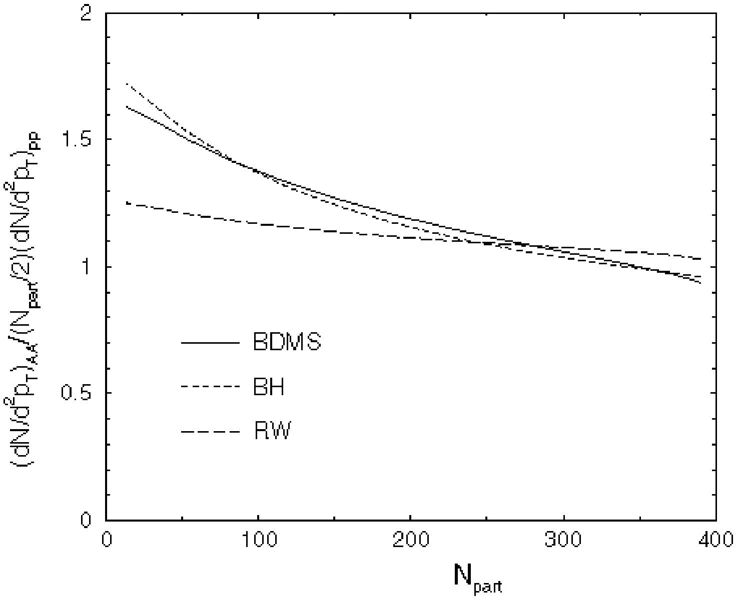

Figure 2.12: Quenched hard parton yield divided by $N_{part}/2$ as a function of N_{part} for $p_T = 10$ GeV/c in the Müller model. The values of the stopping power strength parameters are $\eta = 0.06$ (RW), $\eta = 0.017$ (BH), and $\eta' = 1.1$ (BDMS).

Change of pseudorapidity due to change of momentum is

$$\delta\eta = \frac{p_z}{p}\left(\frac{\delta p_z}{p_z} - \frac{\delta p_T}{p_T}\right). \tag{2.14}$$

The pseudorapidity distributions would be modified as a result of the parton energy loss if the momentum change rate ($\delta p/p$) due to the energy loss is different along the transverse and longitudinal direction.

The medium density depends on both centrality and (pseudo)rapidity. Because jet energy loss is proportional to the density of the local medium, at different rapidities the energy loss for a jet of fixed p_T will be different, and the large p_T hadron spectrum from jet fragmentation will also have different behavior. In their model, Polleri and Yuan [PY01] used the GRV parameterization for the PDFs, the KKP parameterization for the FFs, and the EKS parameterization for the nuclear modification to the PDFs. The k_T broadening effects on both initial and final jet spectra were taken into account. In order to study the rapidity dependence of parton energy loss, they simply assume that the parton energy loss is proportional to the parton energy E and the rapidity density of medium dn/dy, or

$$\Delta E(y,E) = qE\frac{dn}{dy}, \tag{2.15}$$

where q is a parameter in the model. For simplicity, they assume that the plasma density at the early stage is proportional to the measured rapidity density of charged hadrons, therefore including both soft and hard produced particles. The time evolution of the plasma due to geometric and dynamical effects is not taken into account.

Numerical results from the PY model with the parameter $q = 0.27$ are shown in Fig. 2.13 and Fig. 2.14. Fig. 2.13 shows the predictions of the transverse momentum dependence of R_{AA} in central Au+Au collisions (impact parameter $b = 0$) for different

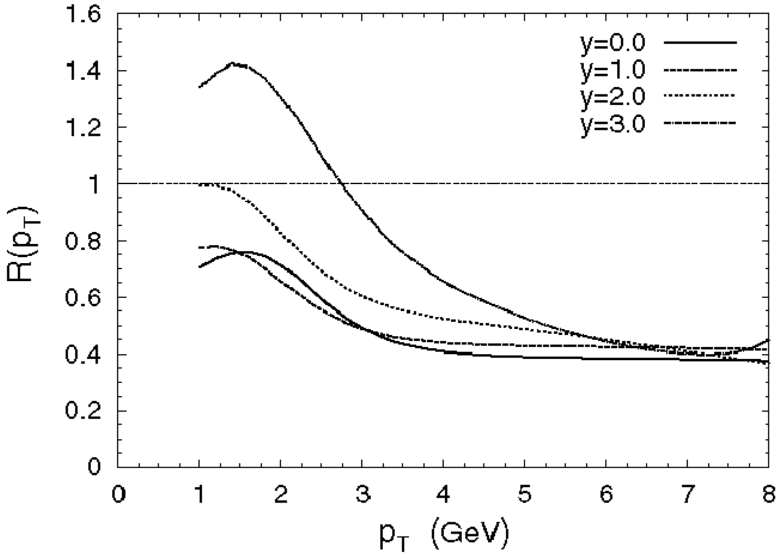

Figure 2.13: Transverse momentum dependence of R_{AA} predicted in the PY model in central Au+Au collisions at $\sqrt{s_{NN}} = 200$ GeV for different rapidity values.

rapidities at $\sqrt{s_{NN}} = 200$ GeV. The suppression at larger y is reduced, as expected, due to the decrease in the medium density. Especially, at very large rapidity one can really observe the Cronin effect. Fig. 2.14 shows the predictions of the rapidity dependence of the R_{AA} at different values of p_T. At large p_T, a presence of a concavity around mid-rapidity is predicted.

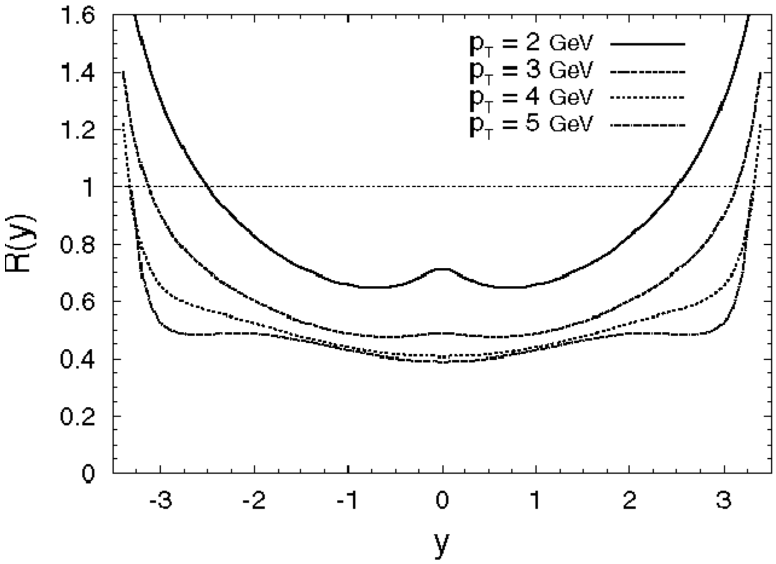

Figure 2.14: Rapidity dependence of R_{AA} predicted in the PY model in central Au+Au collisions at $\sqrt{s_{NN}} = 200$ GeV for different transverse momentum values.

CHAPTER 3

NN Reference and Collision Geometry

In this chapter, we will present first how to obtain a nucleon-nucleon reference spectrum, and then how to calculate N_{coll} in Au + Au collisions, all of which constitute of the denominator in Eq. 2.3.

3.1 *NN* Reference

3.1.1 Extrapolation

In the absence of any NN collision data at $\sqrt{s} = 130$ GeV, a NN reference spectrum is obtained by extrapolation of the UA1 $\bar{p} + p$ data at $\sqrt{s} = 200 - 900$ GeV [Alb90]. The UA1 inclusive p_T spectra were fit by the pQCD inspired power law function [Alb90]

$$\frac{1}{2\pi p_T}\frac{dN}{dp_T} = C(1 + \frac{p_T}{p_0})^{-n}. \tag{3.1}$$

The fit parameters were used to extrapolate to our energy, $\sqrt{s} = 130$ GeV, giving $C\sigma_{in} = 267^{+4}_{-6}$ mb/(GeV/c)^2, $p_0 = 1.90^{+0.17}_{-0.09}$ GeV/c, and $n = 12.98^{+0.92}_{-0.47}$ at $\sqrt{s} = 130$ GeV [Adl02a]. The superscripts and subscripts are curves that bound the systematic uncertainty.

We listed this NN spectrum in Table 3.1. The first column is the p_T interval which we used everywhere in this analysis. The second column is the p_T point in the corresponding p_T bin. In a bin with large width, the correct point for variable x is neither the bin center x_c nor the weighted mean value $\bar{x}$ within the bin but a solution x_{lw} [LW95] to

$$f(x_{lw}) = \frac{1}{\Delta x}\int_{x1}^{x2} f(x)dx, \tag{3.2}$$

where $x1$, $x2$ are lower, upper edges of the bin and the bin width $\Delta x = x2 - x1$, and $f(x)$ is the density distribution function of the variable x. This assumes no significant variation in efficiency over the bin. In most of cases, $\bar{x} < x_{lw} < x_c$. In our case, $f(x)$ is the expected power law function of the p_T distribution. There is slight difference between the p_T points calculated in this way for different spectra in the same p_T bin. For example, in the p_T bin of 5.1 – 6.0, $p_T = 5.477$ GeV/c for the most central bin and $p_T = 5.489$ GeV/c for the most peripheral bin in Au + Au collisions. The $d^2\sigma_{NN}/dp_T d\eta(|\eta| < 2.5)$ is listed in the third column, and the lower (-) and upper limits of its systematic uncertainty are listed in the forth and fifth columns and are shown as percentages.

It is worthwhile to note here that from the power law function Eq. 3.1 it is easy to obtain mean transverse momentum

$$\begin{aligned} \langle p_T \rangle &= \frac{\int_0^\infty p_T \cdot dN/dp_T \cdot dp_T}{\int_0^\infty dN/dp_T \cdot dp_T} \\ &= \frac{2p_0}{(n-3)} \end{aligned} \tag{3.3}$$

and pseudorapidity density

$$\begin{aligned} \frac{dN}{d\eta} &= \int_0^\infty \frac{d^2N}{dp_T d\eta} \cdot dp_T \\ &= \frac{2\pi C p_0^2}{(n-2)(n-1)}. \end{aligned} \tag{3.4}$$

Table 3.1: Extrapolated NN reference p_T spectrum and its systematic uncertainty for $\sqrt{s} = 130$ GeV from UA1 $\bar{p} + p$ data within $|\eta| < 2.5$. p_T and $d^2\sigma/dp_Td\eta$ are in units of (GeV/c) and (mb/(GeV/c)), respectively.

p_T interval	p_T	$d^2\sigma/dp_Td\eta$	Lower bound (%)	Upper bound (%)
0.00 - 0.10	0.05	108	-1.5	1.0
0.10 - 0.20	0.15	184	-0.6	0.5
0.20 - 0.30	0.25	167	0.0	0.0
0.30 - 0.40	0.35	130	0.5	-0.3
0.40 - 0.50	0.45	95.2	0.7	-0.5
0.50 - 0.60	0.55	67.8	0.8	-0.6
0.60 - 0.70	0.65	47.6	0.8	-0.6
0.70 - 0.80	0.75	33.3	0.6	-0.5
0.80 - 0.90	0.85	23.3	0.3	-0.4
0.90 - 1.00	0.95	16.4	-0.1	-0.2
1.00 - 1.10	1.05	11.6	-0.6	0.0
1.10 - 1.20	1.15	8.21	-1.1	0.3
1.20 - 1.30	1.25	5.87	-1.7	0.6
1.30 - 1.40	1.35	4.22	-2.3	0.9
1.40 - 1.50	1.45	3.06	-3.0	1.3
1.50 - 1.60	1.55	2.23	-3.7	1.6
1.60 - 1.70	1.65	1.64	-4.5	2.0
1.70 - 1.80	1.75	1.21	-5.2	2.5
1.80 - 1.90	1.85	0.899	-6.0	2.9
1.90 - 2.00	1.95	0.673	-6.8	3.3
2.00 - 2.10	2.05	0.507	-7.5	3.8
2.10 - 2.20	2.15	0.384	-8.3	4.2
2.20 - 2.30	2.25	0.293	-9.1	4.7
2.30 - 2.40	2.35	0.224	-9.9	5.2
2.40 - 2.60	2.50	0.153	-11.1	5.9
2.60 - 2.80	2.70	0.0929	-12.7	6.9
2.80 - 3.00	2.90	0.0574	-14.3	7.9
3.00 - 3.35	3.16	0.031	-16.3	9.3
3.35 - 3.80	3.56	0.0132	-19.2	11.3
3.80 - 4.40	4.07	0.00469	-22.8	13.9
4.40 - 5.10	4.71	0.00144	-27.0	17.3
5.10 - 6.00	5.49	0.000393	-31.6	21.2

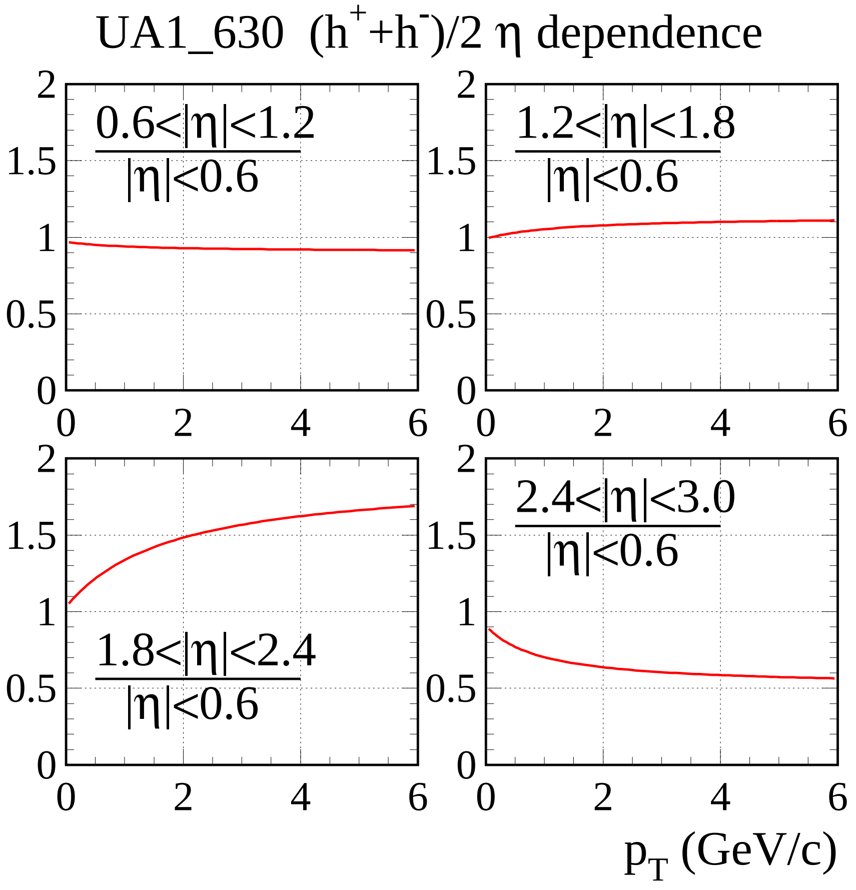

Figure 3.1: Possible η dependence in UA1 630 GeV $\bar{p}p$ data. Large uncertainty is seen as p_T increases.

3.1.2 η Acceptance Correction

The UA1 acceptance ($|\eta| < 2.5$) is different from this analysis. η dependence was studied by UA1 in $\bar{p}+p$ collisions at $\sqrt{s} = 630$ GeV [Boc96]. They claimed that no clear dependence was observed. However, their experimental uncertainties are large. As presented in Fig. 3.1 our re-examination of their data shows that variations in the p_T spectra from different η regions could be as large as 50%, hence any dependence below that level would certainly be buried.

The quantitative η dependence of the p_T spectrum can be calculated by pQCD based models. A reliable model calculation should be in good agreement with the known measurements in various aspects. We examine PYTHIA [Sj01] and HIJING [GW94] model calculations for 200 GeV $p(\bar{p})+p$ collisions in the identified particle ratios, the pseudorapidity density, and the inclusive charged hadron p_T spectrum. PYTHIA is a leading order (LO) pQCD model which incorporates the LO PDFs of CTEQ5L and is optimized to pp collisions. HIJING is a LO pQCD-inspired model with Duke-Owens PDFs [DO84] and is optimized to AA collisions. Fig. 3.2 shows various particle ratios for PYTHIA 200 GeV pp collisions, which are in agreement with the results of ISR measurements for pp at $\sqrt{s} = 23-63$ GeV [Alp75]. But the same HIJING calculation shows increased p/h^+ ratio with the increase of p_T. According to Xin-Nian Wang, one of two authors of the HIJING model, such a phenomenon is due to the diquark hard scattering mechanism implemented in HIJING [Wan02a]. Fig. 3.3 shows the $dN/d\eta$ distributions of the $(h^+ + h^-)$ from PYTHIA non-single diffractive (NSD) processes with the factor $K = 1$, 1.5, 2 and the $dN_{h^-}/d\eta$ distribution of the h^- from HIJING inelastic process. It appears that both PYTHIA NSD $dN/d\eta$ distributions for $K = 1$ and $K = 1.5$ agree reasonably well with the UA5 measurements for 200 GeV $\bar{p}p$ data [Aln86] while the magnitude for $K = 2$ seems too high. The HIJING $dN_{h^-}/d\eta$ distribution is almost half of that UA5 measurement of $(h^+ + h^-)$ for inelastic process. Finally, Fig. 3.4 shows the p_T spectra of the $(h^+ + h^-)/2$ for PYTHIA $K = 1$, 1.5, 2 and the p_T spectrum of the h^- from HIJING within the UA1 acceptance $|\eta| < 2.5$. The UA1 power law function fit result is also shown in the figure for comparison. It seems that there is better agreement with the larger K factor, in contrast to the $dN/d\eta$ case.

After this investigation, we decided to make the η acceptance correction based on the PYTHIA calculation with $K = 1.5$, incorporating the cases of $K = 1$ and $K = 2$ as the estimate of systematic uncertainty. The invariant multiplicity distributions are calculated for inclusive charged hadrons in 130 GeV pp collisions within $|\eta| < 2.5$, $|\eta| < 0.5$, and $0.5 < |\eta| < 1$. In order to estimate model dependent systematic un-

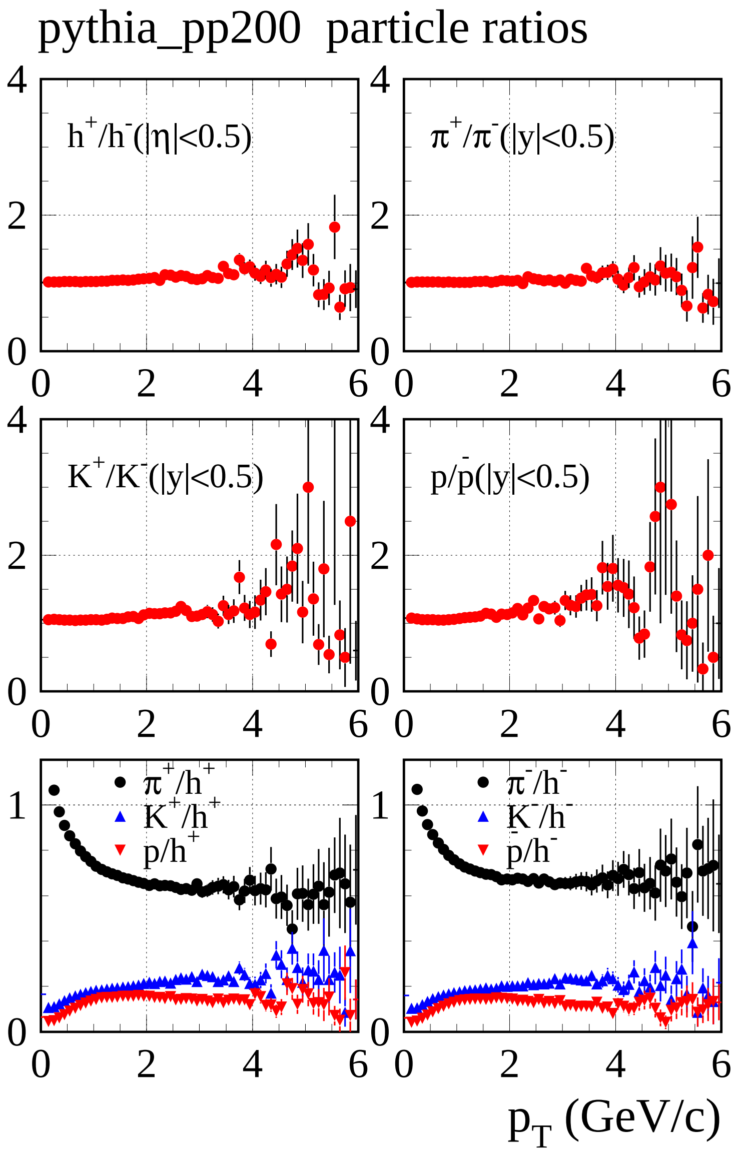

Figure 3.2: Various particle ratios in PYTHIA 200 GeV pp collisions, which are in agreement with the results of ISR measurements for pp at $\sqrt{s} = 23 - 63$ GeV.

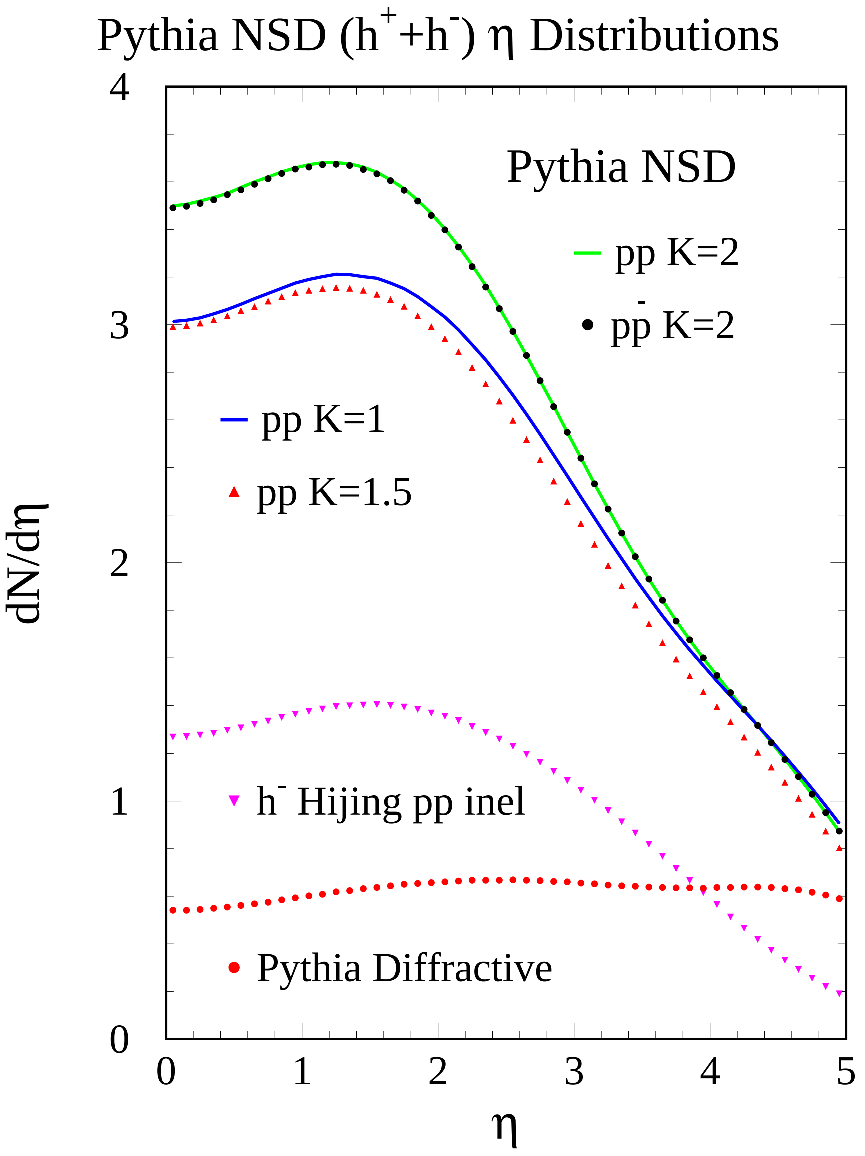

Figure 3.3: Various $dN/d\eta$ distributions of the $(h^+ + h^-)$ for PYTHIA 200 GeV NSD $p(\bar{p}) + p$ processes and the h^- for HIJING 200 GeV inelastic pp process. Agreements with the UA5 measurements [Aln86] ocurr for PYTHIA $K = 1$, 1.5 and for HIJING h^-.

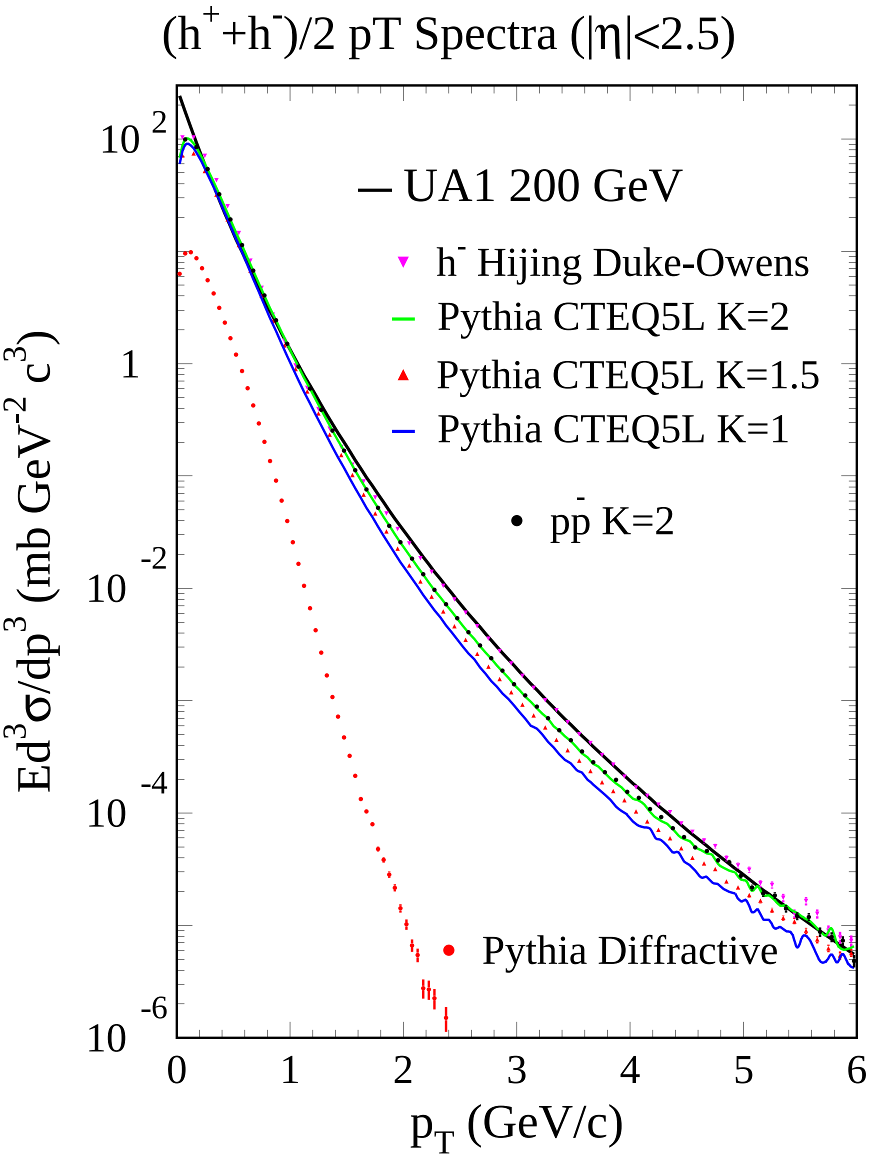

Figure 3.4: Various p_T distributions of the $(h^+ + h^-)/2$ for PYTHIA 200 GeV NSD $p(\bar{p}) + p$ precesses and the h^- for HIJING 200 GeV inelastic pp process within $|\eta| < 2.5$. The better agreements with the UA1 measurements ocurr for PYTHIA $K = 2$ and for HIJING h^-.

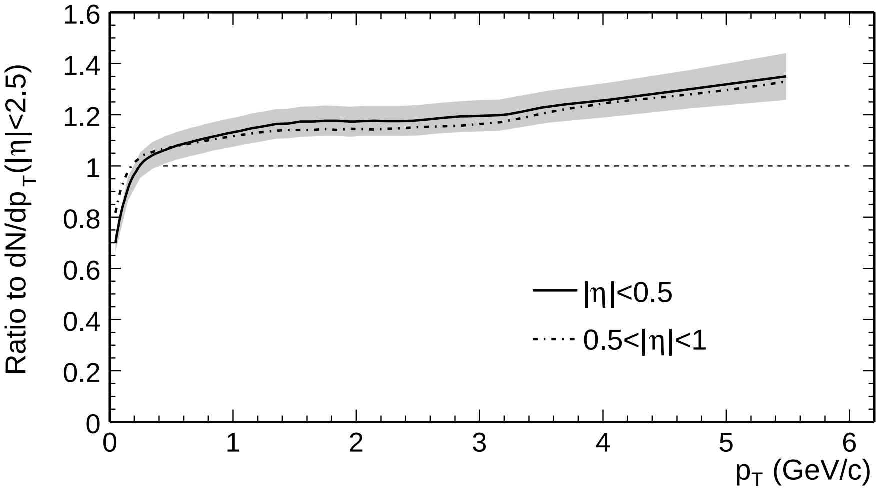

Figure 3.5: η correction function from model calculations: ratios of p_T spectra in two different η regions to that within $|\eta| < 2.5$, in which the UA1 Collaboration published its inclusive charged particle p_T spectrum.

certainty, another independent pQCD calculation [Vit03] is also performed. Fig. 3.5 shows the p_T-dependent correction functions for two η regions, obtained by averaging over the two pQCD calculations. The solid curve is the ratio of dN/dp_T within $|\eta| < 0.5$ to that within $|\eta| < 2.5$, and the shaded area shows its systematic uncertainty. The dot-dashed curve shows the same ratio for $0.5 < |\eta| < 1$, and the similar magnitude of the uncertainty on the ratio of $0.5 < |\eta| < 1$ to $|\eta| < 2.5$ is not shown. The multiplicative correction of 1.35 ± 0.09 (1.33 ± 0.09) at $p_T = 5.5$ GeV/c is obtained for $|\eta| < 0.5$ ($0.5 < |\eta| < 1$). The difference between $|\eta| < 0.5$ and $0.5 < |\eta| < 1$ is quite small, indicating a relatively flat η distribution within $-1 < \eta < 1$ for a broad p_T range.

Finally, we derive σ_{in} in the NN reference at $\sqrt{s} = 130$ GeV. From Eq. 3.4 and Fig. 3.5, we can obtain $d\sigma/d\eta(|\eta| < 0.5)(= \sigma_{in} dN/d\eta(|\eta| < 0.5) = 90.2$ mb. From an energy dependence

$$\frac{dN_{ch}}{d\eta}(\eta = 0) = 0.023 \ln^2(s) - 0.25 \ln(s) + 2.5, \tag{3.5}$$

which was obtained by fitting CDF and UA5 data [Abe90], we have $dN/d\eta(|\eta| = 0) = 2.246$. Assuming $dN/d\eta(|\eta| < 0.5) = dN/d\eta(|\eta| = 0)$, we derive $\sigma_{in} = 40.2$ mb.

3.2 Geometry of Nuclear Collisions

In nucleus-nucleus collisions, the number of participants, N_{part}, is defined as the number of nucleons which suffered at least one inelastic collision with another nucleon. N_{part} is a critical parameter in the study of heavy ion reactions at high energy since, for a given colliding system and beam energy, it determines the volume and the energy of the fireball. In theoretical models, N_{part} is a function of the impact parameter b, which is defined as the transverse distance between the centers of the target and projectile nuclei in a A+A collision. The impact parameter defines the centrality which represents the fraction of the total geometric cross section. For a head-on (the most central) collision, the impact parameter $b = 0$; $N_{part} \approx A + A$; and the collision probability is very small, therefore corresponding to the top percentage (a few %) of centrality. N_{part} can thus be used as a measure of the centrality. In experiments, the centrality is usually determined by measuring one or more of the following observables: charged particle multiplicity N_{ch}, transverse energy E_T in middle rapidity regions, and the forward energy E_F of spectator neutrons deposited in the zero degree calorimeter (ZDC) (see also Chapter 4 for details). Fig. 3.6 illustrates a semi-central A+A collision geometry and possible experimental observables.

The number of participants, N_{part}, and the number of binary nucleon-nucleon collisions, N_{coll}, in the nucleus-nucleus collisions are two important quantities when we compare experimental results with model predictions. Unfortunately, at RHIC N_{part} and N_{coll} could not be measured directly and have to be obtained in a model-dependent way. Considerable discrepancy exists among various model calculations,

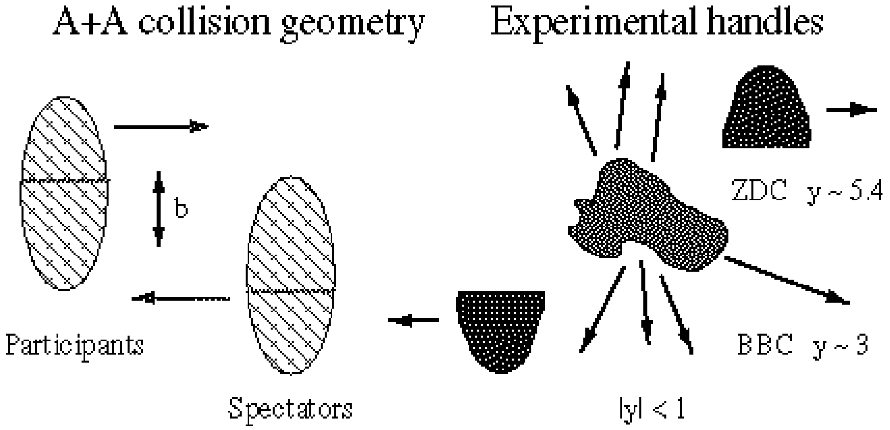

Figure 3.6: Illustration of nuclear collision geometry and experimental handles.

especially for peripheral collisions [Sa02]. In a STAR published paper [Adl02a], N_{part} and N_{coll} were obtained from a Monte Carlo Glauber model calculation. In this analysis, we present calculations of N_{part} and N_{coll} using three dynamic models: FRITIOF [AGP93], HIJING [GW94] and VENUS [Wer93]. Both FRITIOF and HIJING are the two-component models, in which the momentum transfer of the soft processes is treated phenomenologically and the hard processes are calculated by pQCD. The excited nucleons after collisions are stretched out as quark-diquark strings and fragments based on the Lund fragmentation scheme [And83]. In HIJING, the parton energy loss in the dense medium and nuclear modification of the parton structure function are also modeled. VENUS is based on the Gribov-Regge theory and string fragmentation. We will discuss results based on ingredients of physics in each model and compare them with results from a Monte Carlo Glauber model calculation in [Adl02a], which will shed light on systematic uncertainties of N_{part} and N_{coll}.

All the three dynamic models describe nuclear collision geometry using the Woods-Saxon nuclear density distribution and the eikonal formalism to determine the probability for each binary nucleon-nucleon collision, and to compute N_{part} and N_{coll}. The

Woods-Saxon nuclear density distribution has a form

$$\rho(r) = \frac{\rho_0}{1+\exp[(r-r_0)/D]}, \tag{3.6}$$

with normalization to $\int \rho(r)dr = A$ and parameters: nuclear radius r_0 and surface diffuseness D. Table 3.2 shows the comparisons of the nuclear geometries implemented in FRITIOF, HIJING, and VENUS for Au + Au collisions at $\sqrt{s_{NN}} = 130$ GeV. The overlap function, which defines the probability for a nucelon-nucelon collision at a given impact parameter b, has the following form in HIJING and FRITIOF

$$1-\exp(-2\Omega(b)), \tag{3.7}$$

with $\Omega(b)$ defined in Table 3.2 while it is a step function, $\theta(b-R)$, in VENUS. The participant scaling parameter, α in Table 3.2, is defined by the following expression

$$N_{coll} = B\cdot N_{part}^{\alpha}. \tag{3.8}$$

It shows that the scaling exponents α for these models are approximately $4/3$ due to the fact that $N_{part} \propto A^1$ and $N_{coll} \propto A^{4/3}$.

3.3 Participants and Binary Collisions

The distributions of N_{part} and N_{coll} for 130 GeV Au + Au collisions from these three models are shown in left and right panels in Fig. 3.7, respectively. It is worthwhile to note here that distribution differences among HIJING and VENUS are mainly due to different overlap functions. Calculations show that N_{part} and N_{coll} distributions

Table 3.2: Comparisons of nuclear geometries implemented in various models for 130 GeV Au + Au collisions.

Model	FRITIOF 7.02	HIJING 1.35	VENUS 4.12
Woods-Saxon Parameters	$r_0 = 6.52$ fm $D = 0.540$	$r_0 = 6.38$ fm $D = 0.535$	$r_0 = 6.64$ fm $D = 0.540$
Mininmum Distance of Two Nucleons	0.8 fm	0.4 fm	0.8 fm
Nucleon-Nucleon Overlap Function	$\Omega(b) = \Omega_0 \exp(-\beta b^2)$	$\Omega(b) = (1+\sigma_{jet}/\sigma_{soft})\chi_0(\xi)$ $\xi = b/b_0(s)$ $\chi_0(\xi) = \mu_0^2(\mu_0\xi)^3 K_3(\mu_0\xi)/96$	$\theta(b-R)$
Maximum Impact Parameter	24.20 fm	25.60 fm	24.10 fm
Inelastic Nucleon-Nucleon Collision Accepted	nucleon excitation energy should increase after each collision.	no restriction	no restriction
Nucleon-Nucleon Cross Section σ_{in}	40.19 mb	38.72 mb	37.45 mb
Scaling Exponent α	1.30 ± 0.08	1.41 ± 0.08	1.34 ± 0.08

from them tend to be identical if the same overlap functions of models are used. Low N_{coll} from FRITIOF may be attributed to the restriction on accepted inelastic nucleon-nucleon collisions.

The correspondence between the centrality classes defined by measured charged particle multiplicity and by modeled impact parameter was used to extract the average N_{part} and N_{coll} from models for a given centrality bin. Variations of average N_{part} and N_{coll} by different centrality selections were estimated using the Monte Carlo events from the HIJING model. The event classes corresponding to the same fractional cross section were selected by impact parameter b, multiplicity N_{ch} as well as participants, N_{part}, and binary collisions, N_{coll} , cuts. The average N_{part} or N_{coll} are consistent within 2% for each centrality bin except the 60–80% most peripheral bin, in which the discrepancy is at a level of 6%.

The results of N_{part} and N_{coll} from the models are shown in Table 3.3. The Monte Carlo Glauber model used to extract N_{part} and N_{coll} is described in [Adl02a, Ada].

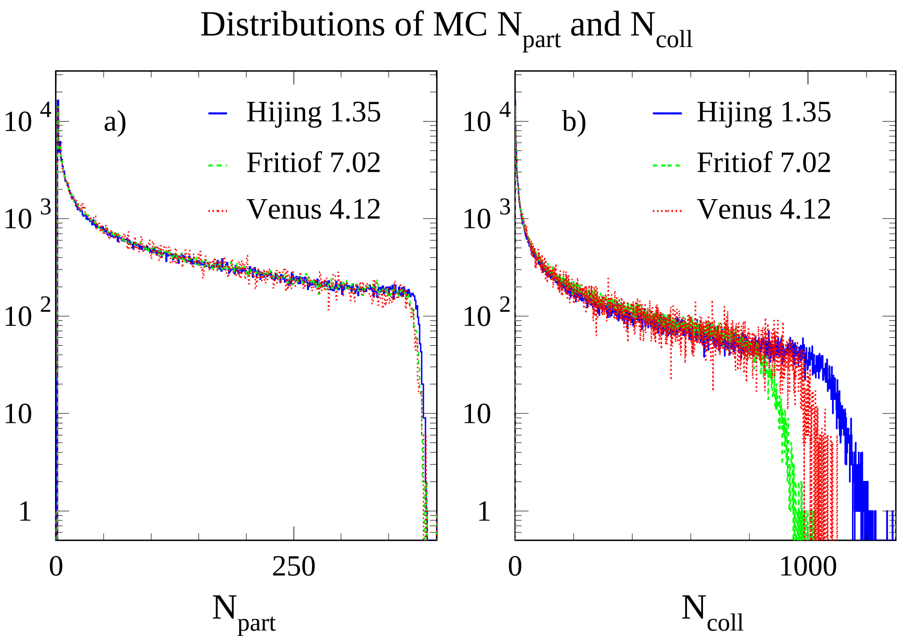

Figure 3.7: The distributions of N_{part} and N_{coll} for 130 GeV Au + Au collisions from three models.

Systematic uncertainty (7%) of N_{coll} from HIJING for the 0–5% most central bin is the quadrature sum of followings: 2% due to different centrality class selections, 1% due to total cross section uncertainty, 4% straightforwardly from difference of σ_{in} used in HIJING and in the NN reference, and 5% from possible variations of r_0 and D for a colliding gold nucleus. Then we derived a dependence of systematic uncertainties of N_{coll} or N_{part} as a function of centrality based on fluctuations in N_{coll} or N_{part} distributions with respect to the systematic uncertainty of N_{coll} from HIJING for the 0–5% most central bin. Systematic uncertainties of N_{coll} or N_{part} for selected centrality bins were obtained from the centrality dependence. The solid curves shown in Fig. 3.8 represent such a centrality dependence of systematic uncertainties of N_{part} (upper panel) or N_{coll} (lower panel) for HIJING results. It is derived from RMS coming from impact parameter cuts for different centrality bins with same fraction (5%) by assuming that the RMS or dynamic fluctuations contain the relevant systematic uncertainty information.

Table 3.3: Average values and uncertainties of N_{part} and N_{coll} from model calculations.

Centrality	FRITIOF		HIJING		VENUS		Glauber	
	N_{part}	N_{coll}	N_{part}	N_{coll}	N_{part}	N_{coll}	N_{part}	N_{coll}
0–5%	349±13	775±51	353±13	957±67	346±14	872±57	350^{+4}_{-4}	965^{+67}_{-67}
5–10%	297±13	623±41	300±14	749±61	293±14	694±50	296^{+7}_{-7}	764^{+59}_{-63}
10–20%	231±14	450±38	233±15	523±52	228±15	496±46	232^{+9}_{-9}	551^{+48}_{-56}
20–30%	164±14	287±32	164±13	318±41	161±13	311±37	165^{+10}_{-10}	348^{+44}_{-45}
30–40%	112±13	175±27	112±12	183±30	111±11	187±28	115^{+10}_{-12}	210^{+36}_{-36}
40–60%	59±10	77±18	58±10	75±17	58±9	80±17	62^{+9}_{-11}	90^{+22}_{-22}
60–80%	20±7	20±9	18±6	16±6	20±6	19±7	20^{+5}_{-6}	20^{+7}_{-9}

The ratios of N_{part} or N_{coll} from various models to those from HIJING are shown in Fig. 3.9. We can see that over a broad range of centrality model dependent uncertainties of N_{part} and N_{coll} are within 10% and 20%, respectively. In this analysis, we will use N_{part} and N_{coll} from the HIJING model calculation.

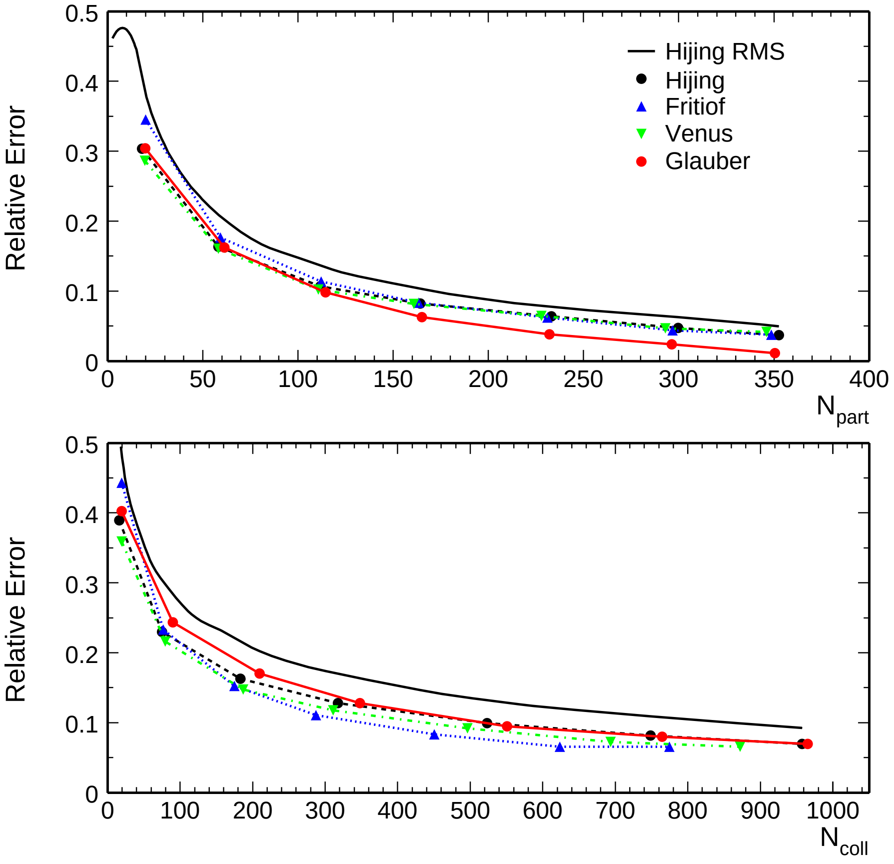

Figure 3.8: Determinations of the systematic uncertainties of N_{part} (upper panel) or N_{coll} (lower panel) for different models. Solid curves are RMS from HIJING. Points are relative errors for different models, and curves through the points are to guide eyes.

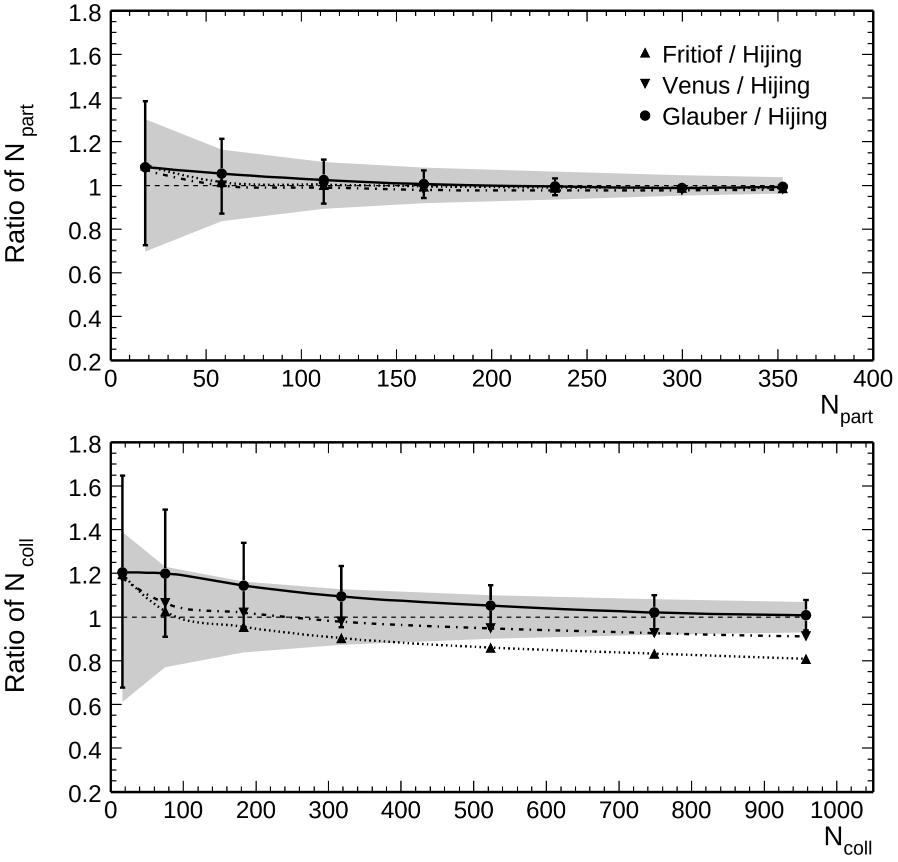

Figure 3.9: Ratios of the number of participants N_{part} (upper panel) or the number of binary collisions N_{coll} (lower panel) determined from different models to that from HIJING. Shaded areas show the uncertainties of N_{part} or N_{coll} from HIJING. Solid dots and error bars represent results from a Monte Carlo Glauber model calculation in [Adl02a]. Curves are to guide eyes.

CHAPTER 4

STAR Experiment

The Solenoidal Tracker At RHIC (STAR) is designed to search for signatures of quark-gluon plasma (QGP) formation and to investigate the behavior of strongly interacting matter at high energy density. The STAR experiment utilizes the STAR detector to record high multiplicity events of nucleus-nucleus collisions produced at the Relativistic Heavy Ion Collider (RHIC). The STAR experiment is one of four experiments at RHIC. The others are BRAHMS, PHENIX, and PHOBOS. The STAR experiment is also among the largest detectors and collaborations in the physics community. The STAR Collaboration is currently comprised of 49 institutions, or 459 collaborators from 9 countries in the world. A full STAR Collaboration author list and scientific journal publications are appended in Appendix B. The UCLA Intermediate Energy Physics and Relativistic Heavy Ion Group, which totals 3 faculty members, 6 research staff, and 9 graduate students, is actively involved in the construction and maintenance of STAR detectors (TPC, EMC, etc.) and in the physics analyses of STAR Au+Au, p+p, and d+Au collision data.

4.1 RHIC Accelerator Complex

The Relativistic Heavy Ion Collider is located at the Brookhaven National Laboratory in Long Island, New York. The facility consists of two rings of superconducting magnets, each with a circumference of 2.4 miles. The whole RHIC complex (Fig. 4.1) includes the Tandem Van de Graaff accelerator, the Booster Synchrotron, and the Alternating Gradient Synchrotron (AGS). Gold (Au) atoms are generated in the Pulsed Sputter Ion Source in the tandem. They are accelerated and passed through two Au foils to strip off some of the electrons from the atoms. That leaves a beam of Au atoms with an energy of 1 MeV/nucleon and a distribution of charge states peaking at +32e. The 1 MeV/nucleon Au is then transferred to the booster where it is accelerated to 95 MeV/nucleon and further stripped to a net charge of +77e before it is injected to the AGS. In the AGS, the energy of the Au beam is increased to 10.8 GeV/nucleon and the beam is bunched. In the final stage of the injection into the RHIC rings, all the orbital electrons of the Au atoms are stripped off and the atoms have a charge of +79e. Once injected into RHIC, the bunches are accelerated to collision energy and kept in the rings by the magnetic fields produced by the superconducting magnets. For proton beams, the Linear Accelerator is used as the source instead of the tandem.

Table 4.1: Physical parameters and performance specifications for the Relativistic Heavy Ion Collider (RHIC).

Physical Parameters		
No. Intersection Regions	6	
No. Bunches/ring	60	
Bunch Spacing (nsec)	213	
Collision Angle	0	
Free Space at Crossing Point (m)	16	
Performance Specifications	*Au*	*p*
No. Particles/Bunch	1×10^9	1×10^{11}
Top Energy (GeV/u)	100	250
Energy Spread (10^{-3})	0.7	0.7
Luminosity, average ($\text{cm}^{-2}\text{sec}^{-1}$)	$\sim 2 \times 10^{26}$	$\sim 1 \times 10^{31}$
Luminosity Life Time (hr)	3	10
Average Beam Current (mA)	55	70

RHIC is the first machine in the world capable of colliding heavy ions. It can be used to accelerate and collide species ranging from $p+p$ at $\sqrt{s_{NN}} = 40-500$ GeV to

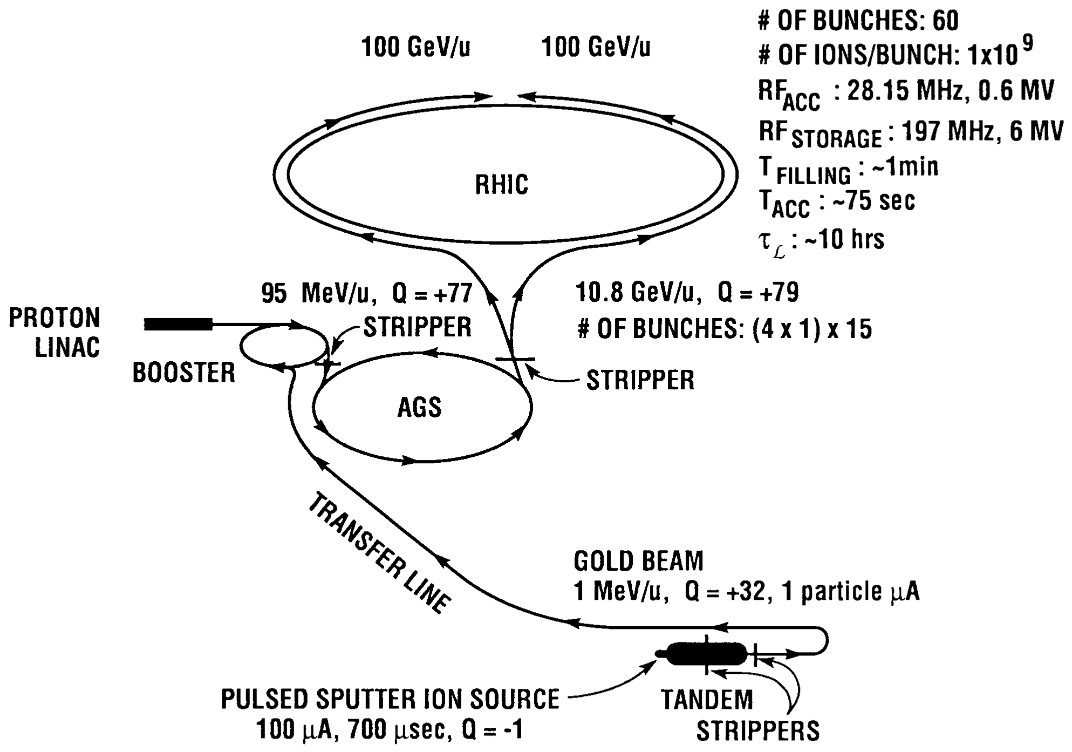

Figure 4.1: Diagram of the AGS - RHIC facility at the Brookhaven National Laboratory in Long Island, New York.

$Au + Au$ at $\sqrt{s_{NN}} = 40 - 200$ GeV. This great flexibility allows physicists to study a variety of colliding systems at a range of energies. Table 4.1 lists the some important physical parameters and performance specifications for RHIC.

The RHIC ring has 6 intersection points where the two rings cross, allowing the particle beams to collide. Four of the interaction regions are currently occupied by four experiments: BRAHMS, PHENIX, PHOBOS, and STAR. The first commissioning run occured in the summer of year 2000. At 9 PM on 12 June 2000, the first beam-beam collision event at RHIC at a collision energy of $\sqrt{s_{NN}} = 60$ GeV was recorded by STAR (Fig. 4.2). In Fig. 4.2, the lines coming out from the center are the tracks left in the detector by the high velocity charged particles produced in collisions. A few weeks later, STAR recorded collisions at $\sqrt{s_{NN}} = 130$ GeV, which is the nominal beam energy for the summer run in 2000 (Fig. 4.3). In 2001–2002, RHIC had the second commissioning run where it achieved its full design energy for Au+Au collisions at $\sqrt{s_{NN}} = 200$ GeV and commissioned the first polarized proton-proton collisions at $\sqrt{s} = 200$ GeV. In early 2003, RHIC began a deuteron-Au collision run at $\sqrt{s_{NN}} = 200$ GeV. The d+Au collision is chosen instead of p+Au because the charge to mass ratio (Z/A) for the deuteron (1/2) is much closer to that of Au (79/197) than for the proton (1/1), and therefore less adjustment of the magnetic fields for the two rings is needed.

4.2 The STAR Detector

The physics program of the STAR experiment is to study not only soft physics processes, i.e. hadron production at transverse momenta below 1–2 GeV/c but also hard QCD processes, i.e. jet, mini-jet and hard photon production [Col92]. Its ability to study global observables on an event-by-event basis with full azimuthal coverage

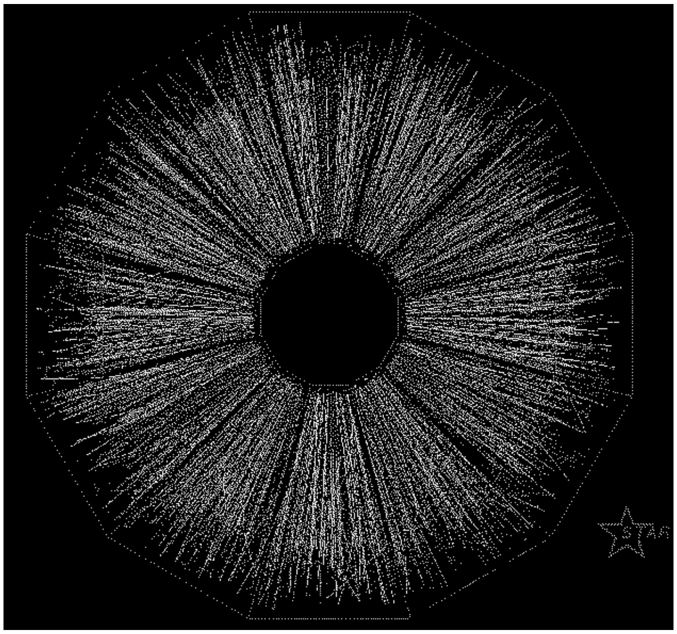

Figure 4.2: First collision at $\sqrt{s_{NN}} = 60$ GeV. Side view of TPC fiducial volume. Tracks are reconstructed from online level-3 trigger.

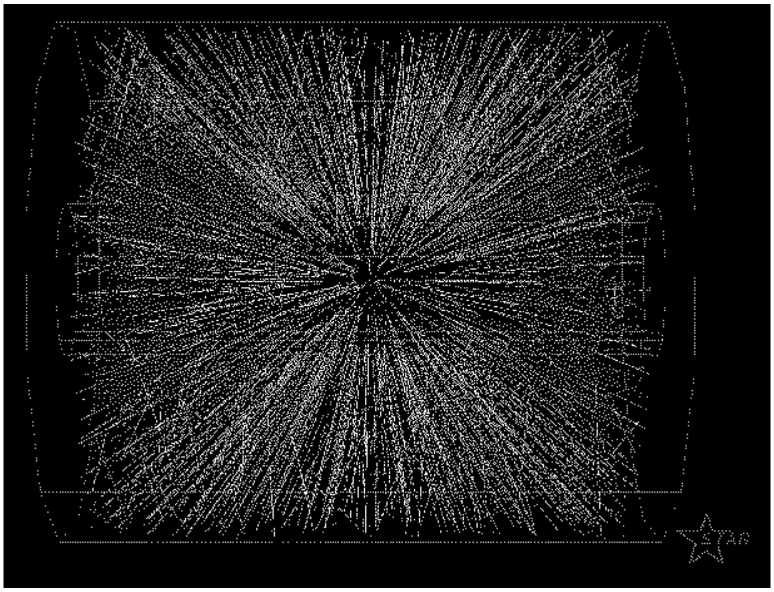

Figure 4.3: First collision at $\sqrt{s_{NN}} = 130$ GeV. End view of TPC fiducial volume. Tracks are reconstructed from online level-3 trigger.

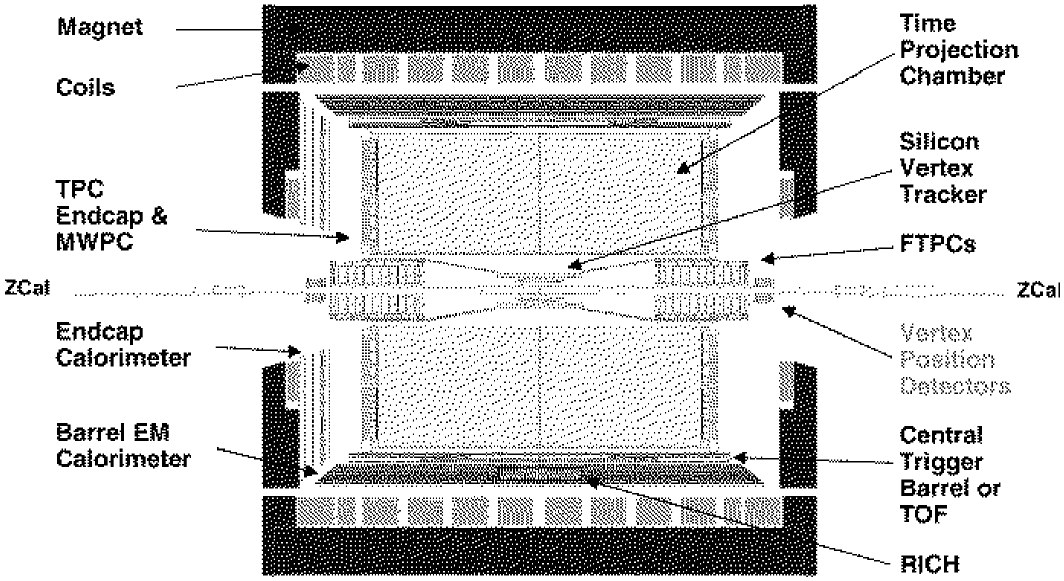

Figure 4.4: The STAR detector in a cross section view.

makes it a unique detector at RHIC.

The STAR detector [Ack03a], as shown in Fig. 4.4 in a cross sectional view, is a cylindrical detector system with full azimuthal coverage over the central rapidity region. The full configuration of the STAR detector will consist of these subsystems: a time projection chamber (TPC) [Ack99, And03a] and a silicon vertex tracker (SVT) [Bel03] inside a solenoidal magnet to enable charged particle tracking, momentum analysis, particle identification via dE/dx and location of primary and secondary vertices; a pair of radial-drift forward TPC (FTPC) [Ack03b] covering $2.5 < |\eta| < 4$ and with complete azimuthal coverage to extend the tracking to the forward region; a barrel electromagnetic calorimeter (BEMC) [Bed03] and an endcap electromagnetic calorimeter (EEMC) [All03] inside the magnet to measure and trigger on the total and local transverse energy deposition; a shower-maximum detector included in the EMC to distinguish high momentum single photons from photon pairs which result from π^0 and η meson decays; a time-of-flight detector (TOF) surrounding the TPC to improve the particle identification at higher momenta; a central trigger scintilator barrel (CTB) around the TPC, vertex position detectors (VPDs) near the beamline just outside the magnet, and zero degree calorimeters (ZDCs) [Adl01a] located in the region of the beam insertion magnets to provide a collision geometry trigger.

For the year 2000 data-taking, the setup consisted of only the TPC, CTB, ZDCs and one ladder of the SVT. A ring-imaging Cerenkov detector (RICH) [Bra03] with an area of approximately one square meter was positioned directly outside the TPC for high-p_T particle identification during the first two years of running. The STAR magnet [Ber03] can provide uniform fields along the beam direction with a strength of 0.25 Tesla (Half Field) to 0.5 Tesla (Full Field). For the Year 2000 physics run, the field was set at 0.25 Tesla. For the Year 2001-2002 and 2003 physics runs, the field was set at 0.5 Tesla and sometimes at 0.25 Tesla.

4.3 Time Projection Chamber

The TPC is the main tracking detector of the STAR. It covers the pseudo-rapidity region $-1.8 < \eta < 1.8$ and full azimuthal angle. Fig. 4.5 is a perspective view of the STAR TPC. The TPC is divided into two longitudinal drift regions, each 2.1 m long, by a thin cathode central membrane (CM) which is set at a voltage of -28 kV. Concentric inner and outer field cage cylinders (radius = 0.5 and 2.0 m), and the anode read out caps, which are 2.1 m away from the central membrane, define two coaxial cylindrical drift volumes of 24.75 m^3. Electric field uniformity is critical since track reconstruction precision is at a order of mm and electron drift paths are up to 2 meters. The chamber is filled with P10 gas (90% Argon + 10% Methane) regulated at 2 mbar above atmospheric pressure [Kot03]. The transverse diffusion in P10 is 230 $\mu m/\sqrt{cm}$ at 0.5 T or about $\sigma_T = 3.3$ mm after drifting 210 cm. Similarly, the longitudinal

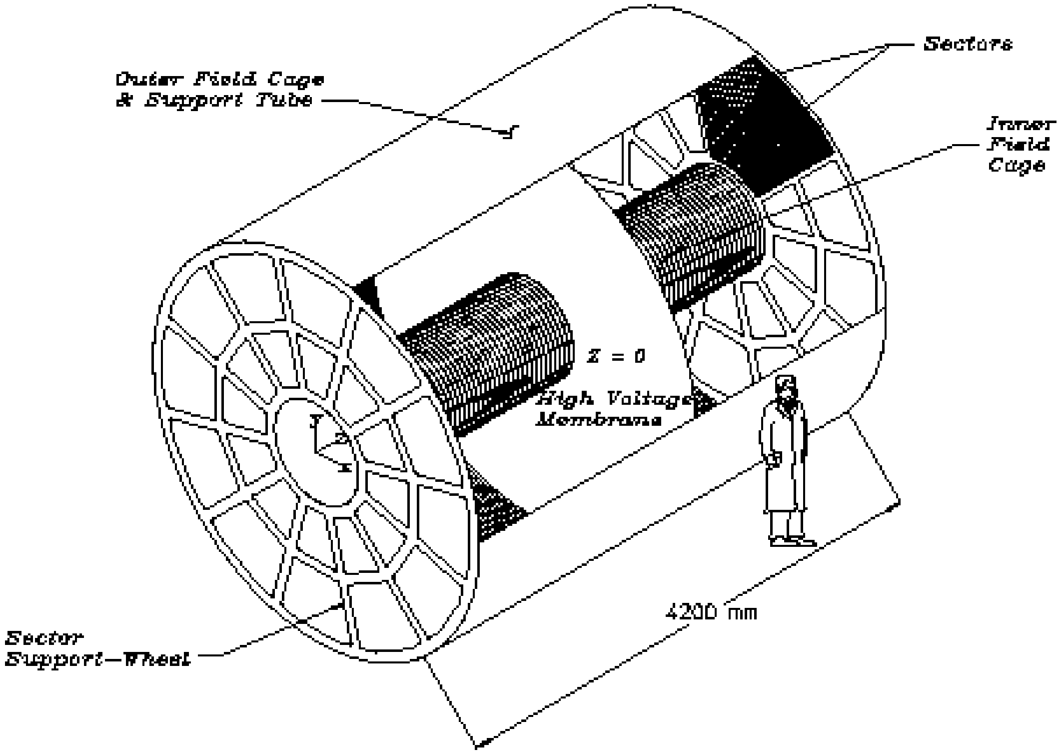

Figure 4.5: The STAR Time Projection Chamber surrouds a beam-beam interaction region at RHIC.

Table 4.2: Basic parameters for the STAR Time Projection Chamber and its associated hardware.

Item	Dimension	Comment
Length of the TPC	420 cm	Two halves, 210 cm long
Outer Diameter	400 cm	200 cm radius
Inner Diameter	100 cm	50 cm radius
Cathode (CM)	400 cm diameter	At the center of the TPC
Cathode Potential	28 kV	Typical
Drift Gas	P10	10% methane, 90% argon
Gas Pressure	atmospheric + 2 mbar	Regulated at 2 mbar
Drift Velocity	5.45 cm/μs	Typical
Transverse Diffusion (σ)	230 $\mu m/\sqrt{cm}$	140 V/cm & 0.5 T
Longitudinal Diffusion (σ)	360 $\mu m/\sqrt{cm}$	140 V/cm
Number of Anode Sectors	24	12 per end
Number of Pads	136,606	
Magnetic Field	0, ±0.25 T, ±0.5 T	Solenoidal

diffusion of a cluster of electrons that drifts the full length of the TPC is $\sigma_z = 5.2$ mm. At a typical drift velocity of 5.45 $cm/\mu s$, the longitudinal diffusion width is equal to a spread in the drift time spread width ($\sim$ 230 ns). Basic parameters for the TPC are listed in Table 4.2.

When a high velocity charged particle travels through the gas-filled TPC volume, the gas molecules will be ionized and produce positive ions and electron clouds along the path. The energy loss due to ionization is typically a few keV per cm of gas at the atmospheric pressur. This gives a total energy loss of a few MeV over a path length of 2 m. For most particles produced in heavy ion collisions, the kinetic energy is above 100 MeV. Under the influence of the electric field provided by the central membrane (CM), inner field cage (IFC), outer field cage (OFC), and the grounded anode plane, the electrons drift to the anode plane. The arrival time and locations of the electron clusters are recorded. Before the signals produced at the anode plane can be read out by the electronics system, they are collected by the pads shown in the Fig. 4.6. The

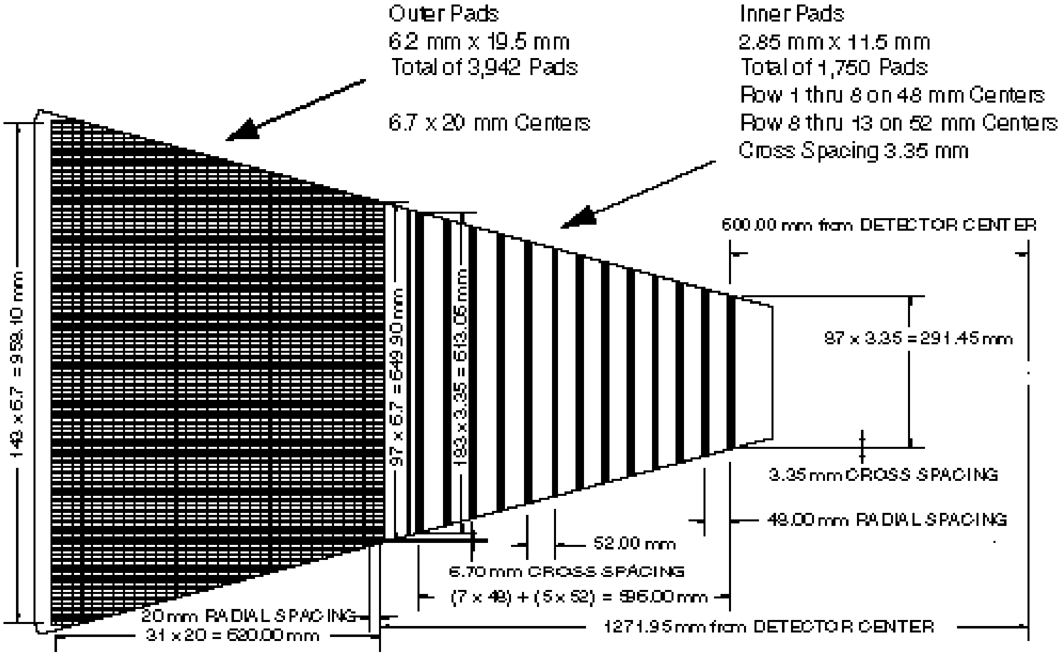

Figure 4.6: A TPC pad plane with one full sector which consists of an inner subsector and an outer subsector. The inner subsector is on the right and has small pads arranged in widely spaced rows. The outer subsector is on the left and is densely packed with larger pads.

signals on pads are image charges induced by the electron avalanches in the region close to the anode wires where the E field is very strong.

There are 136,606 pads grouped into 24 sectors, 12 at each end of the TPC. Each sector is divided into two subsectors (Fig. 4.6), an inner subsector and an outer subsector. The inner subsector is made of 13 pad rows and the outer subsector has 32 rows. Therefore, a straight track passing through both sectors gives 45 hit points in maximum. The configurations of inner subsector pads and outer subsector pads are different. The sizes of pads were designed according to the required position resolution along pad row direction. With dimensions of 2.85×11.5 mm^2, the inner pads are smaller than the outer pads with dimensions of 6.2×19.5 mm^2. This gives them better two-track resolution, which is needed in the region where the track density is high.

The readout system is based on Multi-Wire-Proportional-Chambers (MWPC) [And03b] with readout pads. The analog signals collected on the pad plane are amplified, shaped and then digitized into discrete signals in time. The amplitude of the digital signals is used later to form clusters and hits offline, while the timing information carried by them can be used to determine the hit position in the drift direction if the drift velocity is known.

Since the drift paths of electrons follow the electric field lines, the distortion of the E field has to be very small. The OFC and IFC serve this purpose. The OFC and IFC include a series of gradient rings set to a certain voltage by a chain of resistors that connect to the CM. In this way, the changes of the voltage at the boundary match the decrease in the body part of TPC and this results in a nearly constant axial E field. The distortion of the TPC drift field can be caused by the misalignment of the TPC in the magnet, the misalignment of the TPC sectors in the drift direction, E×B effect due to a component of the magnetic field in the $r-\phi$ direction which we must correct for, etc.

4.4 DAQ and Trigger

The STAR data acquisition system (DAQ) [Lan03] is fast and flexible. It receives data from multiple detectors and these detectors have a wide range of readout rates. The event size is of order 200 MB and the events are processed at input rates up to 100 Hz.

The discrete signals from each TPC sector are delivered to DAQ from 6 readout cards. The data from each readout card are sent to a DAQ reciever card via an optical fiber whose bandwidth is 1.5 Gbit/s. In the DAQ, these data are processed as appropriate, which may include pedestal subtraction, gain correction, and zero suppression. It also assembles the data from each detector subsystem into a form suitable for recording and distribution via network to analysis and monitoring tasks. A typical

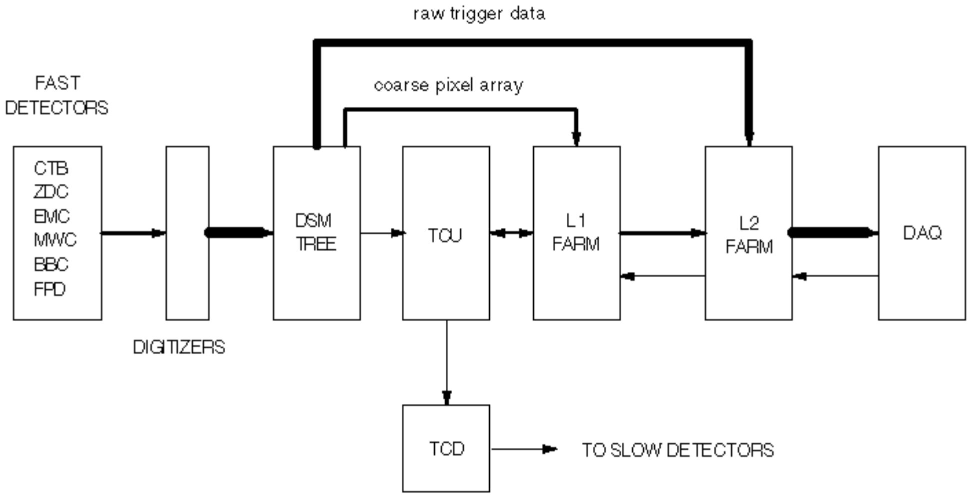

Figure 4.7: Data flow through the STAR trigger.

tape archiving rate is about 1 TPC event/s, which translates to 16 Mbyte/s. Compared to the beam crossing rate, the STAR data-taking is relatively slow due to the event size and the slow TPC. So the trigger system must look at every RHIC crossing and decide whether or not to initiate recording that event.

The STAR trigger system [Bie03] is a 10 MHz pipelined system which is based on input from fast detectors to control the event selection for the much slower tracking detectors. Data flow through the trigger is shown in Fig. 4.7.

The trigger system is functionally divided into different layers with level 0 being the fastest while level 1 and level 2 are slower but they apply more sophiticated constraints on the event selection. STAR has a third level trigger [Adl03] which performs complete reconstruction of the events in a dedicated CPU farm. The level 3 trigger system includes an online display so that individual events can be visually inspected in real time. The events seen in Fig. 4.2 and Fig. 4.3 were drawn by the STAR level-3 online display.

The fast detectors that provide input to the trigger system are a central trigger barrel (CTB) at $|\eta| < 1$ and two zero-degree calorimeters (ZDC West and ZDC East) located

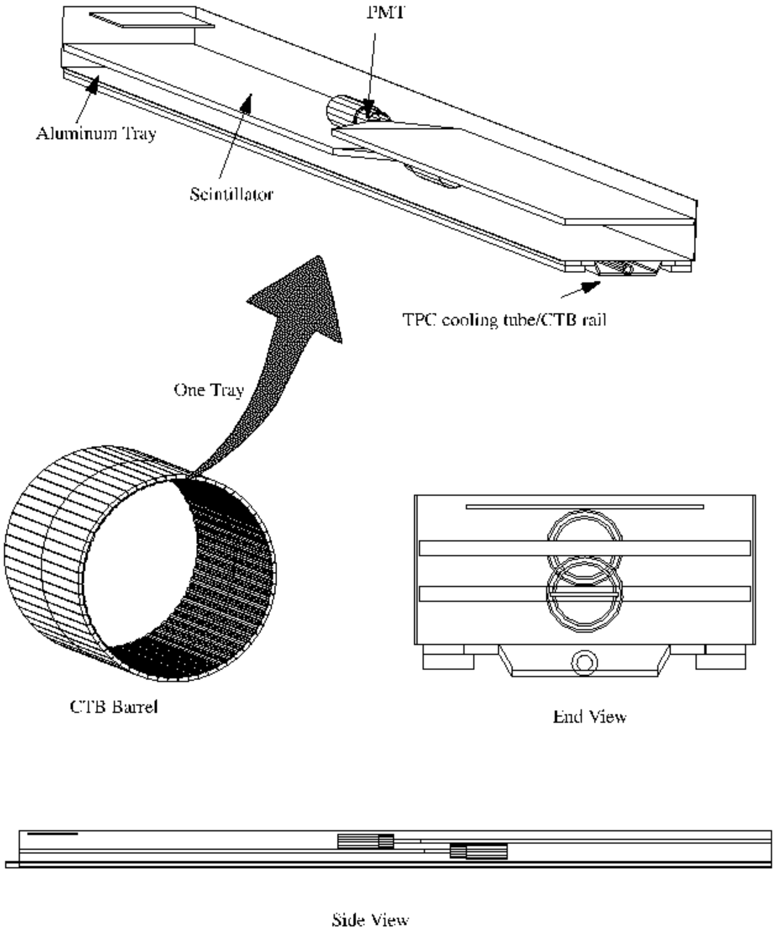

Figure 4.8: STAR central trigger scintillator barrel.

in the forward direction at $\theta < 2$ mrad and at 18 meters away from the interaction point. The CTB consists of 240 scintillator slats arranged in 4 cylindrical bands each covering 1/2 unit of pseudorapidity. The CTB slats cover the outer shell of the 4 m diameter of the TPC. Each slat consists of a scintillator, light guide, and photomultiplier tube (PMT). The CTB and one of its slats are shown in Fig. 4.8. Each ZDC consists of three modules. Each module consists of a series of tungsten plates alternating with layers of wavelength shifting fibers that route cherenkov light to a PMT. Such a ZDC is shown in Fig. 4.9.

The CTB triggers on the flux of charged particles in the midrapidity region. The

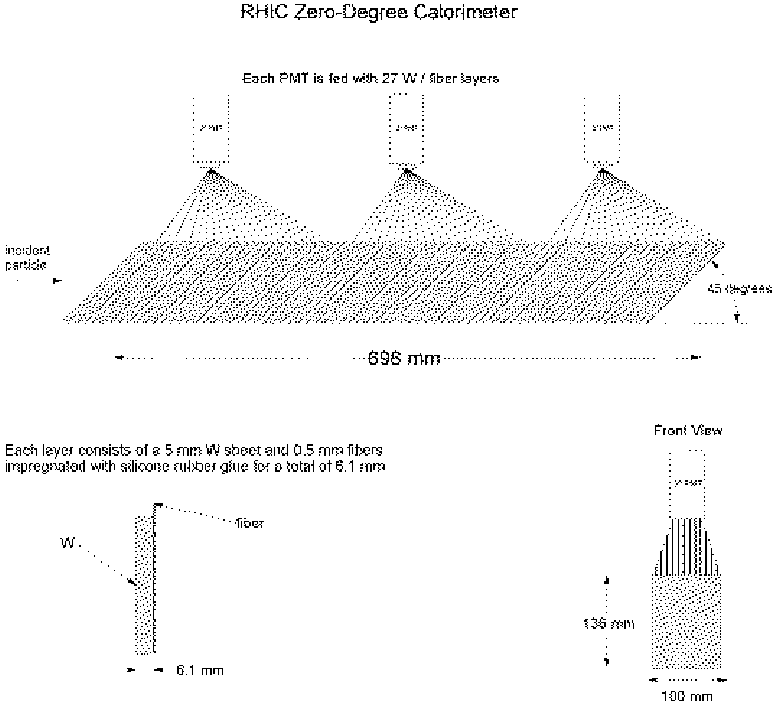

Figure 4.9: RHIC zero degree calorimeter.

ZDCs are used for determining the energy in neutral particles (mainly dissociated neutrons in spectator nuclei) remaining in the forward direction while the charged particles (protons) are bent away by dipole magnets (DX) located between interaction point and ZDCs. Fig. 4.10 presents the correlation between the summed ZDC pulse height (ZDC West and ZDC East) and the pulse height of the CTB for events with a primary collision vertex successfully reconstructed from tracks in the TPC. This correlation is used in the experiment to provide a centrality trigger for collisions. The ZDC is double-valued since collisions at either small or large impact parameter can result in a small amount of energy in the forward ZDC direction.

A minimum bias trigger was obtained by selecting events with a pulse height larger than that of one neutron in each of the forward ZDCs, which corresponds to 95% of the geometrical cross section. Triggers corresponding to smaller impact parameter (central collision) were implemented by selecting events with less energy in the forward ZDCs,

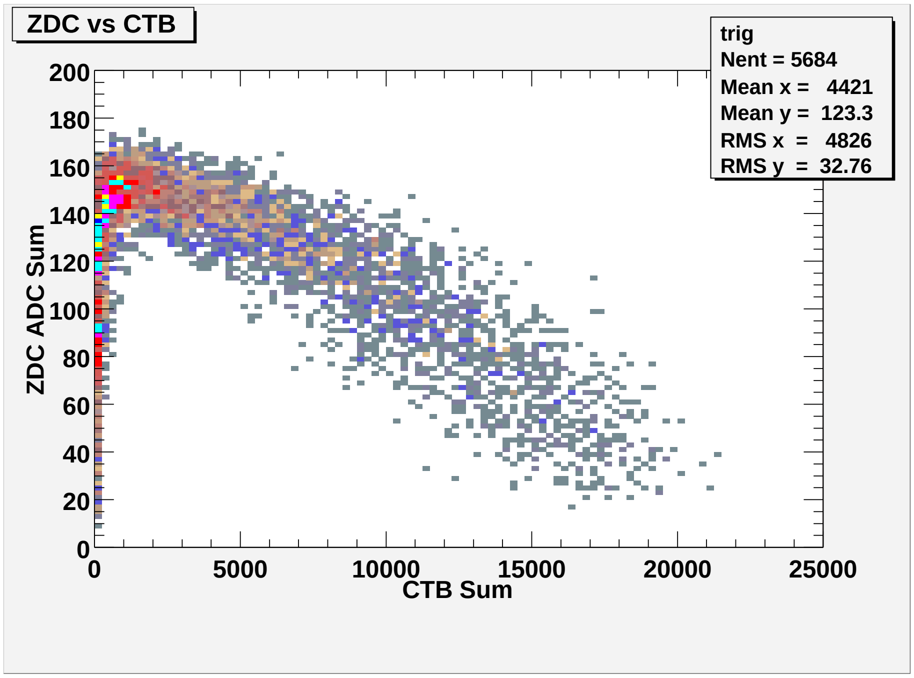

Figure 4.10: Correlation between the summed pulse heights from the ZDCs and the CTB for events with a primary collision vertex successfully reconstructed from tracks in the TPC.

but with sufficient CTB signal.

In the first year run, only the multi-wire proportional counters (MWPC or MWC) at the two ends of the TPC were implemented in the trigger level 0 for fast signal analysis. In the subsequent years, the electromagnetic calorimeter (EMC), the beam-beam counter (BBC), and the forward pion detector (FPD) have been installed and served for particular physics purposes by implementing in the trigger level 0. One of such triggers is the so-called "high tower trigger" by using the EMC signal to trigger on the events with at least one high transverse energy cluster. This trigger allows one to study high p_T phenomenon in the enriched event sample.

CHAPTER 5

Analysis

5.1 Reconstruction

Measurements presented in this dissertation are based on the two data sets of Au + Au collisions at $\sqrt{s_{NN}} = 130$ GeV, which were recorded by the STAR detector at RHIC in year 2000. The two data sets comprised of $\sim$ 1M minimum bias triggered events and $\sim$ 2M central collision triggered events which correspond approximately to the most central 10% of the Au + Au geometric cross section. Charged particle tracks of an event were detected in the Time Projection Chamber (TPC) with a pseudorapidity coverage $|\eta| < 1.8$ and complete azimuthal symmetry. Raw events were reconstructed under the STAR production version of P01hi. The event reconstruction goes through the following three steps:

1) *global tracking* – The Kalman Filter method derived from system theory has been used [Lik92]. A charged track in a uniform magnetic field is a helix which can project onto a circle in transverse plane and a straight line in bend plane. Five track parameters of a helix including curvature $k = q/p_T$ are obtained by the Kalman track fit which incorporates multiple Coulomb scattering and energy loss. The fit is initialized at the position of the hit with the largest distance from the vertex as the track density at the outer wall of the TPC is assumed to be lower. The estimation of the parameters is derived by a Least Squares Method (LSM). The calculated χ^2 can be used to identify outliers or wrongly associated hits, which can thus be removed from

the track [MS94].

2) *primary vertex finding* – The event vertex reconstruction (EVR) package [MC92] in the STAR software library is used to find the primary vertex of an event if the number of global tracks in this event is greater than 15. Such a condition is satisfied for all Au + Au collision events with the centrality of 0–80% geometric cross section. The trajectories of selected global tracks are extrapolated to the distance of closest approach (DCA) to the beam axis (assumed to be at $x = y = 0$), providing a starting seed value for the z position of the primary vertex of the event. The first iteration of the event vertex position is found by minimizing the DCAs for all selected tracks. Then a tighter, or the tightest 3-dimentional (3D) DCA cut is applied using the first, or the second vertex position to select a refined set of tracks for use in the second iteration, or in the final iteration. For the final vertex position, the 3D DCA position for all global tracks are computed [Ray99].

3) *primary track fit* – Once the primary vertex has been found, the global tracks with 3D DCA less than 3 cm are chosen for a refit by forcing a new helix ending at the vertex, which can be achieved by assigning a very small error to the vertex. The new helix parameters are associated with so-called “primary track”. The DCAs to the primary vertex for primary tracks are very close to zeroes according to fit procedure. Since the error assigned to the primary vertex is much smaller than those associated with TPC space points, a significant improvement on the momentum resolution (a factor of 2 – 3) for primary tracks is achieved. We will chose the primary track parameters in this analysis.

5.2 Simulation and Embedding

For physics analyses, a realistic simulation of detector response is critical in determining the acceptance and efficiency for measurements and in estimating the magnitude of background sources. The GSTAR [JI96] is the framework to run the STAR detector simulation using GEANT [Pro]. First, a few event generators (e.g., HIJING for Au + Au collisions, PYTHIA for $p+p$ collisions) can be used in the framework of the GSTAR. Then the produced final particles go through GEANT with the specified STAR detector geometry. The charged particles induce the ionization in the TPC gas, whose response can be simulated using the TPC Response Simulator (TRS). A detailed description and evaluation of the TRS can be found in the Ph.D. thesis of Hui Long [Lon02]. The Monte Carlo simulated events can then be sent to the STAR standard reconstruction chain providing data for final analyses.

However, heavy ion collisions are very complicated systems, usually with high particle multiplicity. No ideal event generator can produce all important features in real events. Any small deviation of the detector response generated at the level of single particles can be propagated finally to a large difference from real data. To avoid these deficits and to make the environment as realistic as possible, a procedure commonly known as “embedding” was developed. Generally, the simulated signal is embedded into a real raw event, and then this embedded event is reconstructed like a real raw event and, of course, the information of simulated signal is kept and can be easily recognized from those real signals. In the STAR, the embedded Monte Carlo tracks are only about 5% of real tracks, providing a minimally disturbed environment. After reconstruction, the simulated tracks can be associated with the corresponding reconstructed tracks, and vice versa. This allows one to examine the acceptance, efficiency etc. in a realistic environment.

5.3 Selection Criteria

5.3.1 Event Selection

The primary vertex position (x_{vtx} and y_{vtx}) in the transverse plane is limited by the beam pipe and has rather small spreads in both x and y directions. We obtained such a beam profile in the transverse plane by extracting it from measured x_{vtx} and y_{vtx} distributions. We assume for the measured deviations:

$$\sigma_{x,y}^2 = (\sigma_{vertex}^{x,y})^2/N_{ch} + (\sigma_{intrin}^{x,y})^2, \tag{5.1}$$

where σ_{vertex}^x denotes the single track vertex resolution in x direction, and σ_{intrin}^x denotes the multiplicity independent intrinsic broadening which should mainly come from beam width. We divided the minimum bias events into seven charged particle multiplity (N_{ch}) bins (which are corresponding to centrality bins, see next section). For each bin, we obtained average N_{ch} and σ_{vertex}^x, σ_{vertex}^y. Fitting Eq. 5.1 through 7 points as dashed curves shown in Fig. 5.1, we had

$$\sigma_{intrin}^x = 0.511\text{ mm} \quad \text{and} \quad \sigma_{intrin}^y = 0.433\text{ mm}, \tag{5.2}$$

and $\sigma_{vertex}^x \approx \sigma_{vertex}^y$ as two solid curves shown in Fig. 5.1 are very close to each other. This is a proof that the STAR is an azimuthal symmetric detector. We denote σ_{vertex}^T as the primary vertex resolution in the transverse plane, then

$$\sigma_{vertex}^T(N_{ch}) = (4.7 \pm 0.1)\text{mm}/\sqrt{N_{ch}}. \tag{5.3}$$

After this investigation, we decided to put a nominal cut on primary vertex position in the transverse plane of $|x_{vtx}| < 1$ cm and $|y_{vtx}| < 1$ cm.

On the other hand, the primary vertex position, z_{vtx}, in beam direction has a wide spread with one standard deviation above 80 cm as shown in Fig. 5.2. In order to

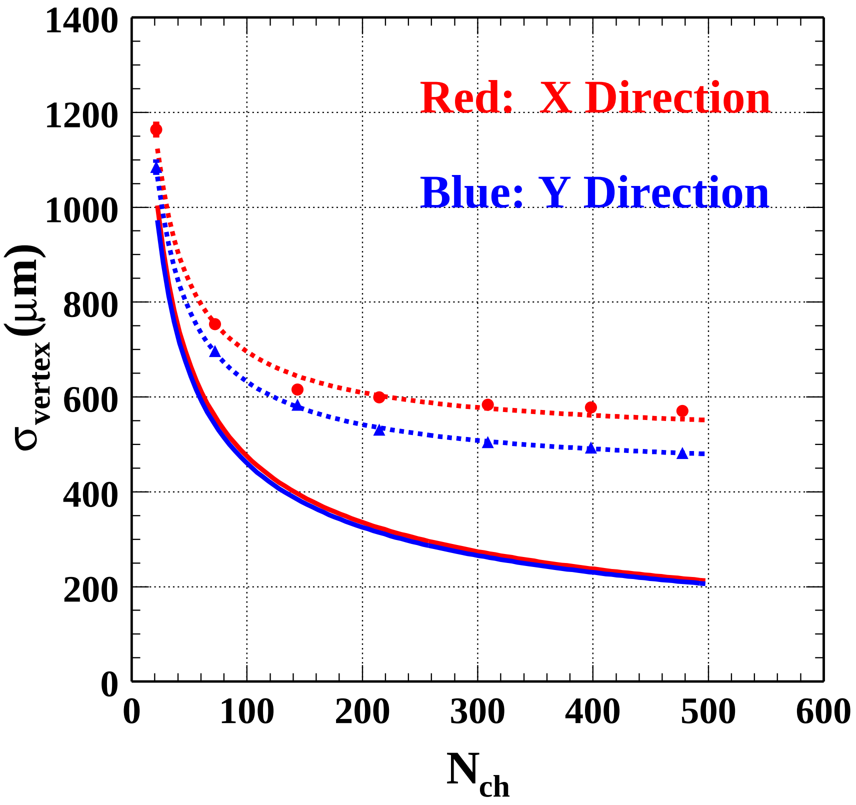

Figure 5.1: Primary vertex position spreads in the transverse plane as a function of charged particle multiplicity. Solid curves represent the derived primary vertex resolution in the transverse plane.

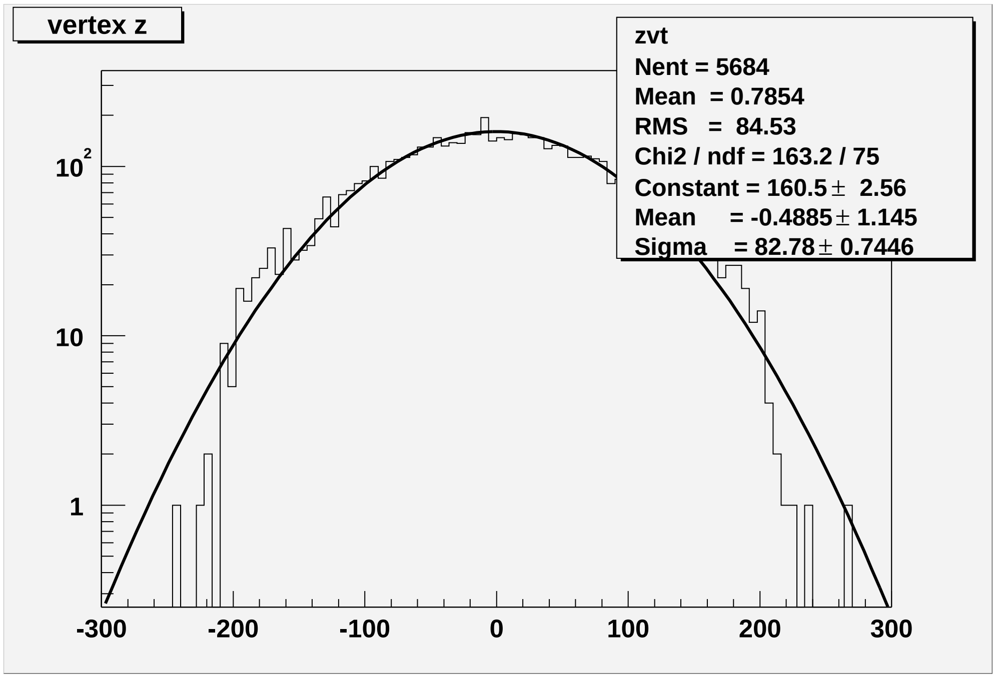

Figure 5.2: Primary vertex position distribution of z_{vtx} in the beam direction.

achieve certain acceptance of the tracks within $|\eta| < 1$ (see Fig. 5.19) and high statistics, we required the events with a primary vertex to have $|z_{vtx}| < 75$ cm. This requirement still leaves some high η region without full acceptance (tracks coming from the vertex will hit the TPC end plane). To estimate this effect, we divided z_{vtx} into six slices as shown in Table 5.1. The corresponding full η coverage can be calculated using TPC parameters listed in Table 4.2. We measured $dN_{ch}/d\eta$ for $p_T > 2$ GeV/c in each z_{vtx} slice and in the whole region with $|z_{vtx}| < 75$ cm in order to estimate the effect on high p_T particles. Fig. 5.3 shows results for one bin of $-1 < \eta < -0.9$. According to Table 5.1, only slice 4, 5, and 6 cover this η bin. We averaged the $dN_{ch}/d\eta$ in these three slices as the solid line, which is very close to the point at $z_{vtx} = 0$ for all particles within $|z_{vtx}| < 75$ cm. The large deviation seen in slice 1 does not contribute too much due to low statistics. Fig. 5.4 shows the comparison between $dN_{ch}/d\eta$ obtained in two ways described above. The agreements are within 2% for $-1 < \eta < 1$.

Table 5.1: Primary vertex position z_{vtx} slices and their corresponding ranges of full η coverage.

Slice Number	z_{vtx} Range	η Coverage
1	(-75, -50)	(-0.63, 1.08)
2	(-50, -25)	(-0.73, 1.00)
3	(-25, 0)	(-0.83, 0.92)
4	(0, 25)	(-0.92, 0.83)
5	(25, 50)	(-1.00, 0.73)
6	(50, 75)	(-1.08, 0.63)

After the event selection cuts, the minimum bias data set contained $\sim$ 181k events and the central data set contained $\sim$ 365k events.

5.3.2 Centrality Selection

Centrality selection is based on the uncorrected primary charged particle multiplicity N_{ch} within $|\eta| < 0.75$ and for $p_T < 1.5$ GeV/c. This requirement on the pseudorapidity range maximizes the number of tracks used to define centrality in an event while keeping the tracking acceptance approximately constant in this range (see Fig. 5.19). The requirement on the transverse momentum is to reduce the effect of high p_T hadrons on centrality determination. The percentage of the geometric cross section is determined by the corrected and normalized negatively charged hadron N_{h^-} ($|\eta| < 0.5$ and $p_T > 0.1$ GeV/c) distribution published by STAR in [Adl01b] through the correlation of N_{ch} and N_{h^-} as shown in Fig. 5.5:

$$N_{h^-} = 0.358 \cdot N_{ch}^{0.986}. \tag{5.4}$$

Then the minimum bias data set is divided into seven centrality bins by N_{ch} as shown in Fig. 5.6. The most central bin is 0–5% while the most peripheral bin is 60–80%. The N_{ch} from embedding data is also plotted in Fig. 5.6, showing good match with the

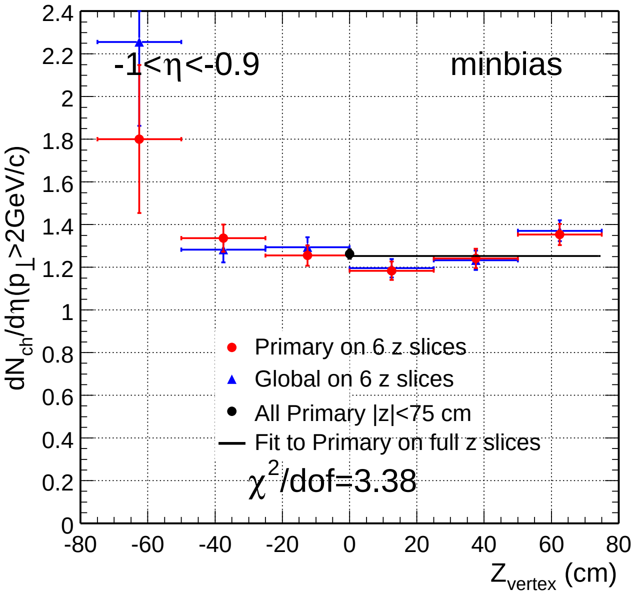

Figure 5.3: $dN_{ch}/d\eta(p_T > 2\text{GeV}/c)$ in different z_{vtx} slices for $-1 < \eta < -0.9$.

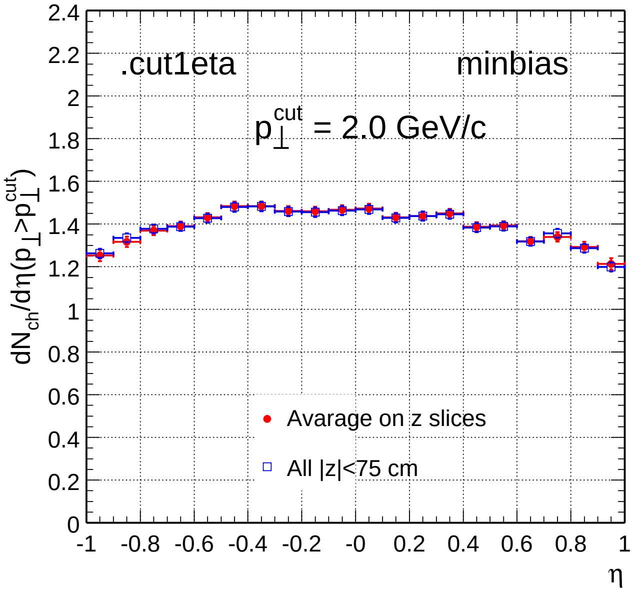

Figure 5.4: $dN_{ch}/d\eta(p_T > 2\text{GeV}/c)$ as a function of η. $dN_{ch}/d\eta$ is measured in two ways.

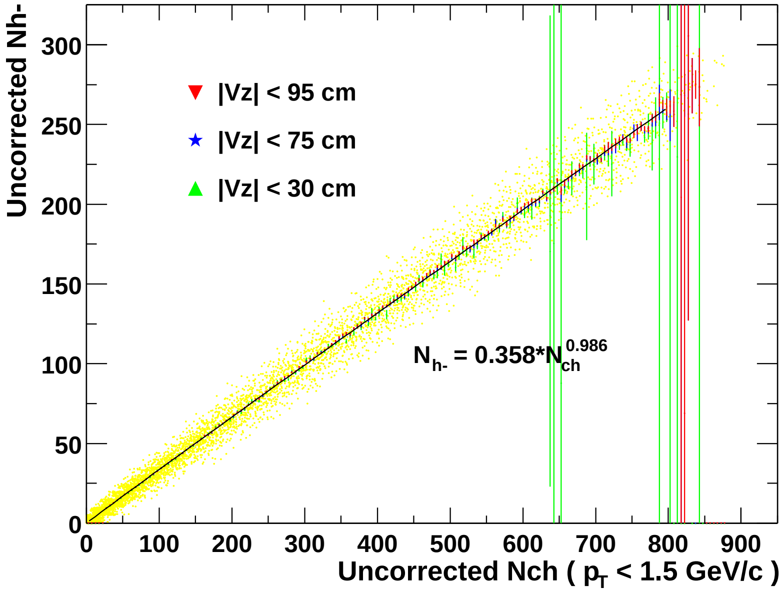

Figure 5.5: Correlation between uncorrected N_{ch} and uncorrected N_{h^-} in different z_{vtx} cuts. The scattered points are for $|z_{vtx}| < 75$ cm. The curve is a fit, giving parameters in Eq. 5.4.

same distribution from real data. Therefore, the systematic uncertainty from centrality selection is negligible. The central data set corresponds to two unbiased centrality bins of 0–5% and 5–10%. Table 5.2 lists the values of N_{ch} cuts used and their corresponding uncorrected and corrected N_{h^-}, and the average negatively charged particle density $\langle dN_{h^-}/d\eta \rangle$ in each centrality bin.

5.3.3 Track Quality Cuts

This analysis covers a transverse momentum range of $0.2 < p_T < 6$ GeV/c and a pseudorapidity range of $-1 < \eta < 1$. The successfully fitted (flag > 0) primary track selection involves the quality cuts on the number of space points out of 45 pad rows in the TPC used in the track fit (N_{fitpts}), on the probability of the primary track fit (*Prob*),

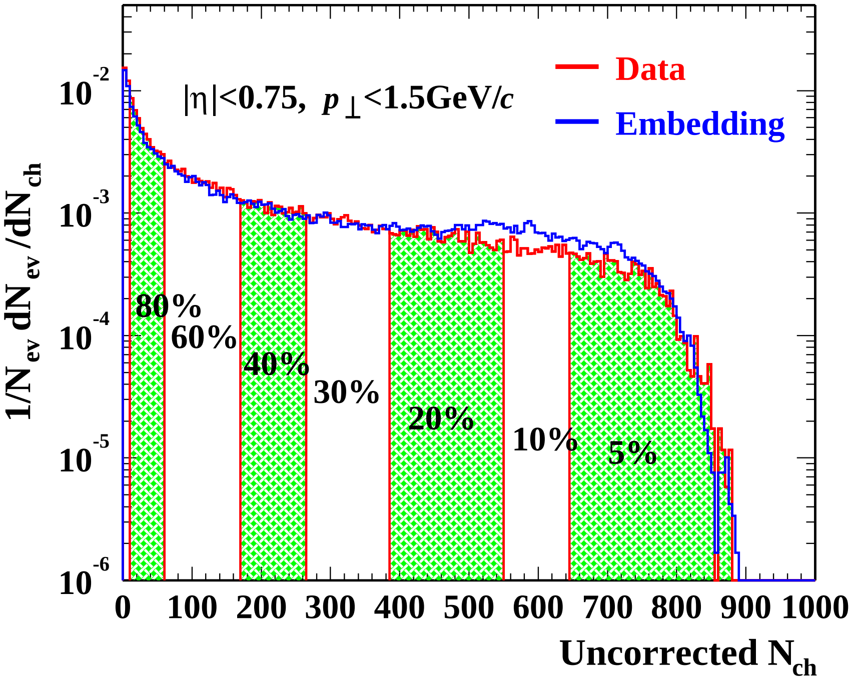

Figure 5.6: Uncorrected N_{ch} distribution in minimum bias data and in embedding data. The vertical lines show corresponding centrality cuts.

Table 5.2: Values of uncorrected charged particle multiplicity N_{ch} used in centrality cuts and their corresponding uncorrected and corrected N_{h^-}, and the average negatively charged particle density $\langle dN_{h^-}/d\eta \rangle$ in each centrality bin.

Centrality Bin	Percentage	Raw N_{ch}	Raw N_{h^-}	Corrected N_{h^-}	$\langle dN_{h^-}/d\eta \rangle$
1	0–5%	649	212	247.7	297
2	5–10%	547	179	206.7	243
3	10–20%	385	127	140.4	185
4	20–30%	261	86	91.5	123
5	30–40%	170	57	57.6	78.8
6	40–60%	58	20	19.0	38.3
7	60–80%	14	5	4.7	11.1

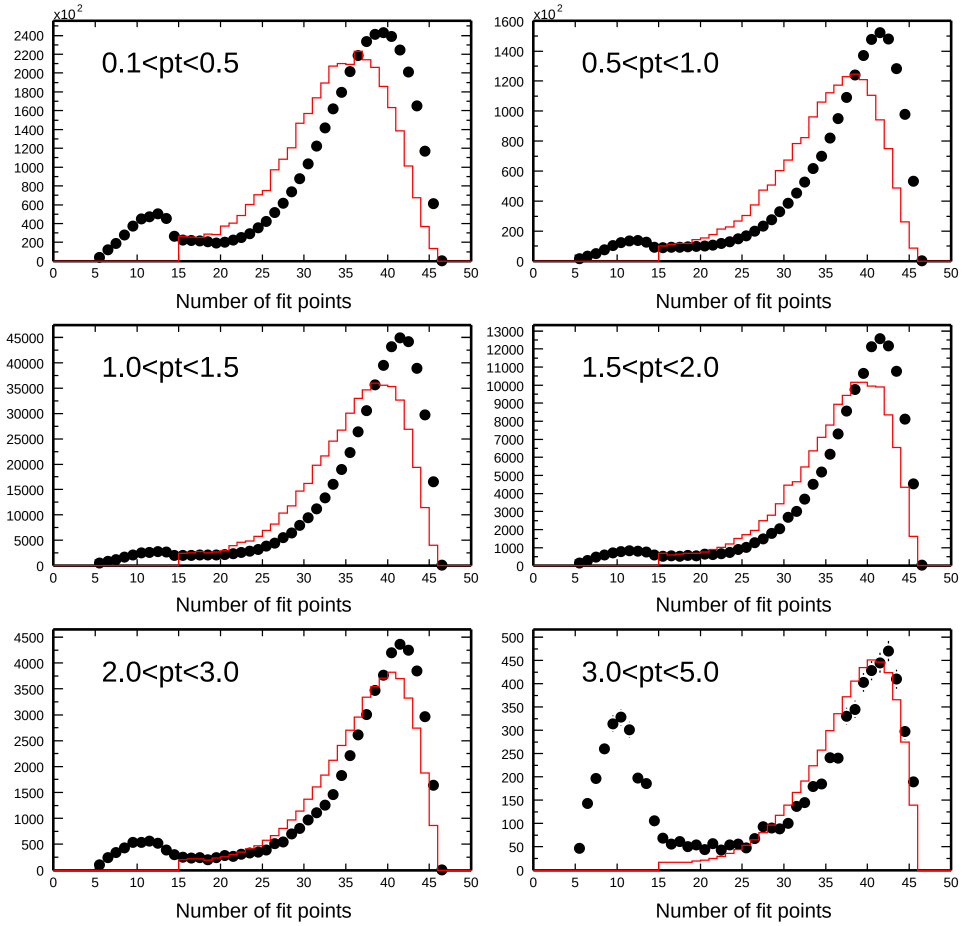

Figure 5.7: N_{fitpts} distribution for all primary tracks with flag > 0 in real data (points) and in embedding (histogram) within $|\eta| < 0.5$ for different p_T regions.

and on the distance of closest approach (DCA) from the associated global track to the primary vertex.

Fig. 5.7 and Fig. 5.8 show the number of fit points distribution. N_{fitpts} distributions for all primary tracks with flag > 0 within $|\eta| < 0.5$ for different p_T regions are shown in Fig. 5.7 as points for real tracks in data and histograms for simulated tracks in embedding. Fig. 5.8 shows N_{fitpts} distributions for $3 < p_T < 5$ GeV/c in different η regions. Fig. 5.9 and Fig. 5.10 show the distance of closest approach (DCA) distribution. DCA distributions for all primary tracks with flag > 0 and $N_{fitpts} \geq 15$ within

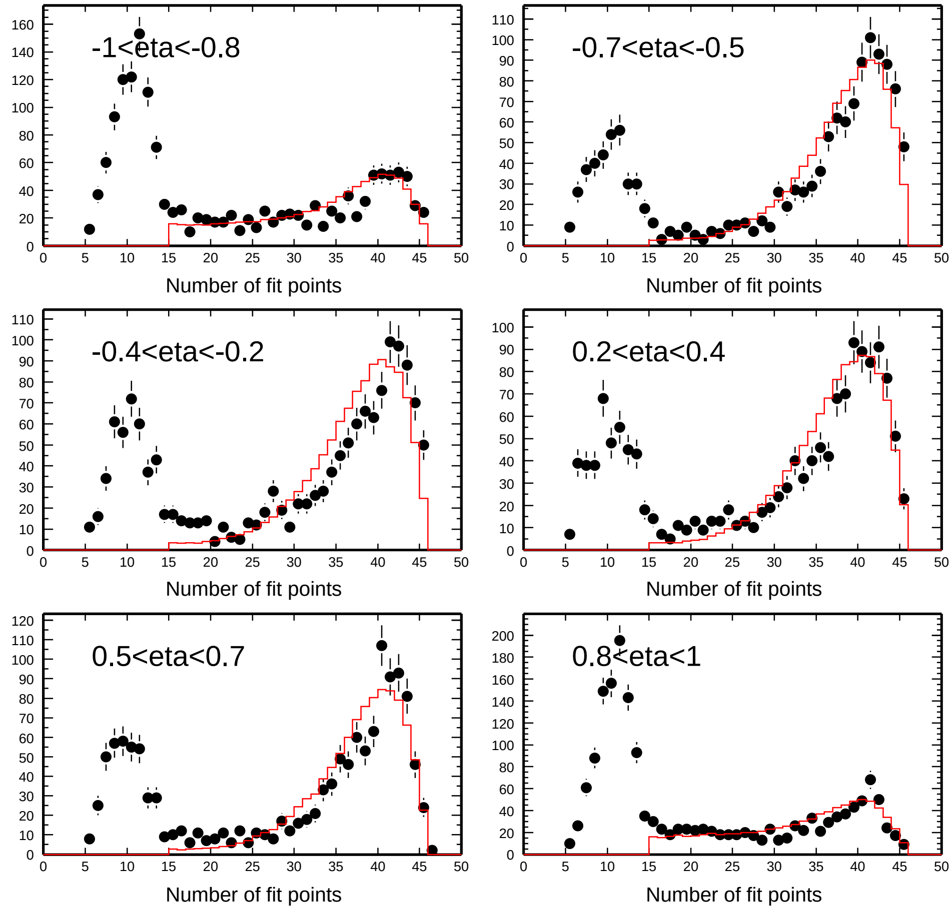

Figure 5.8: N_{fitpts} distribution for all primary tracks with flag > 0 in real data (points) and in embedding (histogram) for $3 < p_T < 5$ GeV/c in different η regions.

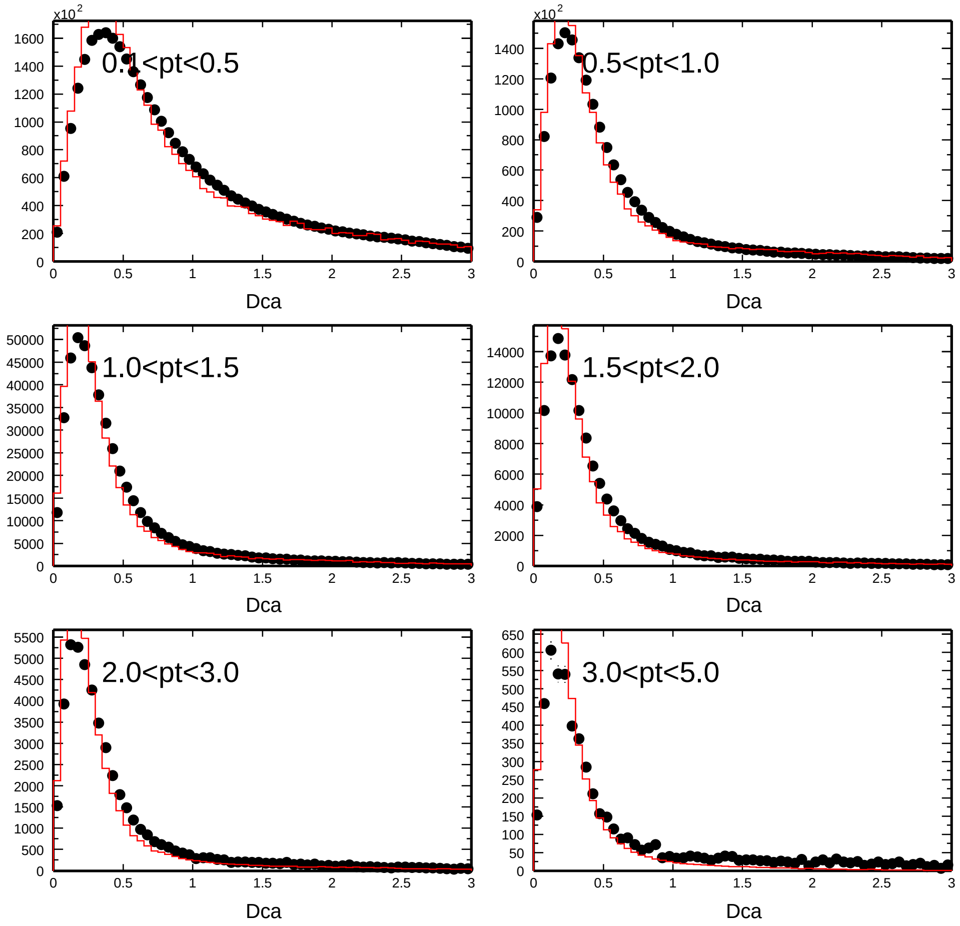

Figure 5.9: DCA distribution for all primary tracks with flag > 0 and $N_{fitpts} \geq 15$ in real data (points) and in embedding (histogram) within $|\eta| < 0.5$ for different p_T regions.

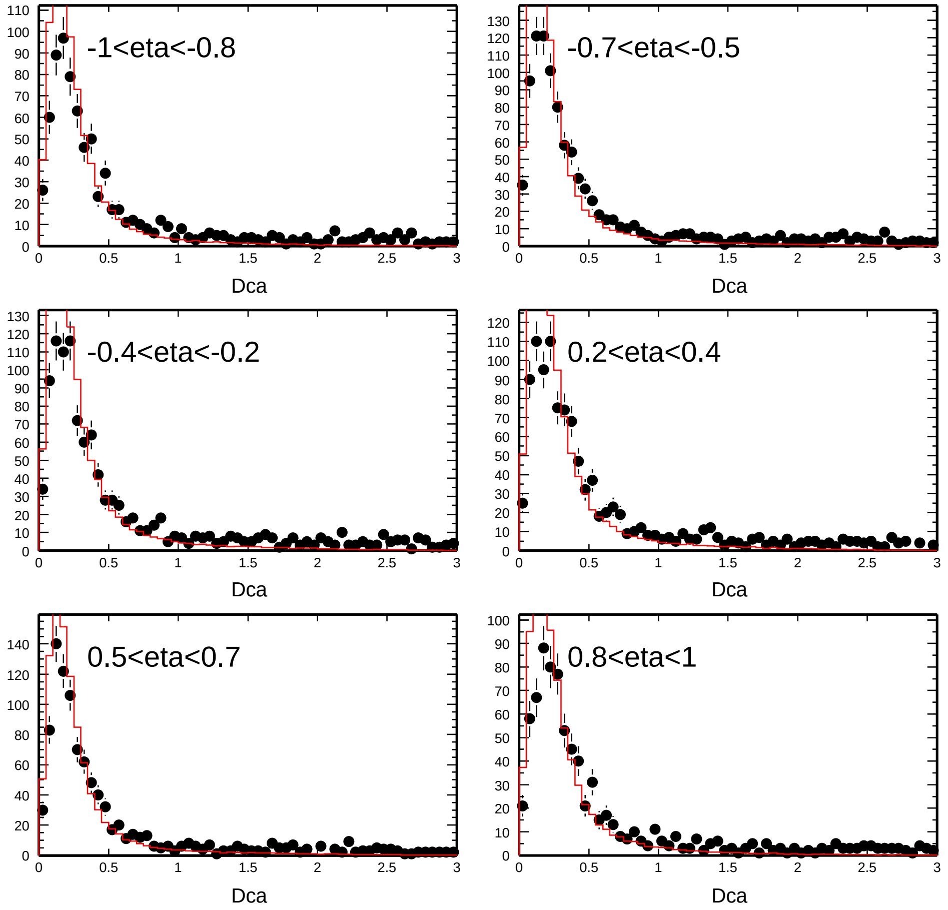

Figure 5.10: DCA distribution for all primary tracks with flag > 0 and $N_{fitpts} \geq 15$ in real data (points) and in embedding (histogram) for $3 < p_T < 5$ GeV/c in different η regions.

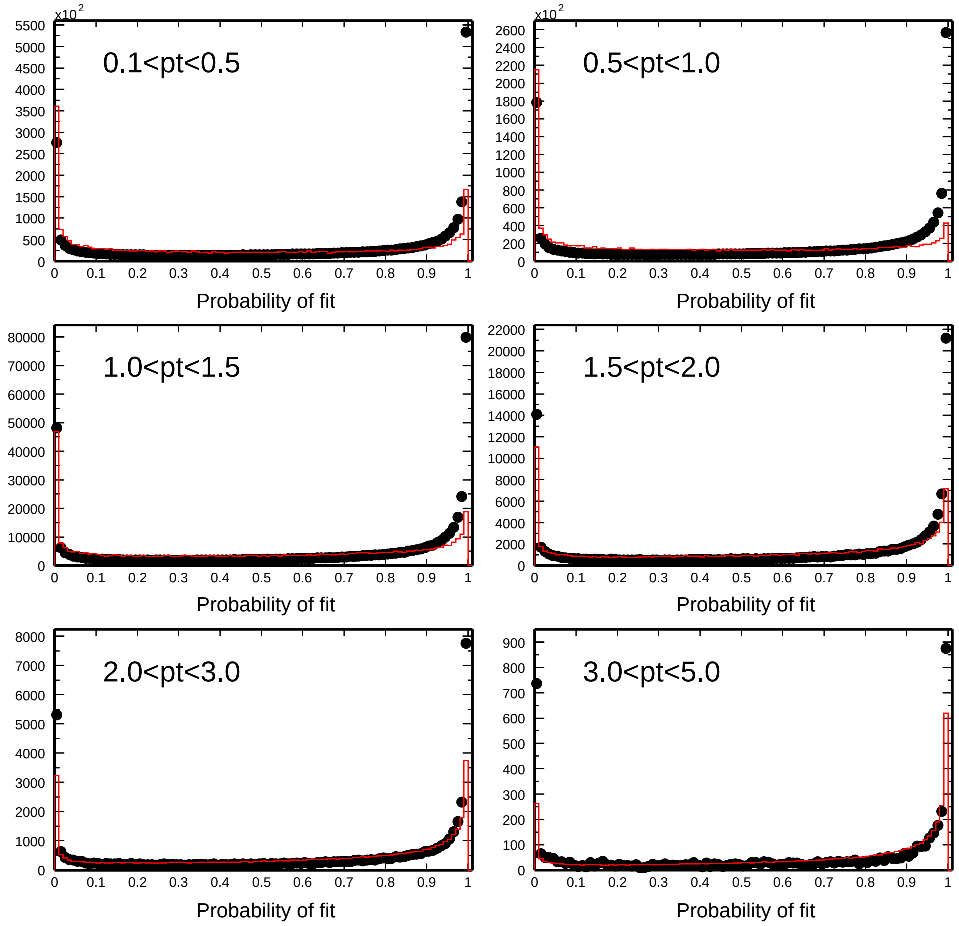

Figure 5.11: Probability of primary track fit distribution for all primary tracks with flag > 0, $N_{fitpts} \geq 15$, and $DCA < 2$ cm in real data (points) and in embedding (histogram) within $|\eta| < 0.5$ for different p_T regions.

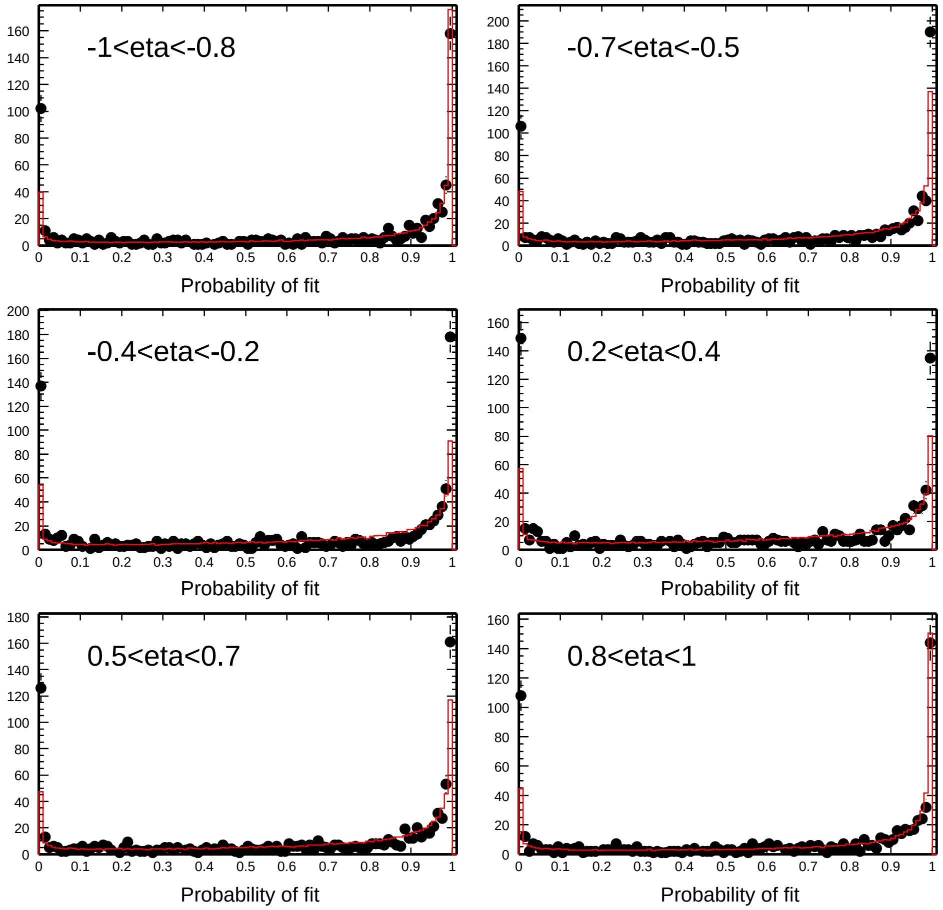

Figure 5.12: Probability of primary track fit distribution for all primary tracks with flag > 0, $N_{fitpts} \geq 15$, and $DCA < 2$ cm in real data (points) and in embedding (histogram) for $3 < p_T < 5$ GeV/c in different η regions.

$|\eta| < 0.5$ for different p_T regions are shown in Fig. 5.9. Fig. 5.10 shows DCA distributions for $3 < p_T < 5$ GeV/c in different η regions. Fig. 5.11 and Fig. 5.12 show the probability of primary track fit distribution. The probability of primary track fit distributions for all primary tracks with flag > 0, $N_{fitpts} \geq 15$, and $DCA < 2$ cm within $|\eta| < 0.5$ for different p_T regions are shown in Fig. 5.11. Fig. 5.12 shows the probability of primary track fit distributions for $3 < p_T < 5$ GeV/c in different η regions. The comparisons between the real tracks and the simulated tracks shown in all these figures are not perfect, but are satisfactory.

In order to estimate the systematic uncertainty due to these track quality cuts, we used a loose cut set and a tight cut set in data analysis as listed in Table 5.3. The p_T spectra obtained using both cuts are consistent within ±5% in the covered p_T range. Thus, a 5% systematic uncertainty is assigned to the final spectra.

Table 5.3: Values of two sets of track quality cuts used in the analysis. The cut set 1 and set 2 correspond to the loose and tight cuts, respectively.

Cut Set	N_{fitpts}	DCA	*Prob*
1	15	2 cm	0.01
2	25	1 cm	0.05

5.3.4 Spatial Distortions

The high p_T hadron yield is sensitive to small spatial distortions. A measurement of the summed hadron yield, $(h^+ + h^-)/2$, is less sensitive to such distortions than the yield of one charge sign alone. Using 12 sectors from each of the TPC ends as independent detectors for high p_T hadrons, we estimated the sectorwise (azimuthal coverage) variations of the yields to be less than 5%. The variation of the yield between the hadrons crossing and not crossing the central membrane of the TPC was found to be approximately proportional to p_T with a value of 11% at $p_T = 5.5$ GeV/c. Those variations of the raw yields in the east sectors of the TPC from h^-, h^+, and $(h^+ + h^-)/2$ are shown in Fig. 5.13 for $|\eta| < 0.5$ and in Fig. 5.14 for $0.5 < |\eta| < 1$. The variations of the raw yields in the west sectors of the TPC from h^-, h^+, and $(h^+ + h^-)/2$ crossing the central membrane are shown in Fig. 5.15 for $|\eta| < 0.5$ and in Fig. 5.16 for $0.5 < |\eta| < 1$.

5.4 Detection Efficiency

The acceptance and efficiency were determined by embedding simulated tracks into actual Au + Au collision events. In this analysis, the flat π^- distributions for $0 < p_T < 8$ GeV/c and $-1 < \eta < 1$ were generated at the real primary vertex, and these Monte Carlo (MC) simulated tracks were embedded into real events. The reconstructed hits will be associated with MC generated hits if they are within a maximum distance of 0.5 cm. The reconstructed tracks will be associated with MC generated tracks if they have at least 5 common hits.

The detection efficiency, ε, is defined as the ratio of the number of associated tracks over the number of input MC tracks, incorporating the detection acceptance and the tracking efficiency. The detection efficiency could be a function of p_T, η, centrality, etc. Fig. 5.17 shows the p_T dependence of the detection efficiency for cut set 1 within $|\eta| < 0.5$. The same for cut set 2 is shown in Fig. 5.18. Fig. 5.19 shows the η dependence of the detection efficiency for cut set 2 in the 0–5% most central bin. It can be seen that the detection efficiencies are almost flat within $-0.75 < \eta < 0.75$ and their drop at the highest η bin due to decreased acceptance is less than 30%. Fig. 5.20 shows the centrality dependence of the detection efficiency for cut set 2 within $|\eta| < 0.5$. It is

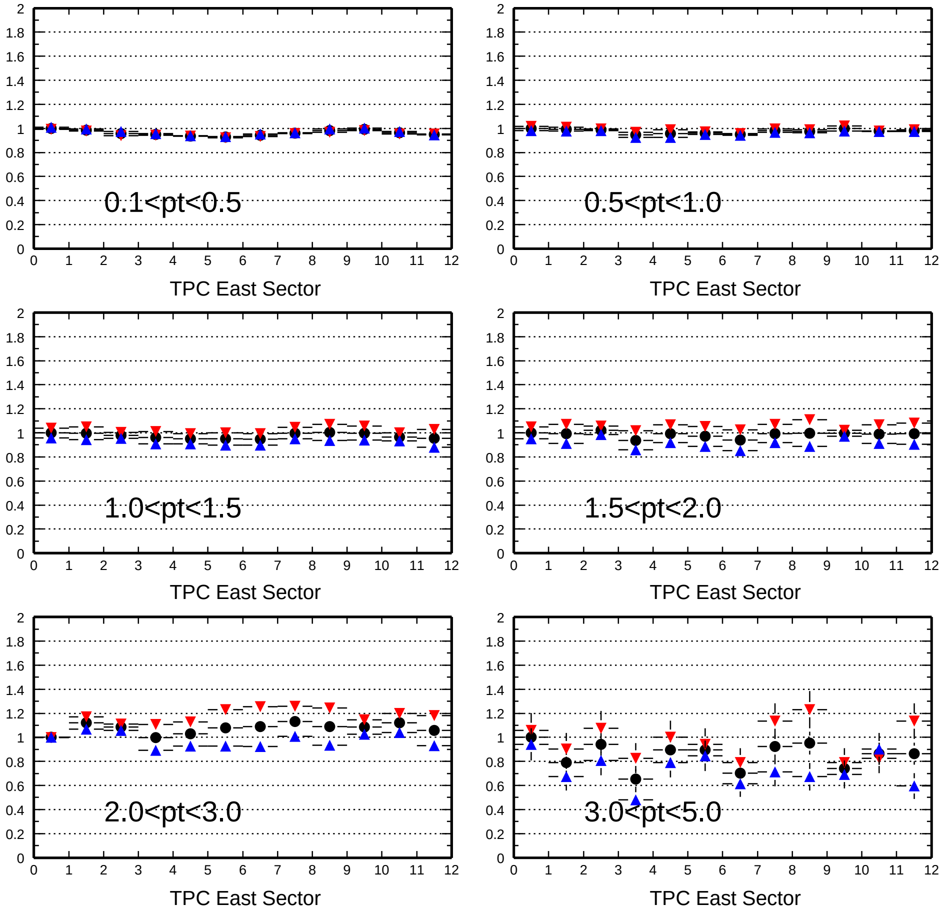

Figure 5.13: Variations of the raw yields in the 12 east sectors of the TPC for those tracks passed cut set 1 within $|\eta| < 0.5$ for different p_T regions. The upward and downward triangles represent the negatively (h^-) and positively (h^+) charged particles, respectively. The dots represent all charged particles, $(h^+ + h^-)/2$. All yields are normalized to the yield of the $(h^+ + h^-)/2$ in sector 1.

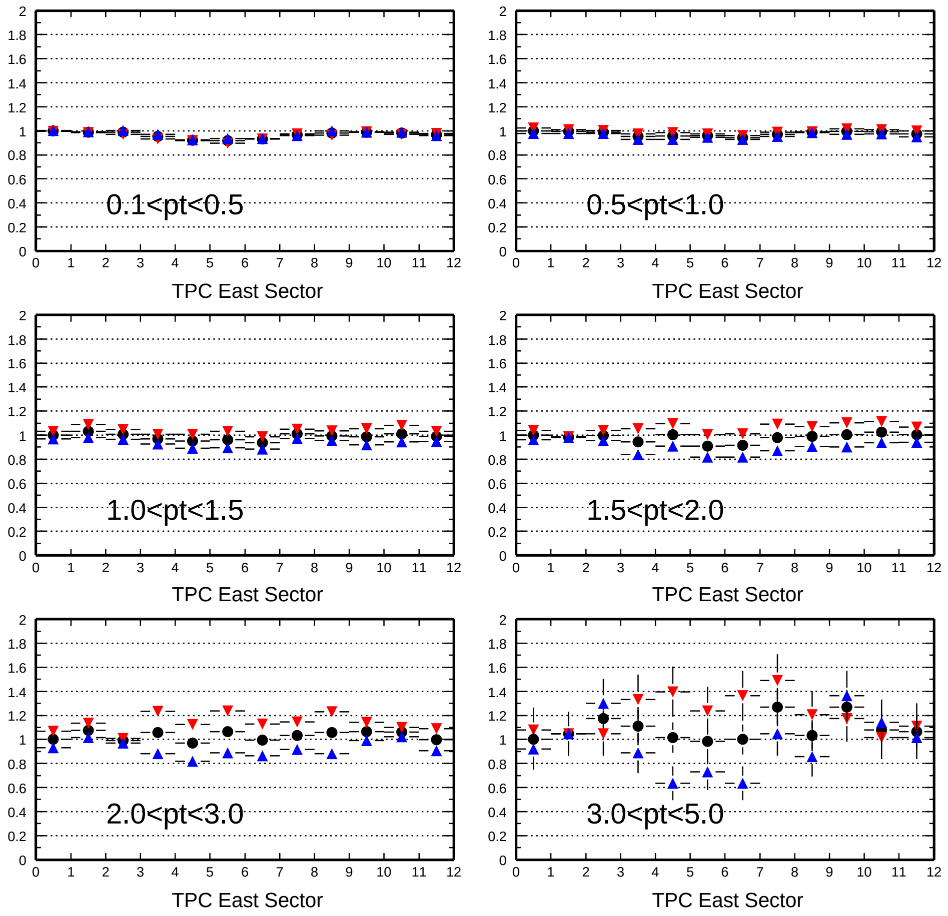

Figure 5.14: Variations of the raw yields in the 12 east sectors of the TPC for those tracks passed cut set 1 within $0.5 < |\eta| < 1$ for different p_T regions. The upward and downward triangles represent the negatively (h^-) and positively (h^+) charged particles, respectively. The dots represent all charged particles, $(h^+ + h^-)/2$. All yields are normalized to the yield of the $(h^+ + h^-)/2$ in sector 1.

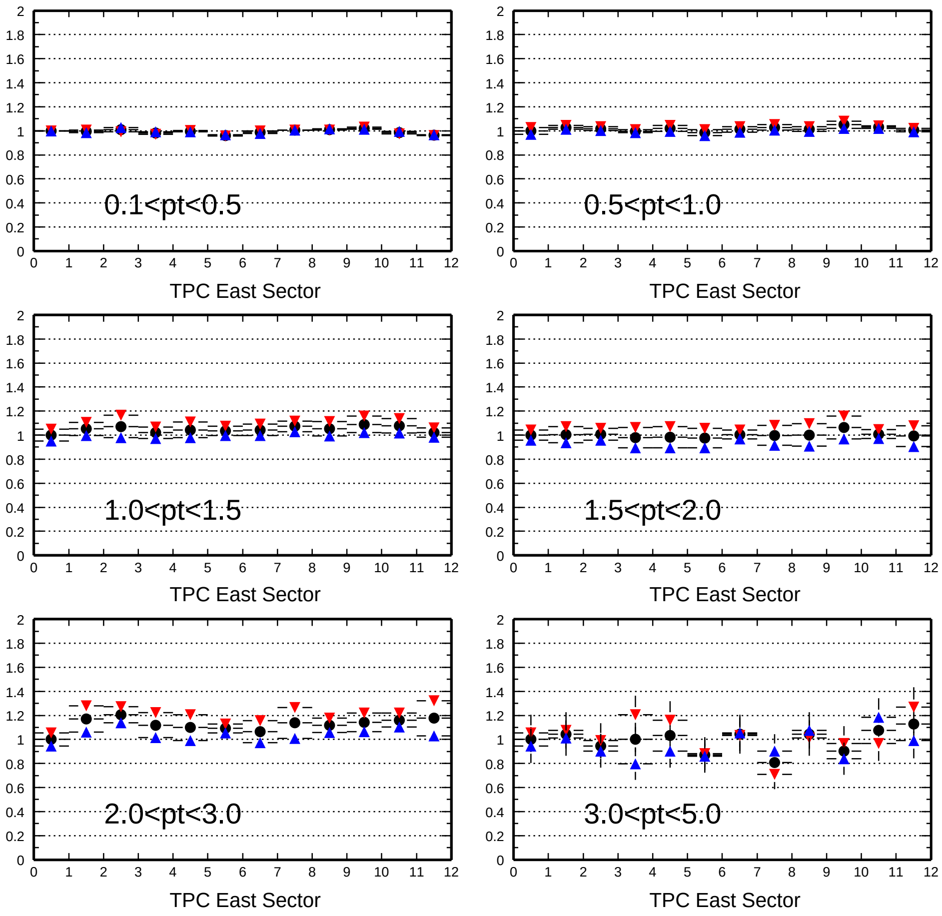

Figure 5.15: Variations of the raw yields in the 12 west sectors of the TPC for those tracks crossing the central membrane and passed cut set 1 within $|\eta| < 0.5$ for different p_T regions. The upward and downward triangles represent the negatively (h^-) and positively (h^+) charged particles, respectively. The dots represent all charged particles, $(h^+ + h^-)/2$. All yields are normalized to the yield of the $(h^+ + h^-)/2$ in sector 1.

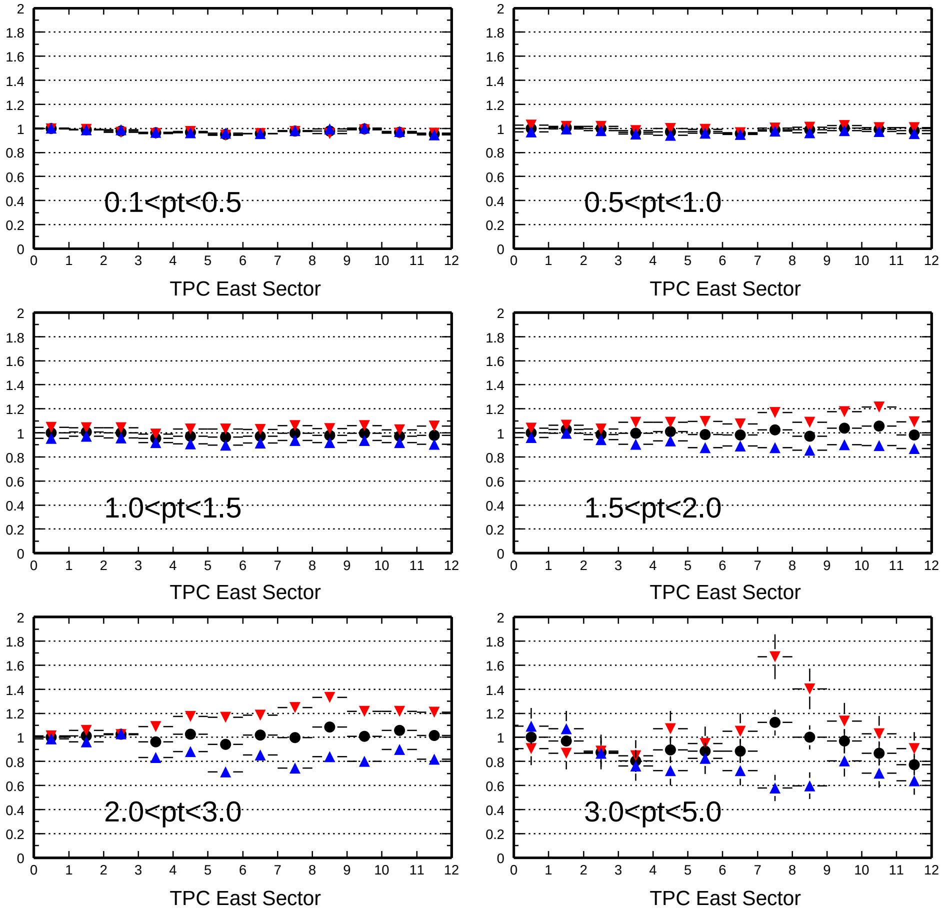

Figure 5.16: Variations of the raw yields in the 12 west sectors of the TPC for those tracks crossing the central membrane and passed cut set 1 within $0.5 < |\eta| < 1$ for different p_T regions. The upward and downward triangles represent the negatively (h^-) and positively (h^+) charged particles, respectively. The dots represent all charged particles, $(h^+ + h^-)/2$. All yields are normalized to the yield of the $(h^+ + h^-)/2$ in sector 1.

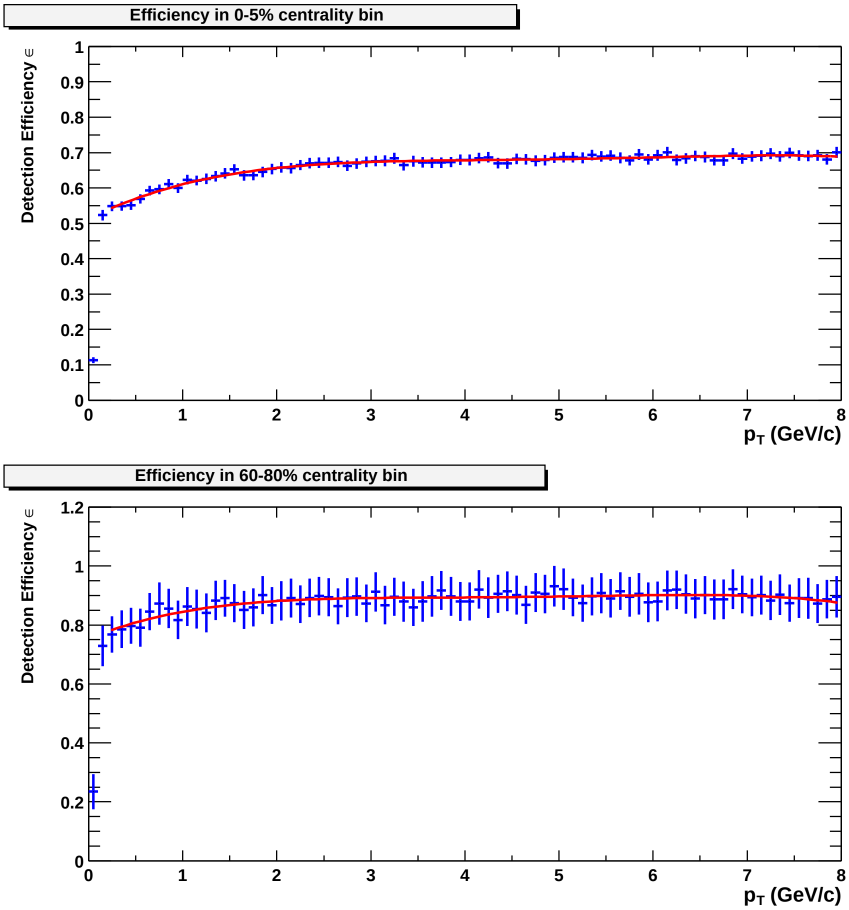

Figure 5.17: Detection efficiency as a function of p_T for cut set 1 within $|\eta| < 0.5$. The upper panel is for centrality bin 1, the 0–5% most central bin. The lower panel is for centrality bin 7, the 60–80% most peripheral bin.

observed that the detection efficiency decreases as the multiplicity increases in all p_T cases because the tracking efficiency becomes lower in higher multiplicity events.

The typical multiplicative correction factors for the acceptance and efficiency, $F_{eff} = 1/\varepsilon$, are given in Table 5.4 as “Tracking”. Their systematic uncertainties incorporate acceptance, efficiency, track quality cuts, and the effects of the spatial nonuniformity.

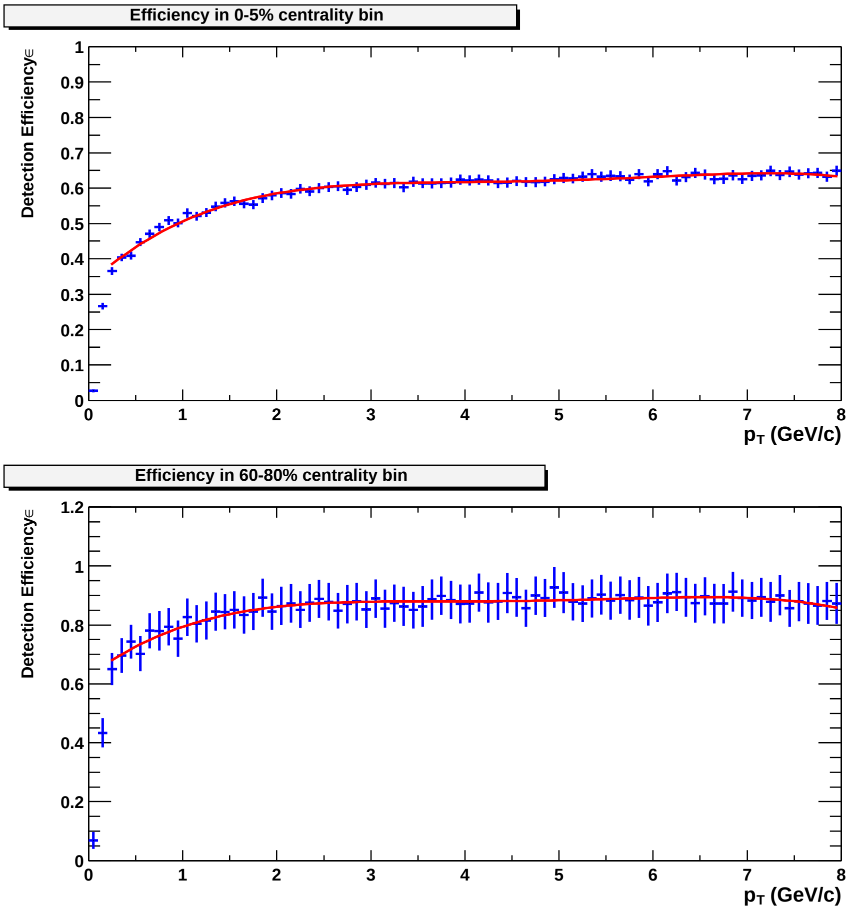

Figure 5.18: Detection efficiency as a function of p_T for cut set 2 within $|\eta| < 0.5$. The upper panel is for centrality bin 1, the 0–5% most central bin. The lower panel is for centrality bin 7, the 60–80% most peripheral bin.

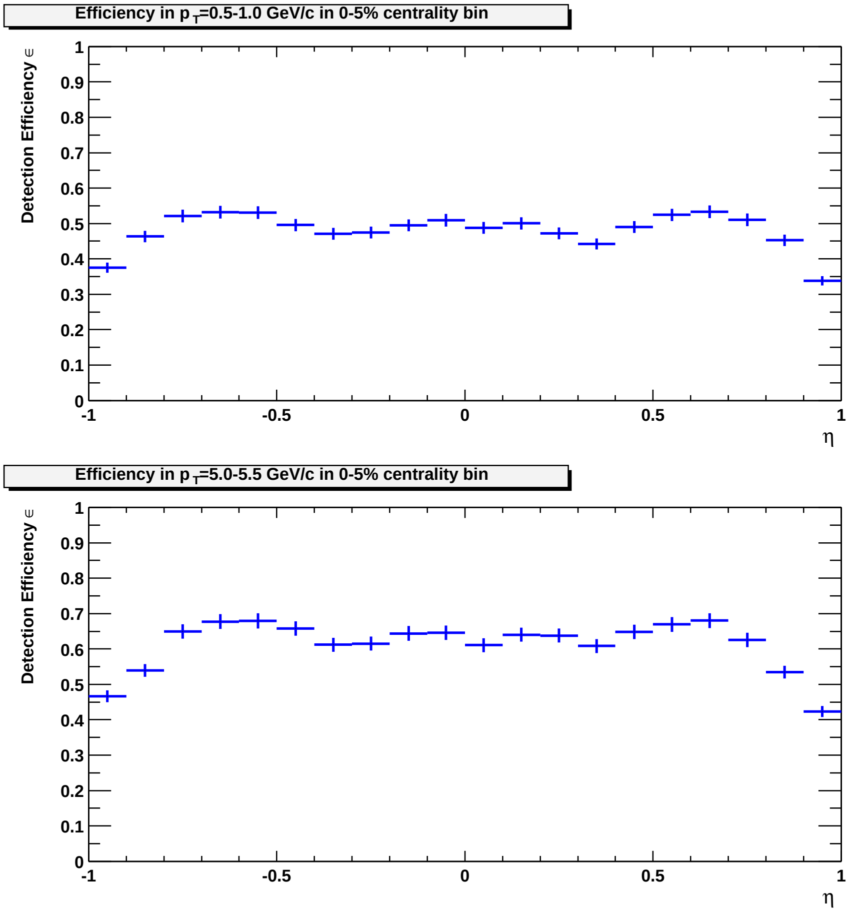

Figure 5.19: Detection efficiency as a function of η for cut set 2 in the 0–5% most central bin. The upper panel is for $0.5 < p_T < 1.0$ GeV/c. The lower panel is for $5.0 < p_T < 5.5$ GeV/c.

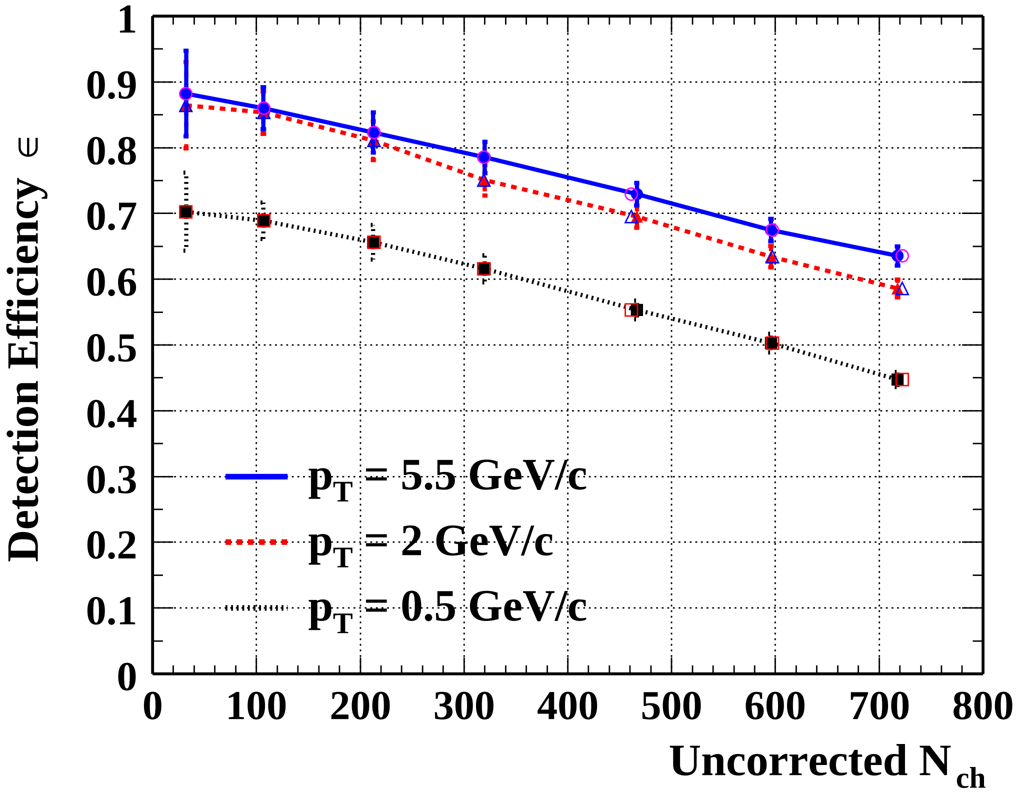

Figure 5.20: Detection efficiency as a function of centrality represented by uncorrected N_{ch} for cut set 2 within $|\eta| < 0.5$. The squares, triangles, and circles are for $p_T = 0.5$, 2, 5.5 GeV/c, respectively. Curves are to guide eyes. The filled or open symbols correspond to the centrality cuts by N_{ch} which included or excluded the embedded tracks. Little differences can be seen in all cases.

5.5 p_T Smearing Correction

Finite momentum resolution tends to shift particles to neighboring bins. This p_T smearing effect cannot be neglected when p_T resolution gets larger at higher p_T where the momentum resolution is limited by the strength of the magnetic field and the TPC spatial resolution. The track curvature $k(= q/p_T)$ with the charge $q = -1$ or +1 is directly from the Kalman fit, and its distribution is a Gaussian function. Considering a p_T distribution $f(p_T)$ (e.g., the power law function Eq. 3.1), we expect the yield in a p_T interval i with the width of $\Delta p_T^i = p_T^u - p_T^l$ should be

$$N_i^{exp}(p_T^i) = \int_{p_T^l}^{p_T^u} f(p_T) dp_T \tag{5.5}$$

if there is no p_T smearing. However, the measured raw yield $N_i^{meas}(p_T^i)$ is comparable with

$$N_i^{meas}(p_T^i) \sim \int_{p_T^l}^{p_T^u} f(p_T)\varepsilon(p_T) dp_T, \tag{5.6}$$

where $\varepsilon(p_T)$ is the detection efficiency as a function of p_T. With the expected yield $N_i^{exp}(p_T^i)$, we define the multiplicative detection efficiency correction factor

$$F_{eff}(p_T^i) = \frac{N_i^{exp}(p_T^i)}{N_i^{meas}(p_T^i)} \sim 1/\varepsilon(p_T^i). \tag{5.7}$$

If the p_T smearing must be taken into account and a Gaussian smearing function is expected, the smeared yield would be

$$\begin{aligned} N_i^{smear}(p_T^i) &= \int_{p_T^l}^{p_T^u} \int_{k=0}^{\infty} f(k)\varepsilon(k) \frac{1}{\sqrt{2\pi}\sigma(k)} \exp\left(-\frac{(\frac{1}{p_T} - k)^2}{2\sigma^2(k)} \right) d(\frac{1}{k})\ d(\frac{1}{p_T}) \\ &= \int_{p_T^l}^{p_T^u} \frac{dp_T}{p_T^2} \int_{k=0}^{\infty} \frac{f(k)\varepsilon(k)}{\sqrt{2\pi}\sigma(k)k^2} \exp\left(-\frac{(\frac{1}{p_T} - k)^2}{2\sigma^2(k)} \right) dk. \end{aligned} \tag{5.8}$$

Then a parameterization can be performed by minimizing the following χ^2

$$\chi^2 = \sum_i \frac{(N_i^{meas}(p_T^i) - N_i^{smear}(p_T^i))^2}{N_i^{meas}(p_T^i)}. \tag{5.9}$$

The multiplicative p_T smearing correction factor can thus be defined as

$$F_{smear}(p_T^i) = \frac{\int_{p_T^l}^{p_T^u} f(p_T)\varepsilon(p_T)dp_T}{N_i^{smear}(p_T^i)}. \tag{5.10}$$

The width of p_T broadening $\sigma(p_T)$ is determined not only by the p_T resolution but also by other sources such as the primary vertex resolution.

We used the embedding technique to determine the magnitude of the p_T resolution as it is defined by the difference between the reconstructed p_T and the MC generated p_T. For $p_T < 0.5$ GeV/c, the p_T resolution is dominated by multiple Coulomb scattering and increases as the p_T decreases. For $p_T > 0.5$ GeV/c, the Gaussian distribution of track curvature $k \propto 1/p_T$ has a relative width of $\delta k/k = 0.013 + 0.015 p_T/(\text{GeV}/c)$ for central events and $\delta k/k = 0.012 + 0.012 p_T/(\text{GeV}/c)$ for peripheral events within $|\eta| < 0.5$, and $\delta k/k = 0.014 + 0.010 p_T/(\text{GeV}/c)$ for central events and $\delta k/k = 0.014 + 0.0072 p_T/(\text{GeV}/c)$ for peripheral events within $0.5 < |\eta| < 1$. The fact that the p_T resolution within $0.5 < |\eta| < 1$ is better than that within $|\eta| < 0.5$ is due to the competition between two opposite effects. For a given p_T, the hadron with higher η tends to have less space points and shorter drift distance in the TPC than that with lower η. The less space points or the longer drift distance a track has, the poorer its momentum resolution. Fig. 5.21 reveals these two effects demonstrated for $5.0 < p_T < 5.5$ GeV/c in both the most central bin and the most peripheral bin. In the range of $0 < |\eta| < 0.7$, the effect of drift distance dominates. Only in the range of $0.7 < |\eta| < 1$ where the acceptance drops can the effect of the space points become dominated.

However, the magnitude of the p_T resolution determined from the embedding tech-

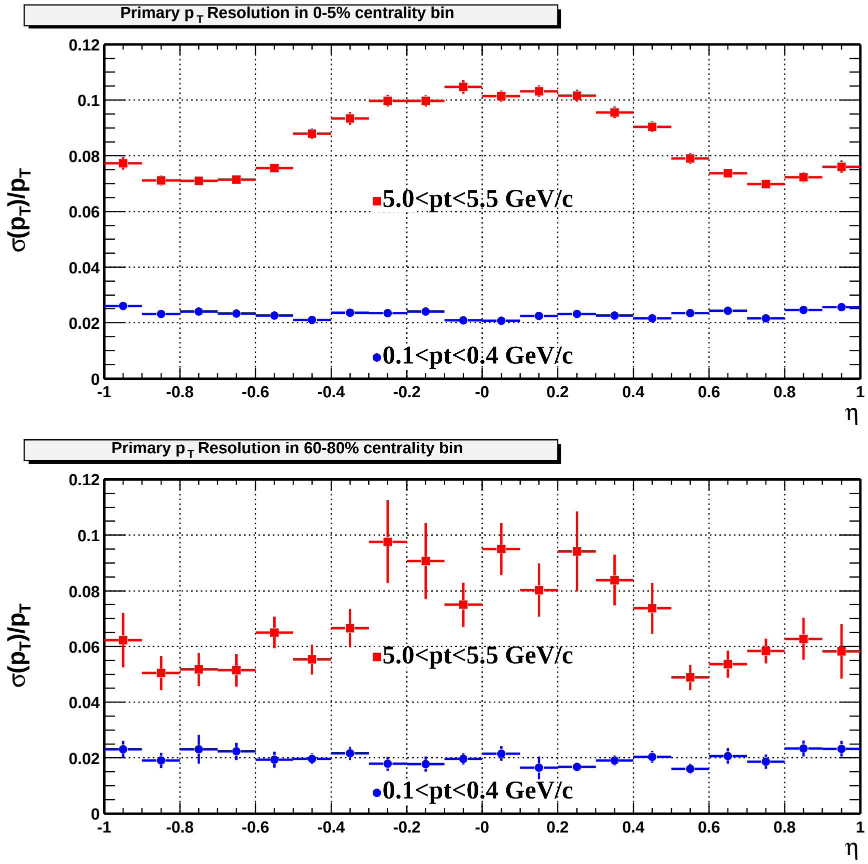

Figure 5.21: The η dependence of the p_T resolution for high p_T and low p_T in the 0–5% most cantral bin (upper panel) and the 60–80% peripheral bin (lower panel).

nique did not include the effect of the primary vertex resolution. In the embedding procedure a simulated track is embedded with a known vertex position determined by the real tracks and the precise vertex was used in p_T fitting for the simulated track. We developed a procedure to take into account the effect of the primary vertex resolution and possible other effects such as charge sign dependent distortion and background particles in the p_T smearing correction. The global tracks in the TPC are reconstructed without the constraint of a vertex, thereby providing a common reference for both the embedded and real primary tracks. In the same p_T bin, the width of Gaussian distribution of the difference between global and primary track curvatures for real tracks is observed to be always larger than that for embedded tracks. The broadening of the width in real tracks is due mainly to the primary vertex resolution and the charge sign dependent distortion, and, partially to background tracks which are mostly from weakly decayed daughters and have a larger p_T smearing than true primary tracks. The contribution from background tracks, $\sim 10\%$, is estimated using HIJING Monte Carlo simulation events with HIJING yields scaled to match measurements of weakly decayed particle spectra [Adl02b, Adl02c]. Therefore, the effect of the p_T smearing due to the primary vertex resolution, the charge sign dependent distortion, and weak decay backgound tracks has been empirically derived from the comparison between real data and embedded tracks. The effect within $0.5 < |\eta| < 1$ was found to be larger than that within $|\eta| < 0.5$, which is partially due to the fact that the magnitude of the charge sign dependent distortion in higher η region is larger.

We plot the p_T smearing correction factors for two η regions in the 5% most central bin in Fig. 5.22: $|\eta| < 0.5$ in the upper panel and $0.5 < |\eta| < 1$ in the lower panel. The dashed curve represents the contribution from the p_T resolution while the dotted curve represents the contribution from the primary vertex resolution. Overall correction factors are shown as the solid curves which are obtained by assuming that the two contributions are independent, and can thus be combined quadratically. Because the two contributions have opposite effects in $|\eta|$ direction, the overall p_T smearing correction factors for the two η regions happen to be comparable as shown in the lower panel as the dot-dashed curve for the ratio. Systematic uncertainties are shown as the shaded areas in the figure. In order to estimate the systematic uncertainty, we calculated the correction factors by varying the embedded p_T resolution and the contribution from the primary vertex resolution etc. by ±5% and ±10%, respectively. Another 10% was applied to the significance of the overall correction factor, i.e., $(1-F_{smear}) \times 10\%$, to account for the systematic uncertainty due to the p_T smearing method, in which we assumed the p_T spectrum is well described by the pQCD inspired power law function Eq. 3.1. The typical p_T smearing correction factors and their systematic uncertainties are also given in Table 5.4.

5.6 Background

The most significant backgrounds for the high p_T charged hadron yield come from particle weak decays and antinucleon annihilation in detector material. The contamination rate, which is defined by the ratio of the background tracks passing all applied cuts with respect to the all measured tracks (signal + backgound), was estimated for each background source using detector response simulations with events generated by HIJING model [GW94]. Fig. 5.23 shows the contamination rates from the weak decay particles K_S^0 and $(\Lambda + \overline{\Lambda})$, antinucleons ($\bar{p}$ + $\bar{n}$), and photon conversions and track splitting etc. for the track quality cut set 2 within $|\eta| < 0.5$.

However, the production yields of weak decay particles, primarily K_S^0, Λ, $\overline{\Lambda}$, and antinucleons, $\bar{p}$, $\bar{n}$, in HIJING are not consistent with experimental measurements. We corrected those production yields using the measured spectra of $\bar{p}$ [Adc02, Adl01c], Λ and $\overline{\Lambda}$ [Adl02b], and K_S^0 [Adl02c], together with those of h^- [Adc02, Adl01b], for

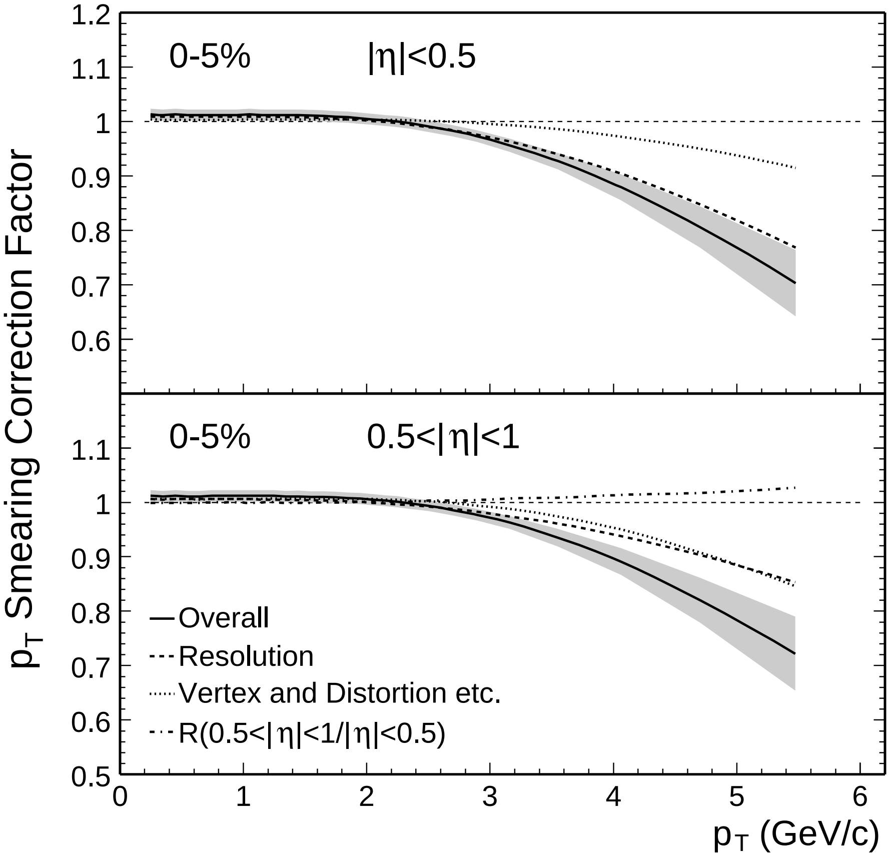

Figure 5.22: p_T smearing correction factors for two η regions in the 0–5% most central bin. Solid curves are overall correction factors while dashed and dotted curves represent contributions from the p_T resolution and the primary vertex resolution etc., respectively.

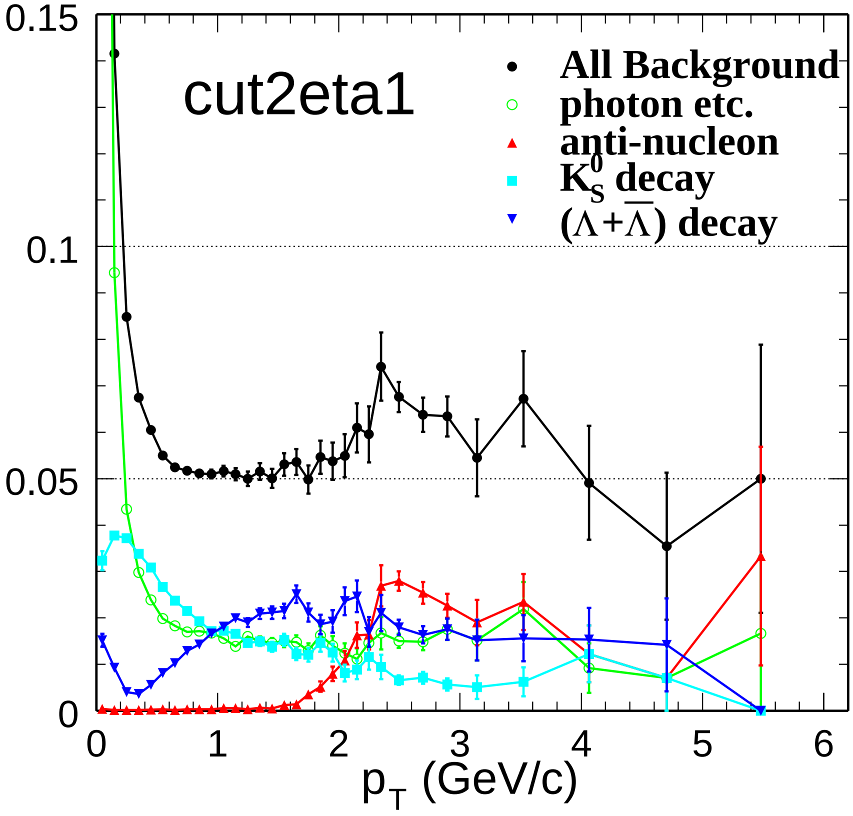

Figure 5.23: Background contamination rates from various sources for the track quality cut set 2 within $|\eta| < 0.5$ based on the HIJING Monte Carlo simulation events.

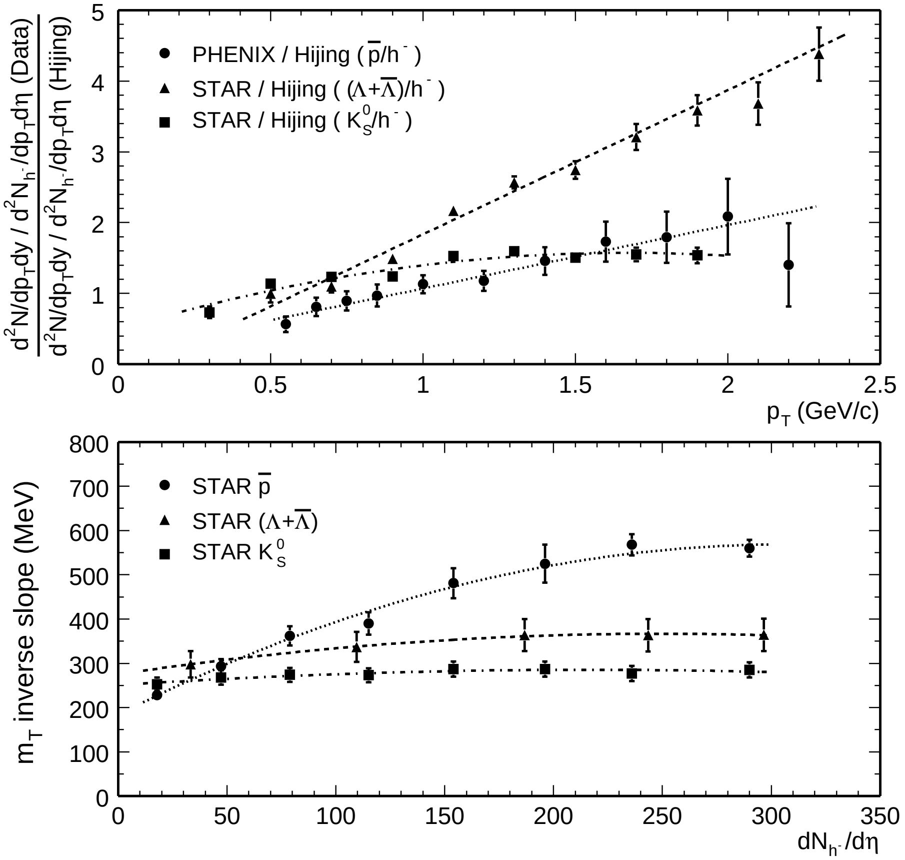

Figure 5.24: Upper panel: ratios of the measured p_T yield ratios to those of HIJING produced ones in the most central bin. Lower panel: measured m_T inverse slope parameters as a function of centrality represented by measured negatively charged hadron multiplicity. Curves are polynomial fits to data points.

$p_T < 2.4$ GeV/c in mid-rapidity region in the most central bin. The corrections used in calculating the background fractions from the HIJING events are shown in the upper panel of Fig. 5.24. The curves are polynomial fits to the data points and are used in the interpolation due to different p_T binning. For $p_T > 2.4$ GeV/c we simply assumed the yield ratios to be constant. A systematic uncertainty of 50% or 100% to overall background fraction is assigned for the range of $p_T < 2.4$ GeV/c or $p_T > 2.4$ GeV/c, respectively.

The contamination rate for all background sources shows almost no centrality de-

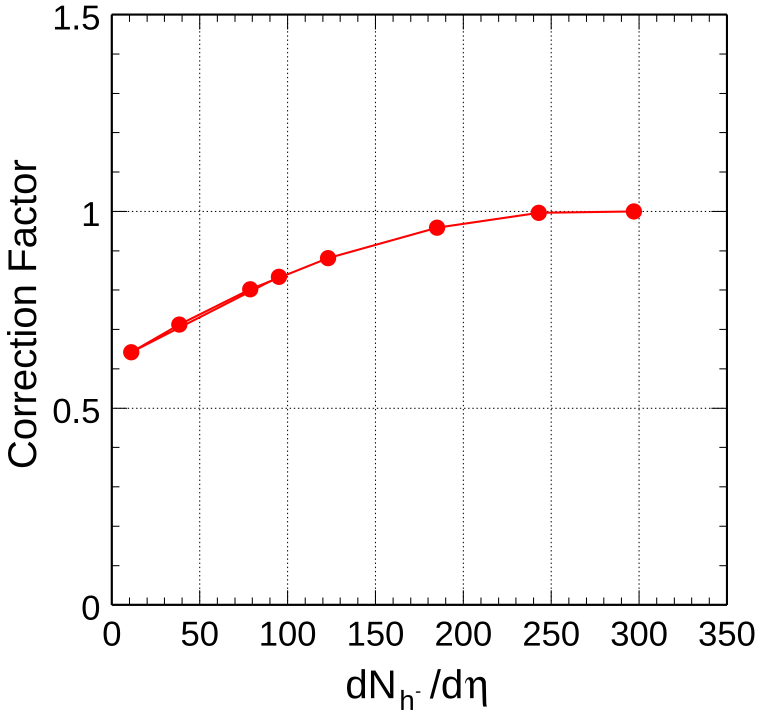

Figure 5.25: Background correction factor normalized to that in the 0–5% most central bin as a function of the multiplity by weighting the various weak decay sources from measurements.

pendence from the Monte Carlo HIJING events. Therefore, the centrality dependence of the background fraction is mainly determined by the measured spectra in various centrality bins. In order to eliminate the effects of different centrality binning, we plot the measured transverse mass ($m_T = \sqrt{p_T^2 + m_0^2}$) inverse slope parameters of exponential distributions for $\bar{p}$, Λ and $\bar{\Lambda}$, and K_S^0 in mid-rapidity region as functions of the measured negatively charged hadron multiplicity in the lower panel of Fig. 5.24. The polynomial fits are used to interpolate the inverse slope parameters in the centrality bins used in this analysis. Weighting the different weak decay contributions, we obtained the centrality dependence of the background correction factor shown as normalized to that in the 0–5% most central bin in Fig. 5.25.

The pseudorapidity dependence of the background fraction is again studied using the Monte Carlo HIJING events. Fig. 5.26 shows the η dependence of all background contamination rate in the ranges of $p_T > 0.5$, 1, 2, and 3 GeV/c. The curves are the Gaussian fits. For $p_T < 2$ GeV/c the η dependence of backgrounds is negligible within $-1 < \eta < 1$ while for $p_T > 2$ GeV/c the background fraction decreases with p_T and $|\eta|$. For example, at $p_T = 5.5$ GeV/c the background fraction within $0.5 < |\eta| < 1$ is only 40% of that within $|\eta| < 0.5$. This could be due to different effects on signal and background (mainly weak decay daughters) tracks when the acceptance changes. After weighting from measurements according to the upper panel of Fig. 5.24 and correcting $|\eta|$ region effects, we plot the backgound fractions within $|\eta| < 0.5$ and within $0.5 < |\eta| < 1$ as functions of p_T for the 0–5% most central bin in Fig. 5.27. The backgound fractions for other centrality bins can be obtained from the centrality dependence shown in Fig. 5.25. The typical multiplicative background correction factors, $F_{bkgd} = 1-$(background fraction), and their systematic uncertainties are given in Table 5.4.

After all corrections are made, the total systematic uncertainties of the measured spectra within $|\eta| < 0.5$ ($0.5 < |\eta| < 1$) at the highest bin $p_T = 5.5$ GeV/c are $\approx 24\%$ ($\approx 18\%$) for central events and $\approx 17\%$ ($\approx 15\%$) for peripheral events.

Table 5.4: Typical multiplicative correction factors and their systematic uncertainties, applied to the yields for peripheral and central collisions within $|\eta| < 0.5$ and within $0.5 < |\eta| < 1$.

Pseudorapidity		$p_T = 2$ GeV/c		$p_T = 5.5$ GeV/c	
	Centrality	60–80%	0–5%	60–80%	0–5%
$\|\eta\| < 0.5$	Tracking	1.16 ± 0.10	1.71 ± 0.15	1.22 ± 0.16	1.65 ± 0.22
	p_T Smearing	1.01 ± 0.01	1.00 ± 0.01	0.89 ± 0.02	0.70 ± 0.06
	Background	0.92 ± 0.04	0.88 ± 0.06	0.90 ± 0.10	0.85 ± 0.15
$0.5< \|\eta\| <1$	Tracking	1.29 ± 0.11	1.78 ± 0.15	1.31 ± 0.18	1.71 ± 0.23
	p_T Smearing	1.01 ± 0.01	1.01 ± 0.01	0.89 ± 0.02	0.72 ± 0.07
	Background	0.92 ± 0.04	0.88 ± 0.06	0.96 ± 0.10	0.94 ± 0.06

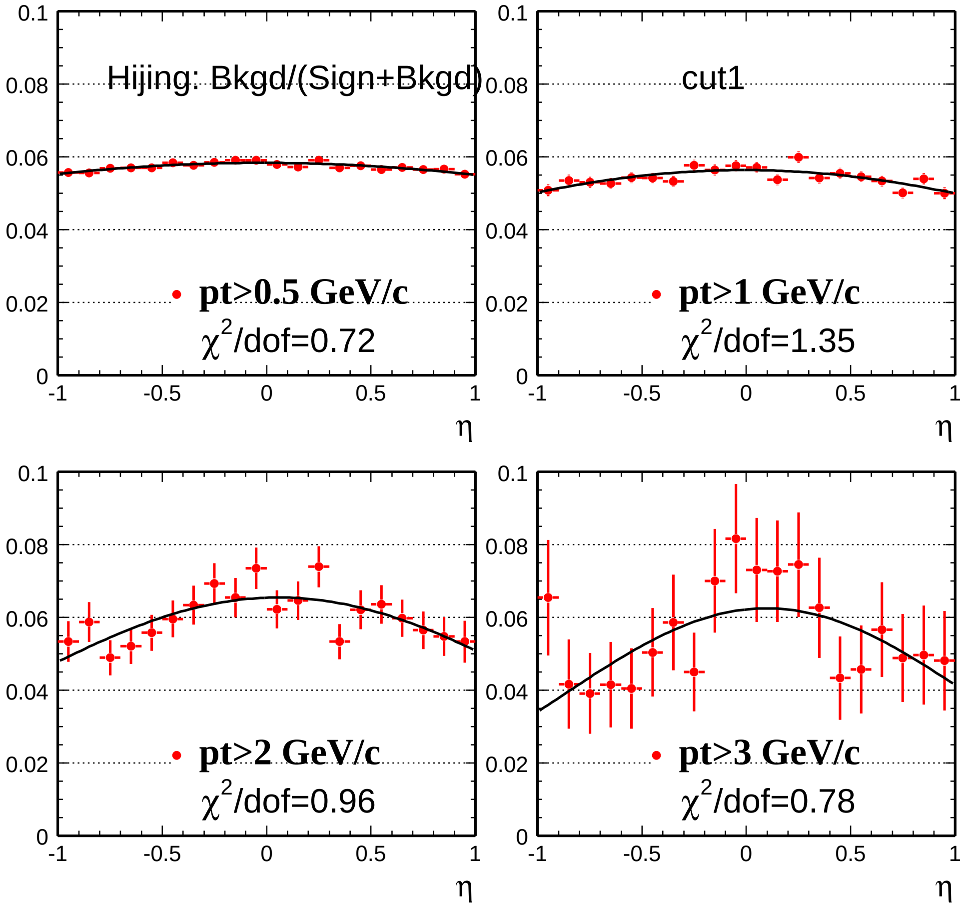

Figure 5.26: The η dependence of all background contamination rate in the ranges of $p_T > 0.5$, 1, 2, and 3 GeV/c. The curves are the Gaussian fits.

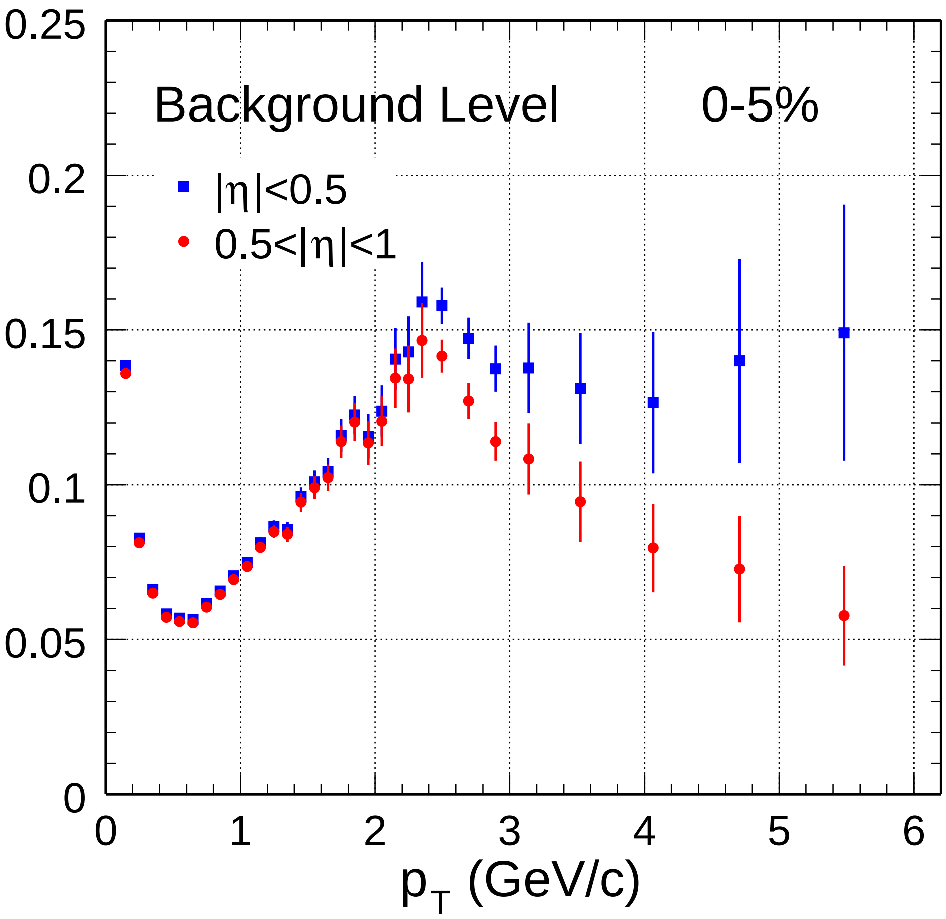

Figure 5.27: The η dependence of all background contamination rate in the ranges of $p_T > 0.5$, 1, 2, and 3 GeV/*c*. The curves are the Gaussian fits.

CHAPTER 6

Results

6.1 Transverse Momentum Spectrum

Inclusive p_T distributions of $(h^+ + h^-)/2$ within $|\eta| < 0.5$ are shown in Fig. 6.1 for various centrality bins. The error bars are the quadrature sum of statistical error and systematic uncertainty, and are dominated by the latter except for the highest p_T point in the peripheral bins. The curves in the figure are the power law function (Eq. 3.1) fits to the spectra. Fig. 6.2 shows inclusive p_T distributions of $(h^+ + h^-)/2$ within $0.5 < |\eta| < 1$ for various centrality bins.

Fig. 6.3 shows ratios of p_T distributions within $0.5 < |\eta| < 1$ to those within $|\eta| < 0.5$ in various centrality bins. The error bars show statistical errors only while the caps are the quadrature sum of statistical errors and systematic uncertainties which cannot be cancelled out. Remaining systematic uncertainty includes the variation due to track quality cuts, the uncertainties of the p_T smearing corrections for the two η regions, and the partial uncertainty of background subtraction related to η-dependent part discussed in Chapter 5.

Fig. 6.4 shows the same ratio of $0.5 < |\eta| < 1$ to $|\eta| < 0.5$ in the 0–5% most central bin. The points are our measurements and the error bars include statistical and remaining systematic uncertainties. The solid curve is the same ratio from PYTHIA calculation [Sj01] in 130 GeV $p + p$ collisions, and dotted, dashed, and dot-dashed

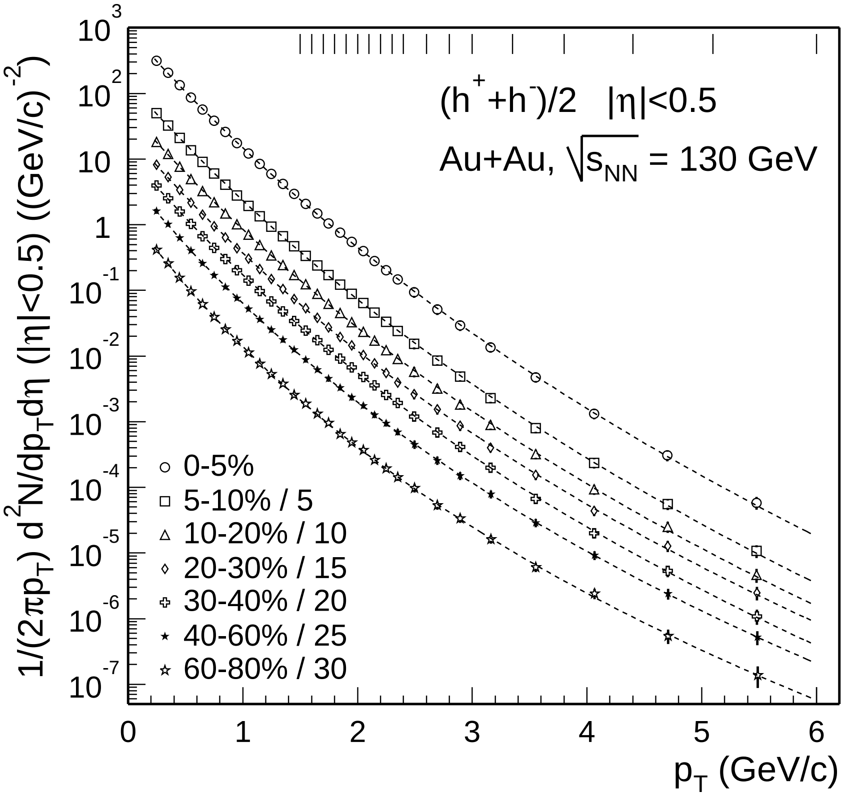

Figure 6.1: Inclusive p_T distributions of $(h^{+}+h^{-})/2$ within $|\eta| < 0.5$. Noncentral bins are scaled down by the indicated factors. The combined statistical and systematic errors are shown. Curves are fits to the power law function. Hash marks at the top indicate bin boundaries for $p_T > 1.5$ GeV/c.

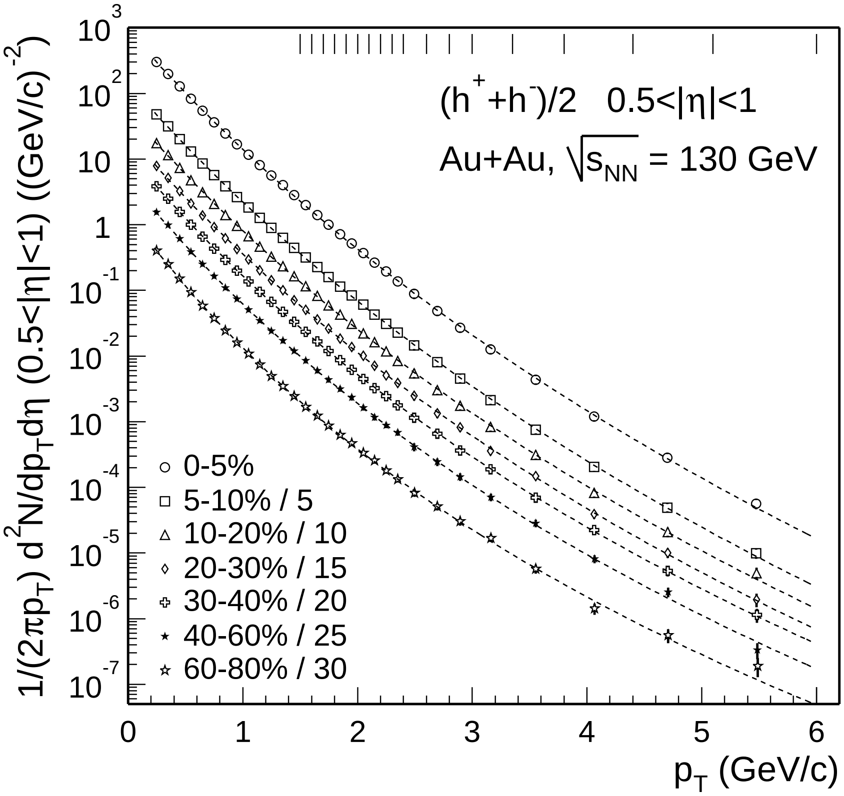

Figure 6.2: Inclusive p_T distributions of $(h^{+}+h^{-})/2$ within $0.5<|\eta|<1$. Noncentral bins are scaled down by the indicated factors. The combined statistical and systematic errors are shown. Curves are fits to the power law function. Hash marks at the top indicate bin boundaries for $p_T > 1.5$ GeV/c.

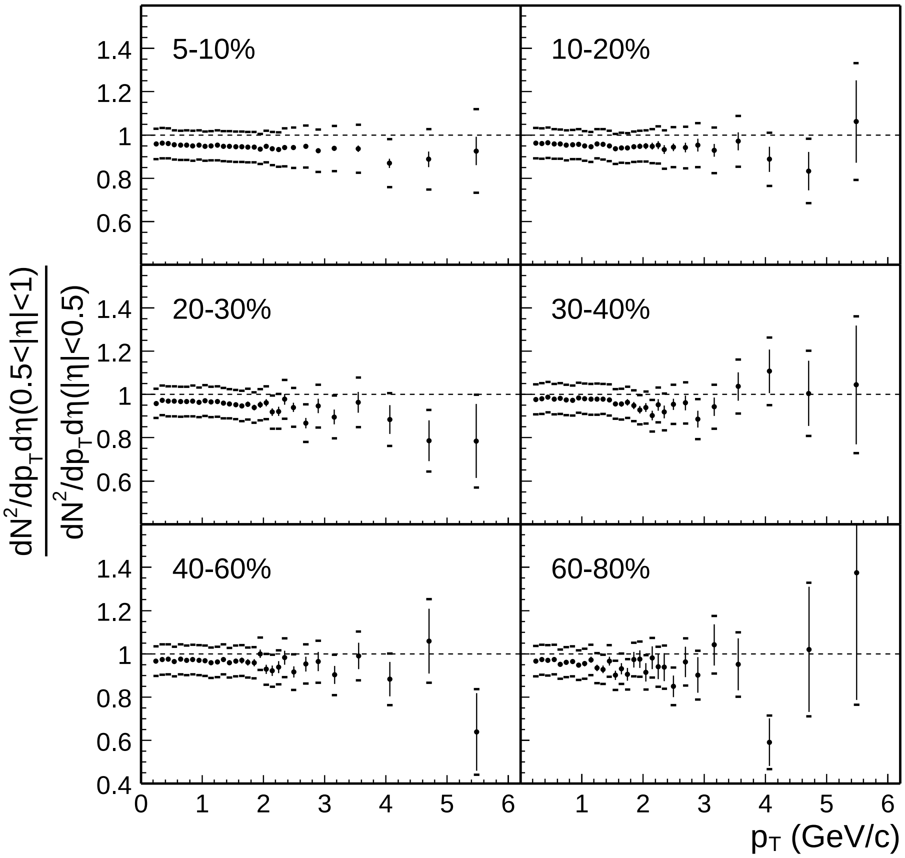

Figure 6.3: Ratios of p_T distributions within $0.5 < |\eta| < 1$ to those within $|\eta| < 0.5$ in various centrality bins. Error bars show statistical errors while caps are the quadrature sum of statistical errors and remaining systematic uncertainties.

curves are ratios from HIJING predictions of 130 GeV Au + Au collisions assuming the parton energy loss to be 0.5, 1.0, and 2.0 GeV/fm, respectively. No significant differences are observed in the comparisons of the inclusive charged hadron yields between the two η regions in Fig. 6.3 and Fig. 6.4 over a broad range of centrality for all measured p_T points. It suggests that an approximate boost invariant condition might be established in the early stage of collisions such that the suppression pattern of the particle yield has little η dependence in the measured region though the particle yield itself is sensitive to parton energy loss. Measurements with enhanced systematics should improve sensitivity to model calculations.

Since the difference between two η bins is small, we average two spectra weighted by statistical uncertainty to obtain the inclusive p_T distributions of $(h^+ + h^-)/2$ within $|\eta| < 1$ as shown in Fig. 6.5. The systematic uncertainty is also the weighted average. We obtained the pseudorapidity density (or multiplicity) $dN_{ch}/d\eta$ and mean p_T from fitting to the power law function for all p_T range and $|\eta| < 1$. The fit parameters C, $\langle p_T \rangle = 2p_0/(n-3)$, and n, together with $dN_{ch}/d\eta = 4\pi C p_0^2/(n-2)/(n-1)$, are listed in Table 6.1.

Table 6.1: Power law function fit parameters and $dN_{ch}/d\eta$ from inclusive charged hadron p_T spectra within $|\eta| < 1$ for various centrality bin and the *NN* reference.

Centrality	C ((GeV/c)^2)	$\langle p_T \rangle$ (GeV/c)	n	$dN_{ch}/d\eta$
0-5%	922 ± 60	0.506 ± 0.012	21.8 ± 1.3	637 ± 51
5-10%	729 ± 48	0.507 ± 0.012	21.0 ± 1.3	502 ± 40
10-20%	545 ± 36	0.506 ± 0.012	19.6 ± 1.1	369 ± 29
20-30%	369 ± 25	0.503 ± 0.012	18.7 ± 1.0	245 ± 20
30-40%	244 ± 16	0.497 ± 0.012	17.8 ± 0.9	156 ± 13
40-60%	130 ± 9	0.483 ± 0.012	16.2 ± 0.7	76.7 ± 6.1
60-80%	47 ± 4	0.451 ± 0.011	13.9 ± 0.6	23.1 ± 1.9
NN reference	6.6 ± 0.4	0.402 ± 0.003	13.0 ± 0.7	2.28 ± 0.11

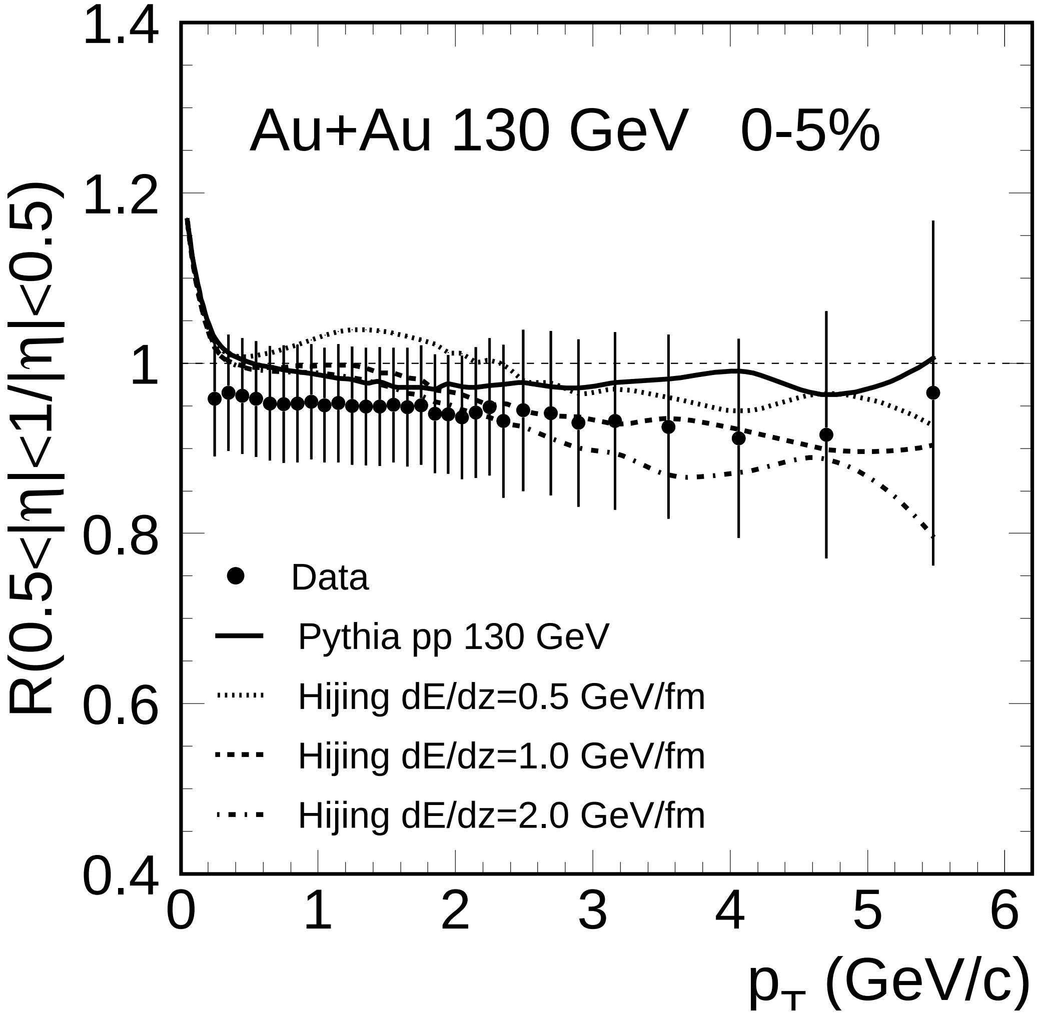

Figure 6.4: Ratio of p_T distributions within $0.5 < |\eta| < 1$ to that within $|\eta| < 0.5$ in the 0–5% most central bin. Points are measurements and error bars include statistical and remaining systematic uncertainties. Curves are described in the text.

In Fig. 6.6 we show the $dN_{ch}/d\eta$ normalized to per participant pair (upper panel) and mean transverse momentum $\langle p_T \rangle$ (lower panel) as functions of centrality represented by N_{part}. The solid points and error bars are data for Au + Au collisions and their combined statistical and systematic uncertainties while the caps in the upper panel are the qrudrature sum of systematic uncertainties of N_{part} and data. The open circles in two panels show the relevant observables from NN reference data. A slow increase of the hadron multiplicity per participant pair and mean transverse momentum is observed from $p+p$ collisions to Au + Au collisions, and from peripheral to central Au + Au collisions.

In the following chapter, we will use those average spectra within $|\eta| < 1$ (Fig. 6.5) to extract various variables such as sum p_T, truncated mean p_T, and hard fraction F in different cut off p_T^{cut} values.

6.2 Pseudorapidity Density Distribution

Fig. 6.7 shows $dN/d\eta$ distributions for $p_T > 2$ GeV/c and $-1 < \eta < 1$ in various centrality bins. The error bars show statistical uncertainties while the caps are the quadrature sum of statistical and systematic uncertainties. The systematic uncertainties are dominant and highly correlated. The $dN/d\eta$ distributions are scaled down by N_{coll} from HIJING and the same distribution of the NN reference. Due to nearly complete η-independence of the NN reference data for $p_T > 0.2$ GeV/c within $-1 < \eta < 1$ as shown in Fig. 3.5 and Fig. 6.4, constant $dN/d\eta$ of the NN reference are used in Fig. 6.7; and therefore the shapes of the $dN/d\eta$ distributions for the Au + Au collisions are preserved. The quadratic uncertainties on both N_{coll} and the NN reference data are shown in the shaded regions around the lines at unity which represent the binary collision scaling. Ratios below unity in the figure show that the high p_T hadrons over

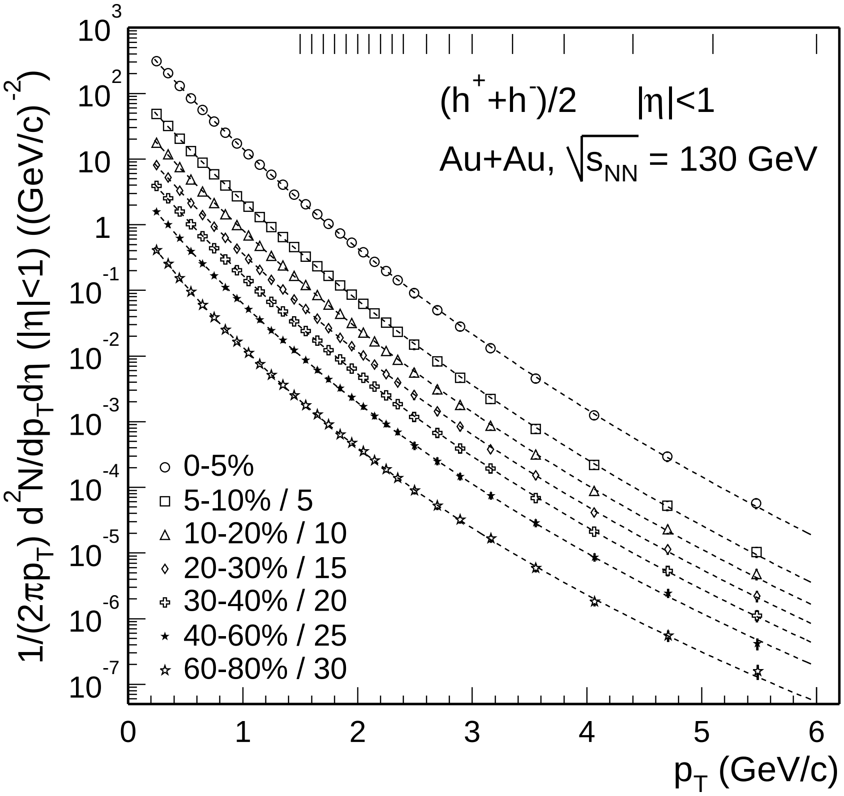

Figure 6.5: Inclusive p_T distributions of $(h^{+}+h^{-})/2$ within $|\eta|<1$. Noncentral bins are scaled down by the indicated factors. The combined statistical and systematic errors are shown. Curves are fits to the power law function. Hash marks at the top indicate bin boundaries for $p_T > 1.5$ GeV/c.

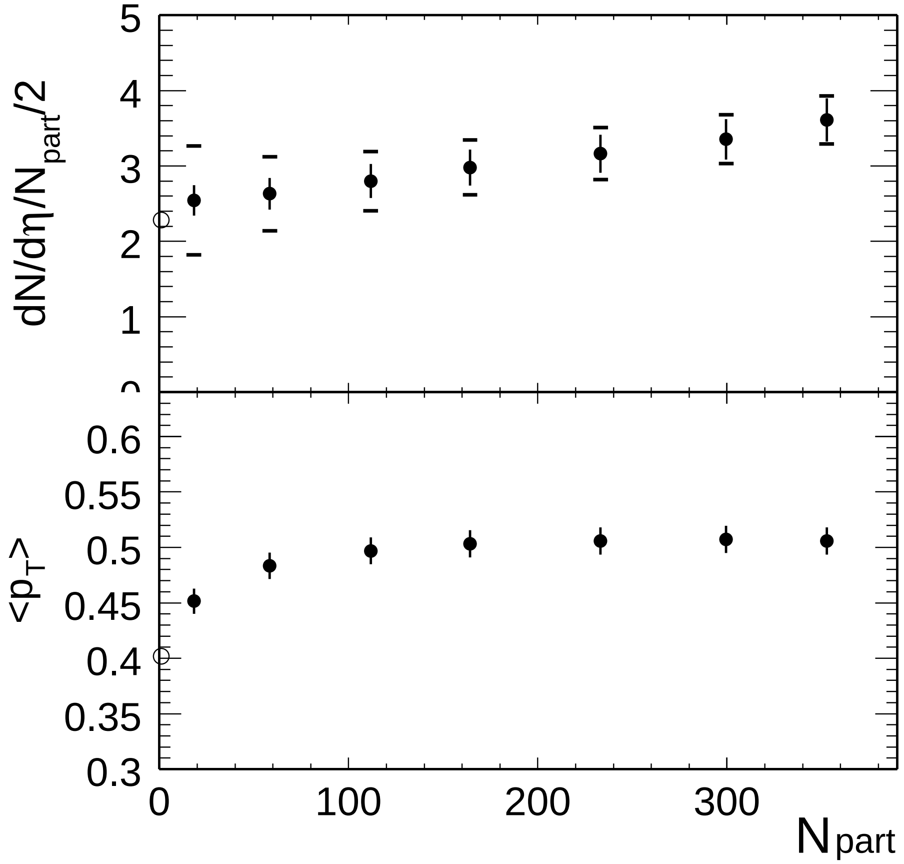

Figure 6.6: Charged hadron multiplicity per participant pair (upper panel) and mean transverse momentum (lower panel) as a function of N_{part} within $|\eta| < 1$. The combined statistical and systematic errors are shown. The solid points are for Au + Au collisions while the open circles are from NN reference data.

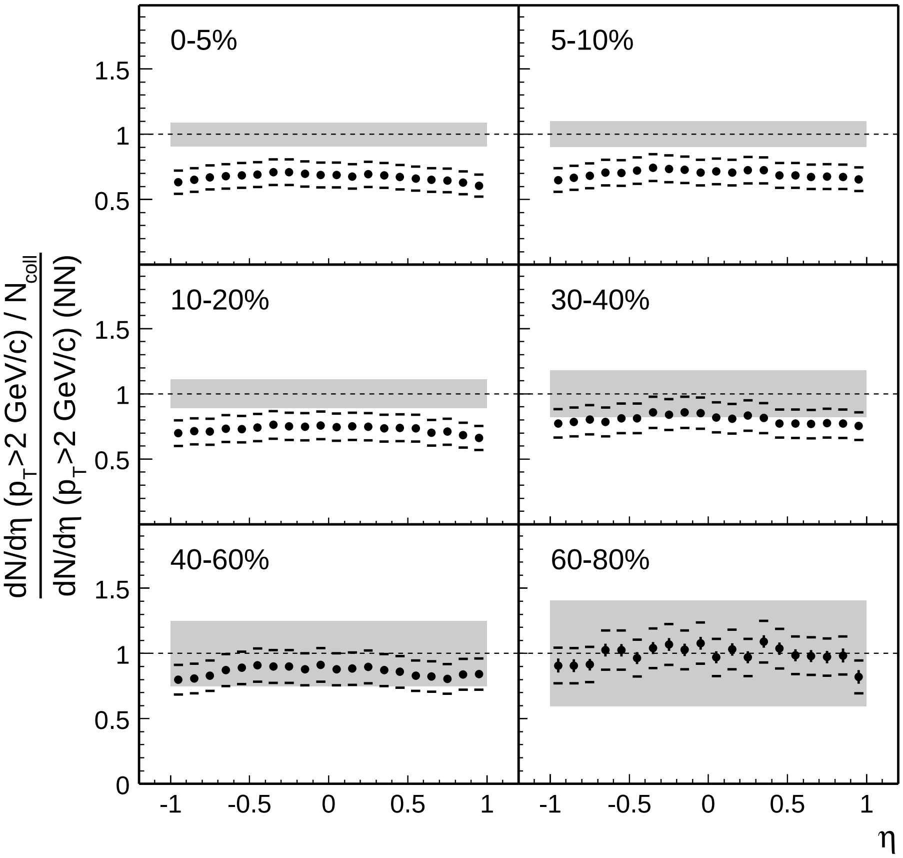

Figure 6.7: $dN/d\eta$ distributions for $p_T > 2$ GeV/c and within $-1 < \eta < 1$ scaled down by N_{coll} and NN reference.

2 GeV/c are suppressed with respect to those in $p+p$ collisions. The shape of $dN/d\eta$ for the high p_T hadrons is nearly flat, which indicates an approximately boost invariant region. No significant centrality dependence of the $dN/d\eta$ shapes within $-1 < \eta < 1$ is observed.

Fig. 6.8 shows ratios of the $dN/d\eta$ distributions for $p_T > p_T^{cut}$ in the selected $p_T^{cut} = 1$, 2, 3, 4 GeV/c with respect to that for $p_T > 0.5$ GeV/c within $-1 < \eta < 1$ in the 0–5% most central bin. The error bars show statistical uncertainties while the shaded regions show the quadrature sum of statistical and systematic uncertainties. Like those in Fig. 6.4, the dotted, dashed, and dot-dashed curves show the same ra-

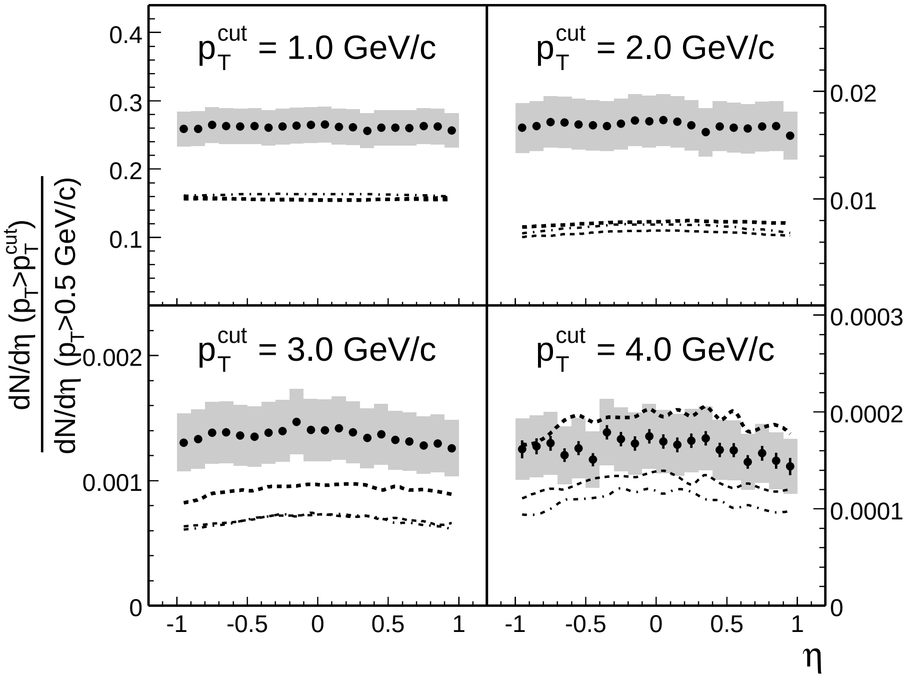

Figure 6.8: Ratios of $dN/d\eta$ distributions for $p_T > p_T^{cut}$ to that for $p_T > 0.5$ GeV/c within $-1 < \eta < 1$ in the 0–5% most central bin. The dotted, dashed, and dot-dashed curves are the HIJING calculations assuming parton energy loss to be 0.5, 1.0, and 2.0 GeV/fm, respectively.

tios from the HIJING predictions assuming parton energy loss to be 0.5, 1.0, and 2.0 GeV/fm, respectively. It appears that the shape of the $dN/d\eta$ distribution does not change significantly from intermediate to high p_T^{cut}, which is consistent qualitatively with the HIJING predictions and is a feature independent of the magnitude of the parton energy loss. The HIJING calculation seems to indicate that the measured ratio could be sensitive to the magnitude of the parton energy loss when p_T reaches 3 GeV/c or above. It suggests a way to probe hard parton scattering.

CHAPTER 7

Discussion

7.1 Nuclear Modification

The ratio of the binary collision scaled yields for the central over the peripheral collisions, R_{CP}, is defined as

$$R_{CP}(p_T) = \frac{(\frac{dN}{dp_T}/N_{coll})|_{central}}{(\frac{dN}{dp_T}/N_{coll})|_{peripheral}}. \tag{7.1}$$

In Fig. 7.1 and Fig. 7.2, we plot $R_{CP}(p_T)$ as ratios of the charged hadron yields per nucleon-nucleon collision within $|\eta| < 0.5$ and within $0.5 < |\eta| < 1$ for the central (0–5%) over the peripheral (40–60%, 60–80%) collisions in order to investigate the medium effects on hadron production at high p_T. The error bars are the uncertainties of the central data while the caps are the quadrature sum of the uncertainties of both central and peripheral data. The lines at unity and below show scaling with N_{coll} and N_{part} from HIJING, respectively, and the shaded regions show their systematic uncertainties from Fig. 3.9. The similar results are observed for those two pseudorapidity regions. Approximate participant scaling at low p_T is seen. The ratios rise monotonically below $p_T \sim 2$ GeV/c and decrease at high p_T, achieving a value of 0.2 ± 0.1 at $p_T = 5.5$ GeV/c. The results show that high p_T hadron production is considerably suppressed in more central collisions.

In Fig. 7.3 and Fig. 7.4, measurements of the nuclear modification factor, $R_{AA}(p_T)$,

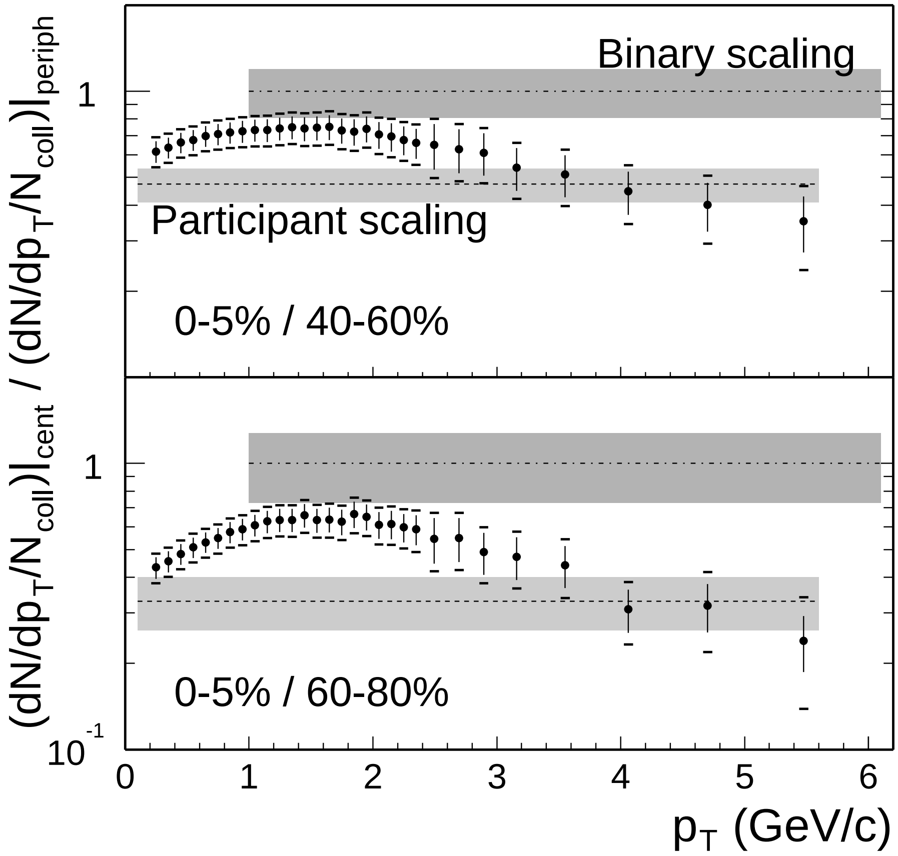

Figure 7.1: Ratio of charged hadron yields within $|\eta| < 0.5$ for central over peripheral collisions, normalized to N_{coll}. Error bars are uncertainties of central data while caps are the quadrature sum of uncertainties of both central and peripheral data. Lines at unity and below show scaling with N_{coll} and N_{part}, respectively, and shaded bands show their systematic uncertainties.

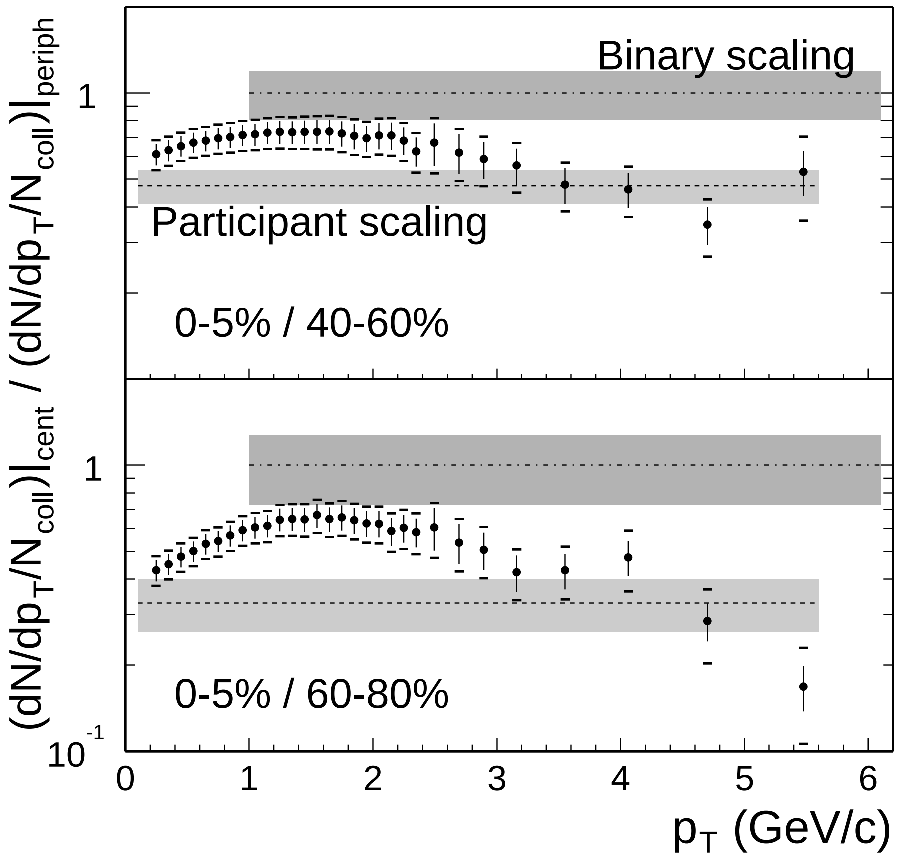

Figure 7.2: Ratio of charged hadron yields within $0.5 < |\eta| < 1$ for central over peripheral collisions, normalized to N_{coll}. Error bars are uncertainties of central data while caps are the quadrature sum of uncertainties of both central and peripheral data. Lines at unity and below show scaling with N_{coll} and N_{part}, respectively, and shaded bands show their systematic uncertainties.

as

$$R_{AA}(p_T) = \frac{\frac{d^2N_{AA}}{dp_T d\eta}/N_{coll}}{\frac{d^2\sigma_{NN}}{dp_T d\eta}/\sigma_{in}}, \tag{7.2}$$

are plotted for various centrality bins within $|\eta| < 0.5$ and within $0.5 < |\eta| < 1$. The error bars are the uncertainties of data while the caps are the quadrature sum of the uncertainties of both data and the NN reference spectrum. $R_{AA}(p_T)$ increases with p_T and reaches maxima at $p_T \simeq 2$ GeV/c. For peripheral collisions (60–80% and 40–60%), $R_{AA}(p_T)$ saturates around unity at $p_T > 2$ GeV/c, indicating approximate binary scaling. In contrast, for central collisions, $R_{AA}(p_T)$ demonstrates a suppression of high p_T hadron production with respect to nucleon-nucleon collisions. For the 0–5% most central bin, the strongest suppression of 0.3 ± 0.1 is observed at $p_T = 5.5$ GeV/c. The degree of the suppression increases with centrality. Similar results are observed for the two pseudorapidity regions, indicating that the suppression pattern is nearly the same and suggesting that the change rates of momenta in the transverse direction ($\delta p_T/p_T$) and in the longitudinal direction ($\delta p_z/p_z$) are approximately the same though the leading particles are emitted from different directions. The pseudorapidity regions $\eta < 0.5$ and $0.5 < \eta < 1$ correspond to the polar angle regions $90^\circ < \theta < 62^\circ$ and $62^\circ < \theta < 40^\circ$, respectively. Or, the two pseudorapidity regions $|\eta| < 0.5$ and $0.5 < |\eta| < 1$ correspond to the average emitting angles 90° and 50°.

7.2 Participant Scaling Behavior

The charged hadron yield per participant pair at $\sqrt{s_{NN}} = 130$ GeV shows a slow increase as a function of N_{part} as seen in Fig. 6.6, and this behavior has also been observed by PHENIX [Adc01] and PHOBOS [Bac02]. Such slow increase of hadron multiplicity as a function of centrality at RHIC has been considered by Kharzeev, Levin, and McLerran [KLM03] in the framework of initial state parton saturation.

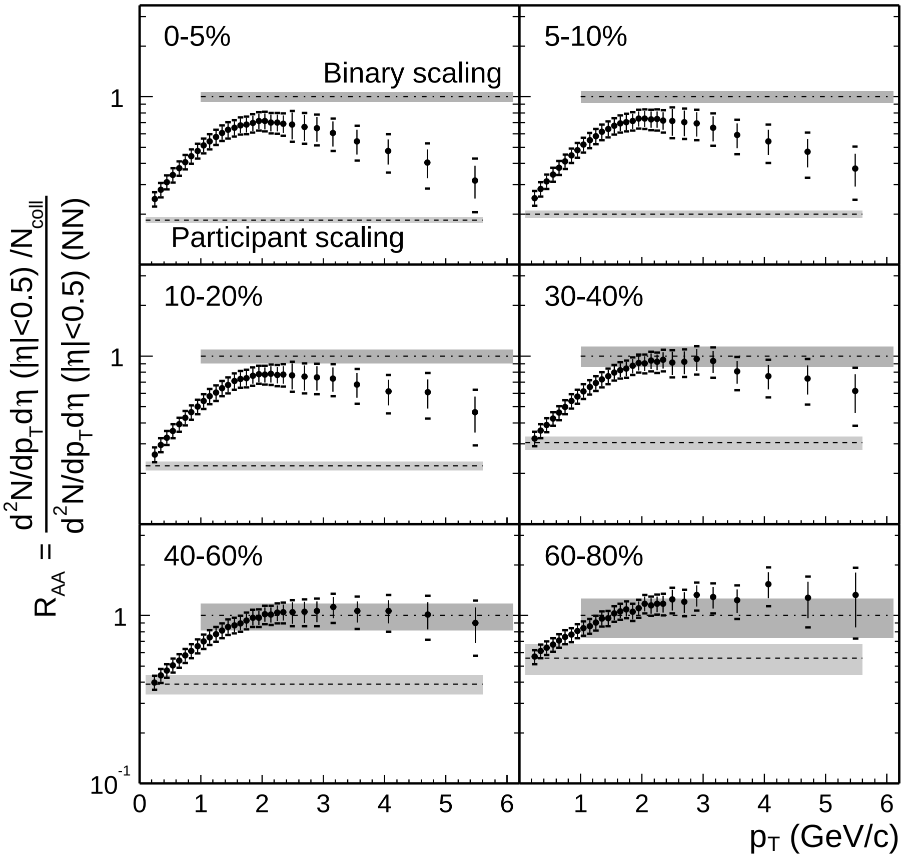

Figure 7.3: $R_{AA}(p_T)$ within $|\eta| < 0.5$ for various centrality bins, for Au + Au relative to *NN* reference spectrum. The error bars are the uncertainties of data while the caps are the quadrature sum of the uncertainties of both data and the *NN* reference spectrum. Lines at unity and below show binary and participant scaling, respectively, and shaded bands show their systematic uncertainties.

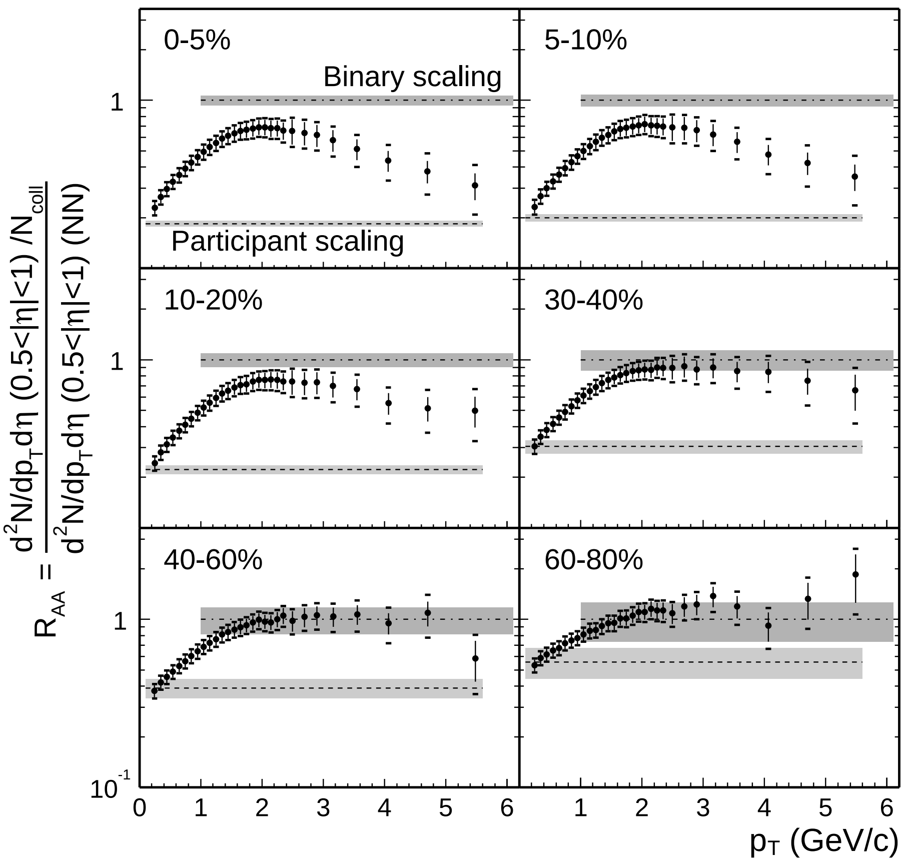

Figure 7.4: $R_{AA}(p_T)$ within $0.5 < |\eta| < 1$ for various centrality bins, for Au + Au relative to NN reference spectrum. The error bars are the uncertainties of data while the caps are the quadrature sum of the uncertainties of both data and the NN reference spectrum. Lines at unity and below show binary and participant scaling, respectively, and shaded bands show their systematic uncertainties.

They argue that the hadron multiplicity as a function of centrality would increase faster if produced jets lose energy radiating soft gluons that in turn fragment into hadrons at mid-rapidity. As a result of the parton saturation, it is predicted that hadron multiplicity should scale with N_{part} at a moderately high p_T (up to $p_T \sim 6 \div 8$ GeV/c at RHIC energies). An alternative explanation of the slow increase within the jet energy loss model is that the effective energy loss is significantly reduced in a thermal environment for less energetic partons due to detailed balance by thermal absorption [WW01b]. Therefore, the hadron multiplicity would not increase considerably as a result of the energy loss of high p_T partons since the cross section to produce the high p_T partons is very small at RHIC energies.

In Fig. 7.5, we plot charged hadron yield per participant pair within $|\eta| < 1$ normalized to that of nucleon-nucleon collisions as a function of N_{part} in various p_T bins. Similarly, we plot in Fig. 7.6 such a ratio for sum of particle transverse momenta in a region of $p_T > p_T^{cut}$. In both figures, the error bars are the uncertainties of data while the caps are the quadrature sum of the uncertainties of both data and N_{part}. The shaded regions around unity show systematic uncertainties of the NN reference data. These results show that the ratios increase with N_{part} in a region of $p_T(p_T^{cut}) < 3$ GeV/c, then flatten out for $p_T(p_T^{cut}) \simeq 4$ GeV/c, and may decrease with centrality at high enough p_T. Another feature of the ratios is that they are always above unity indicating that the yield in Au + Au is higher than the independent sum from participants in the measured p_T region.

Dependence of the charged hadron yield or the sum p_T on N_{part} in Fig. 7.5 or Fig. 7.6 is fitted with $B \cdot N_{part}^{\nu}$ by the curves shown in the figures. The scaling exponents, $\nu_{part}^{N}(p_T)$ or $\nu_{part}^{P}(p_T^{cut})$, are given in Fig. 7.7 as a function of p_T or p_T^{cut}. The error bars are the uncertainties of the fit parameters associated with the uncertainties of data. The lines and shaded regions are participant scaling exponents and errors of

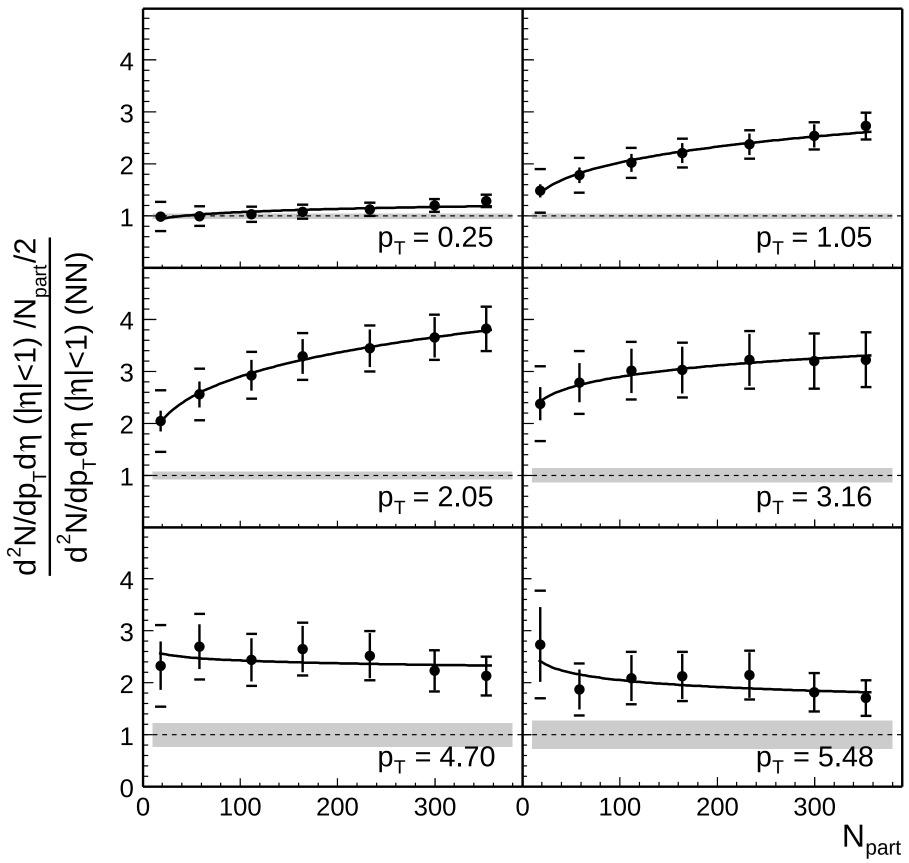

Figure 7.5: Ratio of charged hadron yields within $|\eta| < 1$ for Au + Au relative to NN reference spectrum scaled to $N_{part}/2$ as a function of centrality for selected p_T bins.

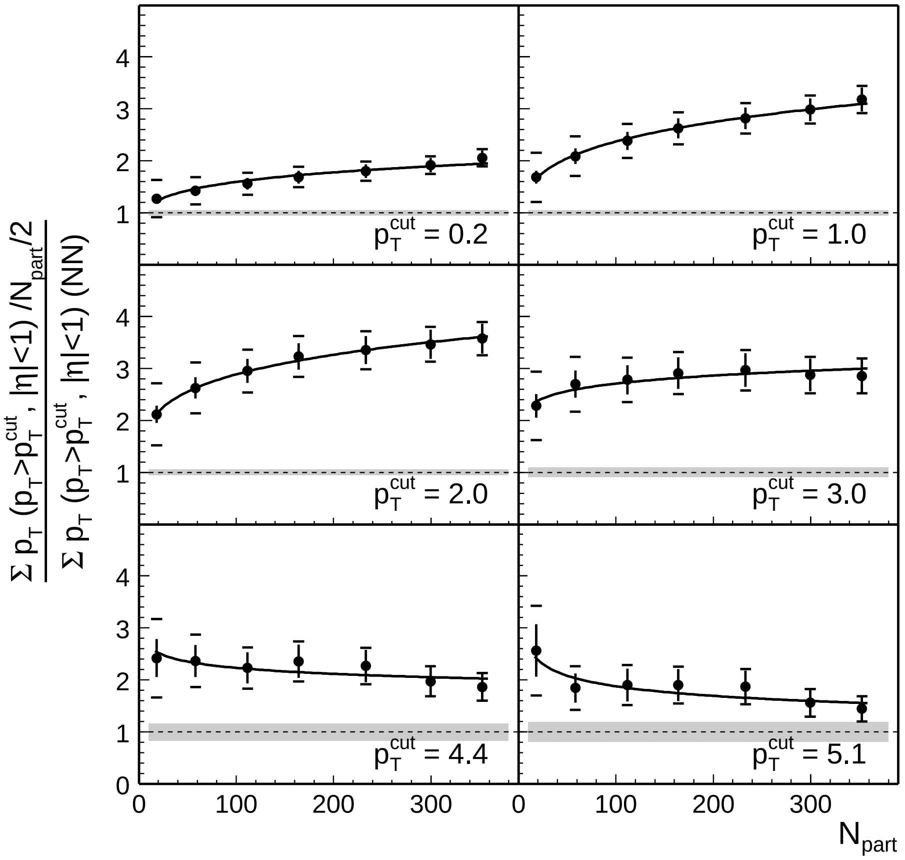

Figure 7.6: Ratio of sum p_T in $p_T > p_T^{cut}$ within $|\eta| < 1$ for selected p_T^{cut} similar to the yield ratio in Fig. 7.5.

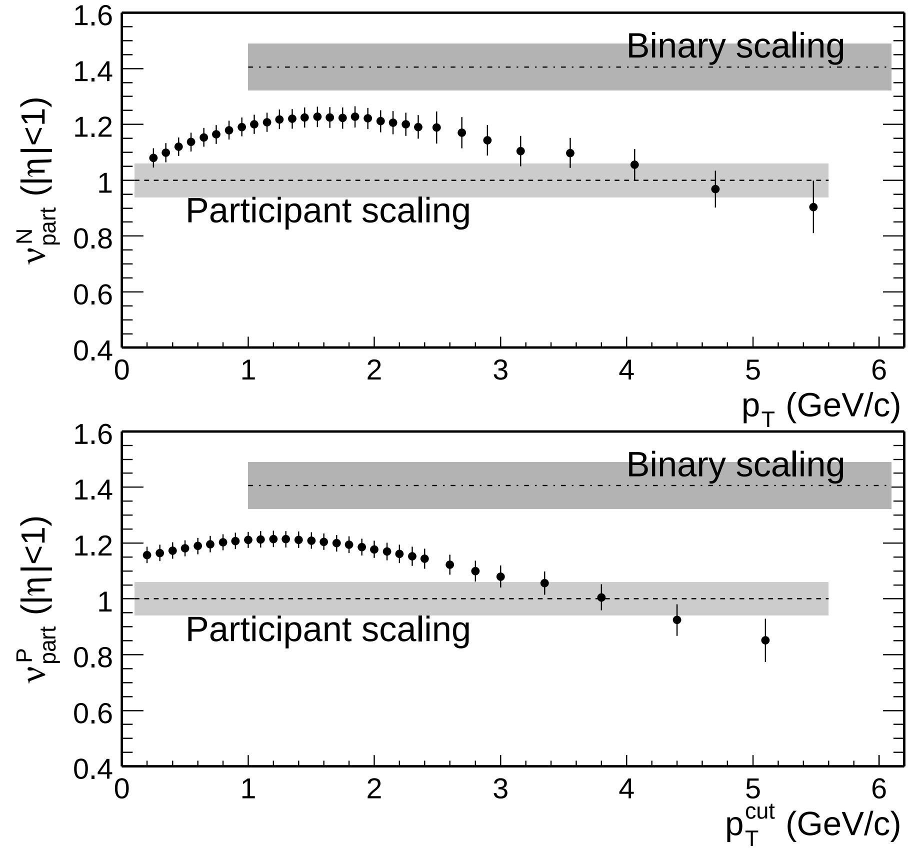

Figure 7.7: Participant scaling exponents of charged hadron yields (upper panel) or sum p_T (lower panel) over a broad centrality range as a function of p_T or p_T^{cut} within $|\eta| < 1$.

N_{coll} or N_{part}. As shown in Fig. 7.7, the approximate participant scaling ($\nu_{part} \simeq 1$) at $p_T(p_T^{cut}) \simeq 4$ GeV/c could be accidental, and a falling trend for ν_{part} is observed for $p_T(p_T^{cut}) > 2$ GeV/c.

In Fig. 7.8, we plot ratios of truncated mean p_T within $|\eta| < 1$ in Au + Au collisions to that in $p+p$ collisions as a function of centrality for various p_T^{cut}. The truncated mean p_T is defined as follows:

$$\langle p_T(p_T^{cut}) \rangle = \frac{\int_{p_T^{cut}}^{\infty} p_T \cdot dN/dp_T \cdot dp_T}{\int_{p_T^{cut}}^{\infty} dN/dp_T \cdot dp_T} - p_T^{cut}. \tag{7.3}$$

The error bars combine statistical errors and systematic uncertainties of data with the

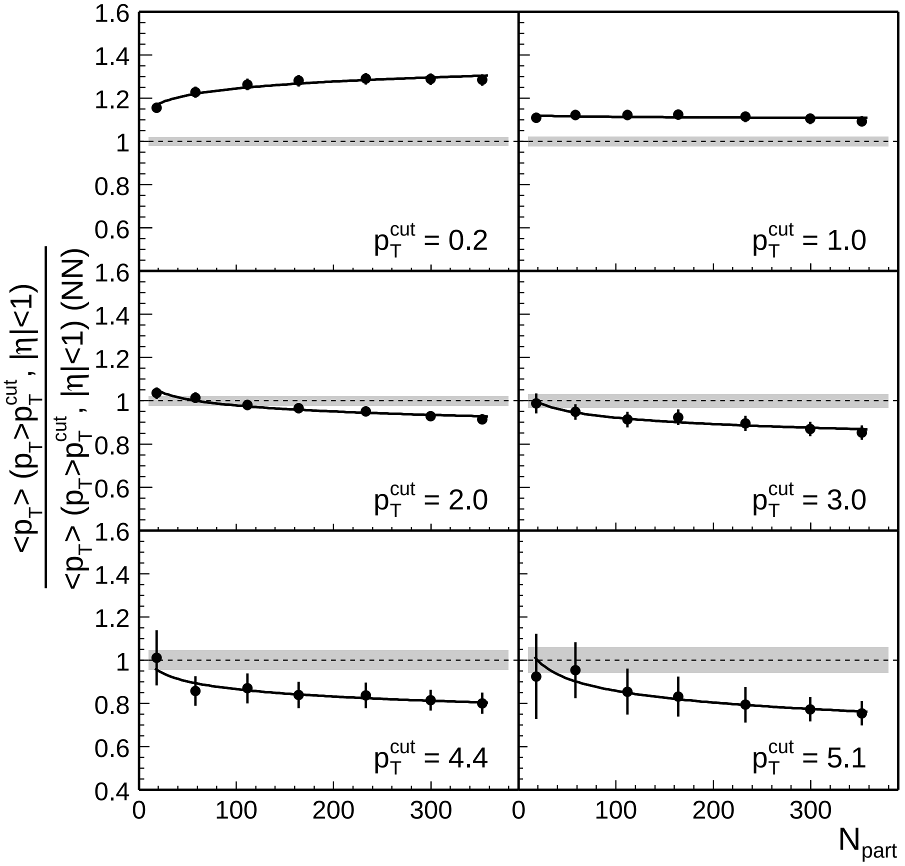

Figure 7.8: Ratio of truncated mean p_T in $p_T > p_T^{cut}$ within $|\eta| < 1$ for Au + Au relative to that of NN reference as a function of centrality for selected p_T^{cut}.

latter determined mainly by p_T uncertainties. The shaded regions around unity show the systematic uncertainties of the truncated mean p_T for the NN reference. The ratio is larger than 1.0 for $p_T^{cut} \leq 1$ GeV/c. For $p_T^{cut} = 0.2$ GeV/c, the ratio increases with N_{part} and turns flat for $p_T^{cut} = 1$ GeV/c. However, for $p_T^{cut} \geq 2$ GeV/c, the ratio becomes smaller than 1.0 for $N_{part} > 100$ and decreases with N_{part}. This behavior was also observed by PHENIX [Adc03], but our data extend to higher p_T^{cut}.

In Fig. 7.9 the truncated mean p_T ratios are plotted as a function of p_T^{cut} for the 0–5% most central bin and the 60–80% peripheral bin. The error bars are combined statistical and systematic uncertainties of data while the caps are the quadrature sum of the uncertainties of both the Au + Au data and the NN reference data. We see that the dependence of the ratio on p_T^{cut} behaves quite differently in central and peripheral collisions in the measured p_T region. The truncated mean p_T in peripheral Au + Au collisions is higher than that in $p+p$ collisions for $p_T^{cut} < 2.0$ GeV/c and then approaches the truncated mean p_T of $p+p$ collisions for higher p_T^{cut}. For the 0–5% most central collisions, the truncated mean p_T is higher than that in $p+p$ collisions for $p_T^{cut} < 1.2$ GeV/c, then becomes lower than the truncated mean p_T of $p+p$ collisions for higher p_T^{cut} and the ratio seems to flatten out for $p_T^{cut} > 2.5$ GeV/c, similar to that in peripheral collisions. In addition, the ratio is higher for central collisions than for peripheral collisions for $p_T^{cut} < 1$ GeV/c and the trend reverses for high p_T^{cut}, consistent with stronger nuclear effects in central Au + Au collisions. Quantitatively, for the 0–5% most central bin the truncated mean p_T increases $\sim$ 30% at $p_T^{cut} = 0.2$ GeV/c and decreases $\sim$ 20% at $p_T^{cut} \simeq 4$ GeV/c with respect to that of the NN reference.

7.3 Hard Fraction from Two-Component Model

In the two-component model, the hadron multiplicity contains the sum of yields from the soft and hard processes, that is assumed to scale with N_{part} and N_{coll}, respectively, which can be expressed in Eq. 2.1. Similiarly, for high p_T hadron multiplicity, we express it as

$$\begin{aligned} dN/d\eta(p_T^{cut}) &= (1-x(p_T^{cut}))n_{pp}(p_T^{cut})N_{part}/2 \\ &\quad +x(p_T^{cut})n_{pp}(p_T^{cut})N_{coll}, \end{aligned} \tag{7.4}$$

where $n_{pp}(p_T^{cut})$ and $x(p_T^{cut})$ are the hadron multiplicity and the fraction of hard processes in $p+p$ collisions, respectively. The p_T^{cut}-dependent fraction of hard processes

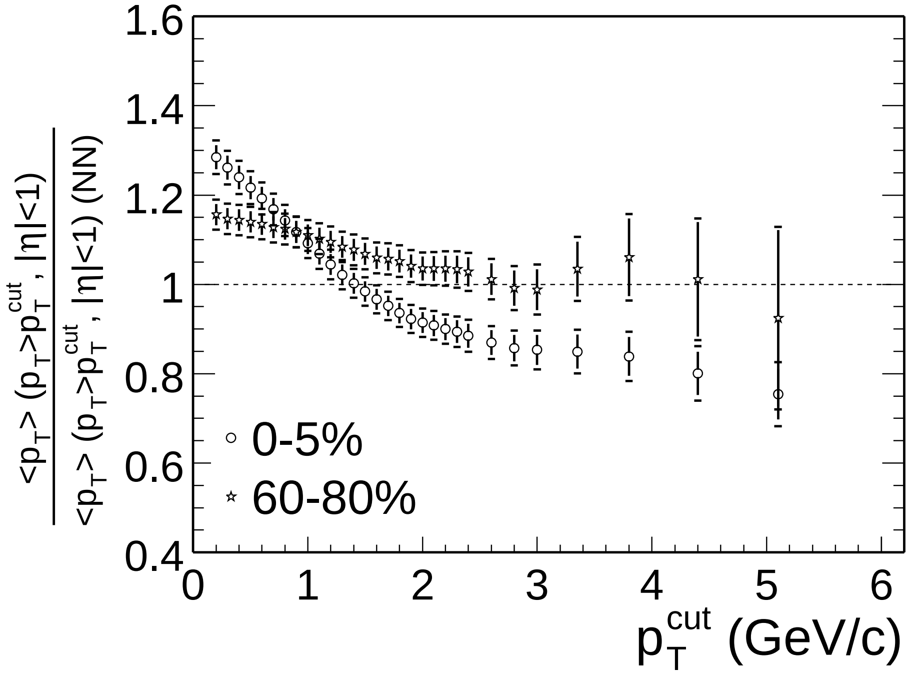

Figure 7.9: Ratio of truncated mean p_T in $p_T > p_T^{cut}$ within $|\eta| < 1$ as a function of p_T^{cut} for central and peripheral collisions.

in AA collisions is thus defined by

$$F(p_T^{cut}) = \frac{x(p_T^{cut})n_{pp}(p_T^{cut})N_{coll}}{dN/d\eta(p_T^{cut})}. \tag{7.5}$$

The phenomenological expression, Eq. 7.5, allows one to examine the fraction of hard processes empirically through a running p_T scale, providing a way to quantitize the p_T dependence of hadron suppression at moderate p_T in Au + Au collisions and the transition between the soft and hard processes. The hard fraction that is extracted in this way may not necessarily correspond to the fraction of parton-parton scatterings at a certain p_T in early Au + Au collisions since a high p_T parton stemming from a hard parton-parton scattering may lose energy in the medium and becomes soft.

In Fig. 7.10, we plot F obtained within $|\eta| < 1$ as a function of p_T^{cut} for different centrality bins. The error bars are the uncertainties from the data only while the caps

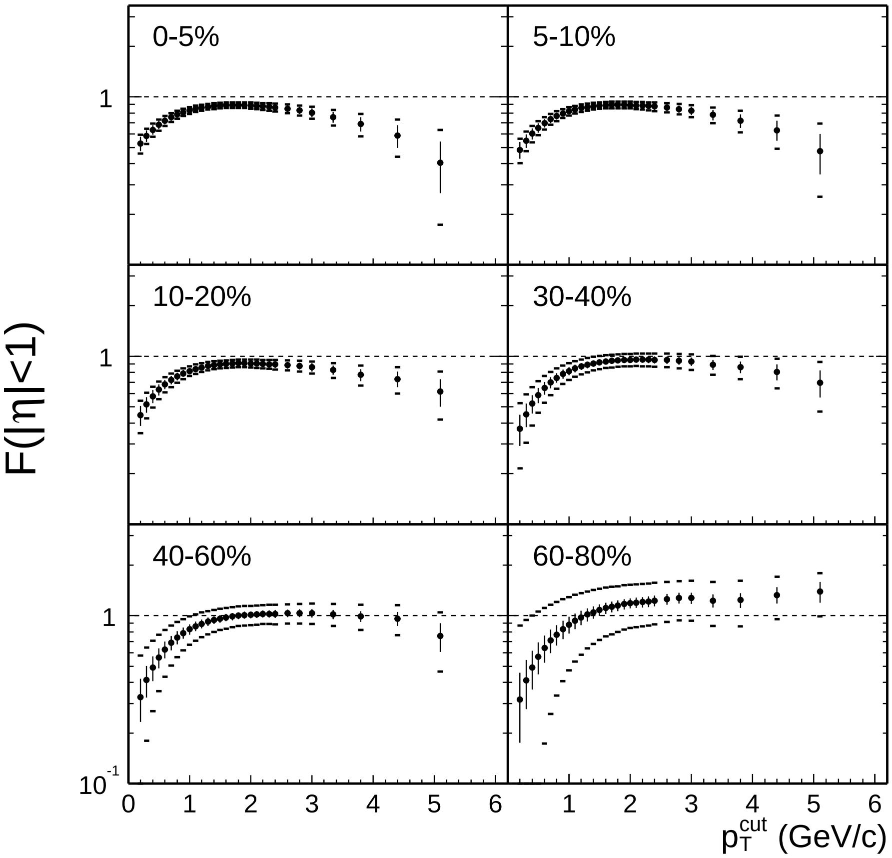

Figure 7.10: Fraction F within $|\eta| < 1$ for various centrality bins.

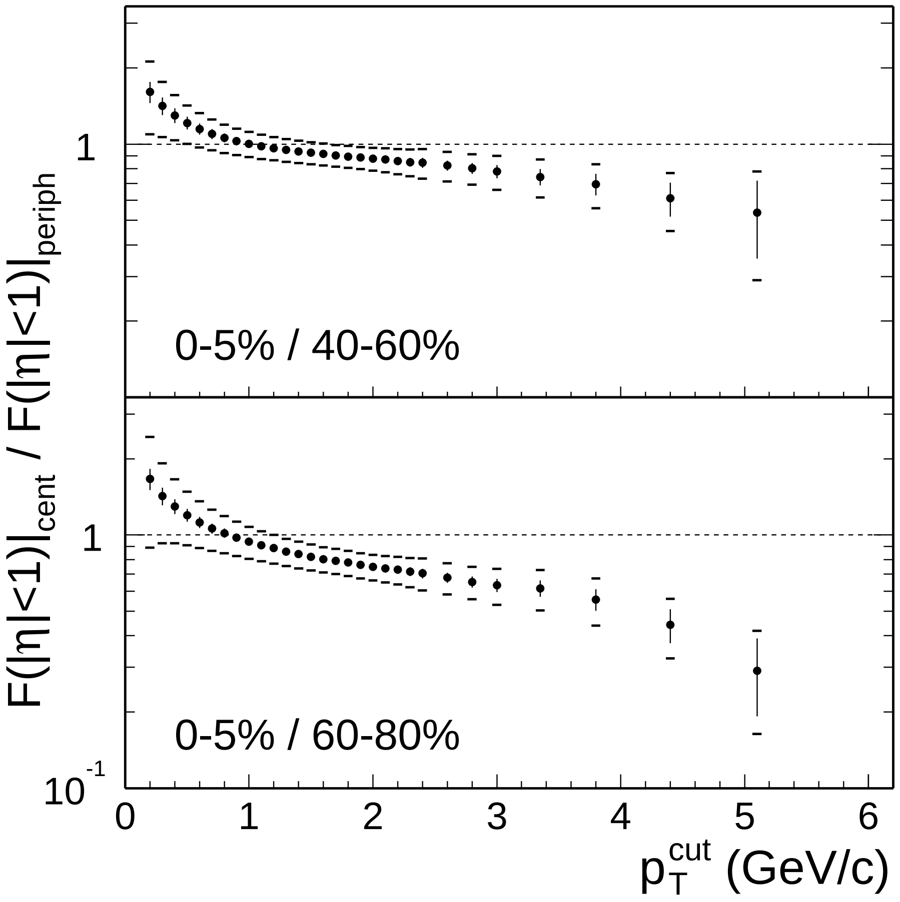

Figure 7.11: Ratio of fraction F within $|\eta| < 1$ for central over peripheral collisions.

are the total uncertainties resulting from the data, N_{part} and N_{coll}/N_{part}, and the NN reference. For the two most peripheral bins, F increases with p_T^{cut} and saturates around unity at $p_T^{cut} \simeq 2$ GeV/c. For the 60–80% bin, F may be even larger than 1, which implies that nuclear effects make hadron production at high p_T increased faster than the binary scaling. One of these nuclear effects is the Cronin effect. For more central collisions, F decreases at $p_T^{cut} > 2$ GeV/c. For the most central collisions, the fraction of hard processes drops to only about 40% at $p_T^{cut} \simeq 5$ GeV/c, demonstrating a strong high p_T suppression in central Au + Au collisions. The high p_T suppression in central collisions with respect to peripheral collisions can be more clearly seen from the ratio of F in two centrality bins in Fig. 7.11. The error bars are the uncertainties of central data while the caps are the quadrature sum of the uncertainties of both central and peripheral data. The ratio monotonically decreases as a function of p_T^{cut} from about 1.0 at $p_T^{cut} < 1$ GeV/c. Dependence of F on N_{part} for various p_T^{cut} is plotted in Fig. 7.12 where the curves are the fits of $B \cdot N_{part}^{\nu}$ to the data. It shows that for $p_T^{cut} > 2$ GeV/c the fraction of hard processes decreases with centrality and it is about 80% at $p_T^{cut} = 1$ GeV/c, independent of centrality.

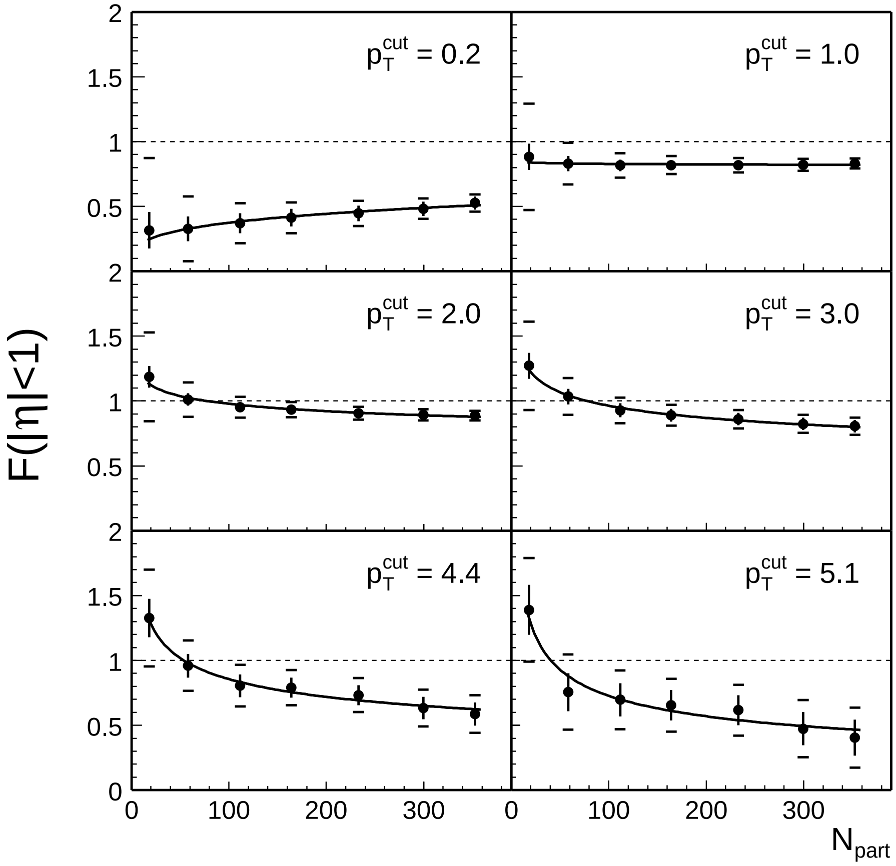

Figure 7.12: Fraction F in $p_T > p_T^{cut}$ within $|\eta| < 1$ as a function of centrality for selected p_T^{cut}. For $p_T^{cut} > 2$ GeV/c, F decreases with centrality and is about 80% at $p_T^{cut} = 1$ GeV/c, independent of centrality.

CHAPTER 8

Conclusion

8.1 Summary

we have provided a detailed description on data analysis techniques, especially on the p_T smearing correction and the background subtraction, giving the total systematic uncertainties of the measured spectra within $|\eta| < 0.5$ ($0.5 < |\eta| < 1$) at the highest bin $p_T = 5.5$ GeV/c $\approx 24\%$ ($\approx 18\%$) for central events and $\approx 17\%$ ($\approx 15\%$) for peripheral events. The detailed study shows that there is a non-negligible effect on the η acceptance correction when the NN reference spectrum extrapolated from the UA1 data is used. The multipicative correction of 1.35 ± 0.09 (1.33 ± 0.09) at $p_T = 5.5$ GeV/c is obtained for $|\eta| < 0.5$ ($0.5 < |\eta| < 1$). Several dynamic models and the Glauber model are used to compute N_{coll} and N_{part}, showing that the model dependent uncertainties of N_{coll} and of N_{part} range between 20% and between 10% for all centrality bins.

We present inclusive p_T distributions of $(h^+ + h^-)/2$ within $|\eta| < 0.5$ and $0.5 < |\eta| < 1$ in Au + Au collisions at $\sqrt{s_{NN}} = 130$ GeV. No significant difference is found in these two η regions for the covered p_T and centrality range. The pseudorapidity density distribution within $-1 < \eta < 1$ for high p_T hadrons is nearly flat for all centrality bins. These results suggest that an approximate boost invariant condition might be established in the early stage of collisions.

For central collisions, the measurement of nuclear modification factor $R_{AA}(p_T)$

demonstrates a suppression of high p_T hadron production with respect to nucleon-nucleon collisions while for peripheral collisions, $R_{AA}(p_T)$ saturates around unity at $p_T > 2$ GeV/c, indicating an approximate binary scaling. For the 0–5% most central bin, the strongest suppression of 0.3 ± 0.1 is observed at $p_T = 5.5$ GeV/c. The suppression increases as the collisions become more central.

The results of the charged hadron yield (the sum p_T) for various centrality bins as a function of p_T (p_T^{cut}) indicate an approximate participant scaling at about 4 GeV/c could be accidental and is not observed over any extended p_T range. The truncated mean p_T is observed to have a different participant dependence: it increases with centrality when $p_T^{cut} < 1$ GeV/c while it decreases with centrality when $p_T^{cut} > 1$ GeV/c. For the peripheral collisions, the increase of the truncated mean p_T with respect to that in $p+p$ collisions is observed for $p_T^{cut} < 2$ GeV/c. For the 0–5% most central bin, the truncated mean p_T increases $\sim$ 30% at $p_T^{cut} = 0.2$ GeV/c and decreases $\sim$ 20% at $p_T^{cut} \simeq 4$ GeV/c with respect to that of the NN reference.

The fraction of hard processes in the two-component model is extracted and plotted as a function of p_T^{cut} or centrality. For more central collisions, the fraction decreases when $p_T^{cut} > 2$ GeV/c, and drops to only about 40% at $p_T^{cut} \simeq 5$ GeV/c with respect to the binary scaling for the 0–5% most central bin, demonstrating a strong suppression of hard process components. The ratio of the fractions for central over peripheral collisions monotonically decreases as a function of p_T^{cut} and crosses 1.0 at $p_T^{cut} \simeq 1$ GeV/c, where the fraction is about 80% and is independent of centrality.

Existing theoretical calculations have not yet reproduced all experimental features in this moderate p_T region. Our measurements provide constraints to the collision dynamics in both longitudinal and transverse directions.

8.2 Recent Results

The observed high p_T hadron suppression phenomenon is consistent with a large energy loss in the final state (for various models, please refer to Section 5 of Chapter 2), suggesting that high density matter have been formed in the central Au + Au collisions at RHIC.

However, there exist other theoretical scenarios besides the pQCD final state parton energy loss mechanism to explain the observed high p_T hadron suppression. The KLM saturation model [KLM03] considers such a hadron suppression in the moderate p_T range is a consequence of initial state parton saturation in the color glass condensate. They predict that at a moderately high p_T, the hadron multiplicity should scale with N_{part} for Au + Au collisions and with $N_{part}^{1/2}$ for $p(d)+Au$ collisions, and therefore is much reduced in central Au + Au collisions comparing to the binary scaling ($N_{part}/N_{coll} \approx 0.37$). Another feature predicted by the parton saturation model is the p_T-independent R_{AA} in both Au + Au and $p(d)+Au$ collisions. On the other hand, another saturation model [BKW03] demonstrates that the perturbative saturation leads to Cronin-type transverse momentum broadening of the produced gluon spectrum in both nucleus-nucleus and proton(deuteron)-nucleus collisions. Although the centrality dependence of the produced gluon spectrum shows N_{part} scaling in some limiting case, it differs significantly from a simple N_{part} or N_{coll} scaling in the experimentally accessible regime. While this BKW saturation model can predict a Cronin-type enhancement in $d+Au$ collisions, it fails to explain the significant suppression of high p_T hadron spectrum observed in the Au + Au collisions at RHIC.

Which effect (the initial state parton saturation or the final state energy loss) is dominant in the central Au + Au collisions can be differentiated by studying the $d+Au$ collisions at RHIC. In general, it is believed that any final state effect should be absent in the $d + Au$ collisions, and thereby the manifested nuclear effects are expected to be the Cronin enhancement, and/or nuclear shadowing and antishadowing. On the other hand, the parton saturation model [KLM03] predicts a p_T-independent nuclear modification factor below unity (binary scaling) for the $d + Au$ collisions.

Recent STAR results on inclusive charged hadron production for p_T up to 10 GeV/c in Au + Au and $p + p$ collisions [Ada03a], and $d + Au$ [Ada03b] collisions at $\sqrt{s_{NN}} =$ 200 GeV are shown in Fig. 8.1. Fig. 8.1 shows $R_{AB}(p_T)$ for minimum bias and central $d + Au$ collisions, and also central Au + Au collisions. $R_{AB}(p_T) > 1$ for $2 < p_T < 7$ GeV/c in the $d + Au$ collisions, consistent with the Cronin-type enhancement picture, while the large suppression in high p_T hadron production is clearly seen in the central Au + Au collisions. Another feature seen in Fig 8.1 is an approximately constant $R_{AA}(p_T)$ of charged hadrons for $5 < p_T < 10$ GeV/c in central Au + Au collisions, indicating the favorable energy loss picture of the linear energy dependence (or Bethe-Heitler case) other than constant or energy square-root dependent energy loss (please refer to Section 2.5.3).

Different models predict that the Cronin enhancement for 200 GeV $p(d) + Au$ collisions should peak at $p_T \approx 2.7 - 4.4$ GeV/c with the peak values of $R_{AB} \approx 1.1 - 1.5$ [Acc02]. For detailed information about these pQCD models, please see Accardi's review [Acc02] and references therein. The enhancement is expected to be larger for central $p(d) + Au$ collisions. On the other hand, the saturation model calculation in [KLM03] predicts $R_{AB}(p_T) < 1$, with larger suppression for more central $p(d) + Au$ collisions, achieving $R_{AB}(p_T) \approx 0.75$ for the 20% most central $d + Au$ collisions. The STAR measurements suggest that the Cronin effect plays a significant role in $d + Au$ collisions exhibiting $R_{AB}(p_T) > 1$ for $2 < p_T < 7$ GeV/c. The $d + Au$ measurement rules out the initial parton saturation as an explanation of the observed high p_T suppression in central Au + Au collisions. This suppression results from the final state

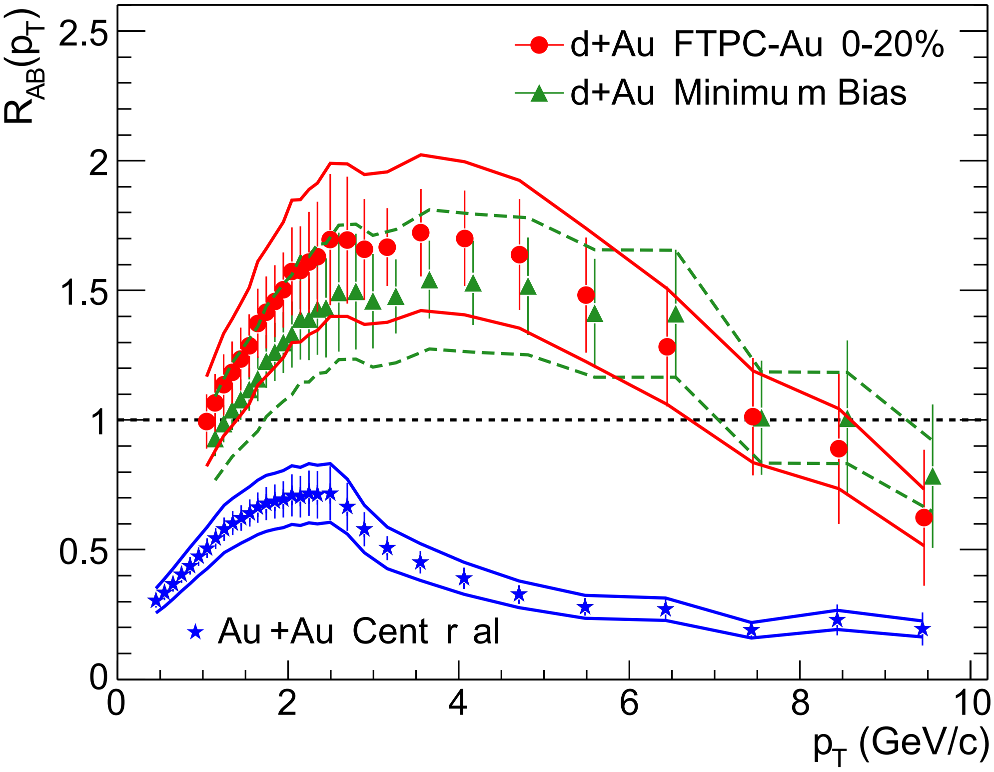

Figure 8.1: p_T dependence of the R_{AB} in minimum bias and central d+Au collisions, and central Au+Au collisions at $\sqrt{s_{NN}} = 200$ GeV from STAR measurements. The minimum bias d+Au data are displaced 100 MeV/c to the right for clarity.

interaction of high p_T particles from hard scattering processes.

8.3 Perspective

Another scenario which would explain the high p_T suppression in the central Au + Au collisions at RHIC is the GGX model [GGX03]. There it is argued that for leading hadrons with moderately high $p_T \leq 10$ GeV/c, originally pointlike jet partons should, to a large fraction, materialize into hadrons while still inside the expanding fireball. These (pre)hadrons will interact (by collisions) with the bulk hadronic matter making up the fireball. The late hadronic final state interactions with the bulk of comovers have a clear and nonvanishing effect in suppressing the spectrum. On average, one to two such interactions should already be enough to explain quantitatively the RHIC results.

While it is established that the final state effect is responsible for the high p_T hadron suppression in the high energy central Au + Au collisions, it has not been unambiguously determined whether such a final state effect is the interaction in partonic matter or in hadronic matter. The disentanglement of the final state partonic energy loss from the final state hadronic energy loss could be very challenging and delicate. One possible way could be precise measurements of p_T distributions for charmed particles like the D mesons. It is believed that heavy quarks should lose considerably less energy than light quarks and gluons. Hence, if the D mesons should not show any significant p_T suppression in the moderate p_T range, this would then favor the partonic pQCD jet quenching scenario.

Another important measurment to reveal particle production mechanisms in matter at the extreme temperature and density created in nuclear collisions at RHIC is the particle-type dependence of the nuclear modifications. STAR is capable of reconstructing weak decay particles using decay topology techniques for p_T up to 6 GeV/c in Au + Au collisions at $\sqrt{s_{NN}} = 200$ GeV. For example, the meson K^0_S and baryon Λ can be reconstructed from decay channel $K^0_S \to \pi^+ + \pi^-$ and $\Lambda \to p + \pi^-$. A new STAR measurement [Ada03c] indicates that the kaon and lambda yields are suppressed by different magnitudes and the p_T scales associated with the onset of the high p_T suppression are different. As shown in Fig. 8.2, for most of the intermediate p_T region, the ratio of $\Lambda + \overline{\Lambda}$ yields per nucleon-nucleon collision for central over peripheral collisions coincides with binary collision scaling, while such a ratio for kaons is significantly below unity. At $p_T \approx 5$ GeV/c, the ratios for K^0_S and $\Lambda + \overline{\Lambda}$ are approaching the ratio for the charged hadron. Such a p_T scale, associated with the approximately constant $R_{AA}(p_T)$ for charged hadron at $p_T > 5$ GeV/c in central Au + Au collisions seen in Fig 8.1, may indicate that single parton fragmentation is dominant for high p_T production above this p_T scale.

The absence of a significant suppression with respect to the binary scaling of the $\Lambda + \overline{\Lambda}$ yield at intermediate p_T in central Au + Au collisions may indicate the presence of dynamics beyond parton energy loss and standard fragmentation. A parton recombination scenario [FMN03] can expect such a stronger dependence on parton density for baryon production than for meson production. The particle-type and p_T dependence of the nuclear modification factors, particularly at intermediate p_T, may provide a unique means to investigate the hadronization of the bulk dense matter formed in nucleus-nucleus collisions at RHIC.

8.4 Conclusion

In conclusion, I would quote what Thomas Kirk, Brookhaven's Associate Laboratory Director for High Energy and Nuclear Physics, and Timothy Hallman, Spokesper-

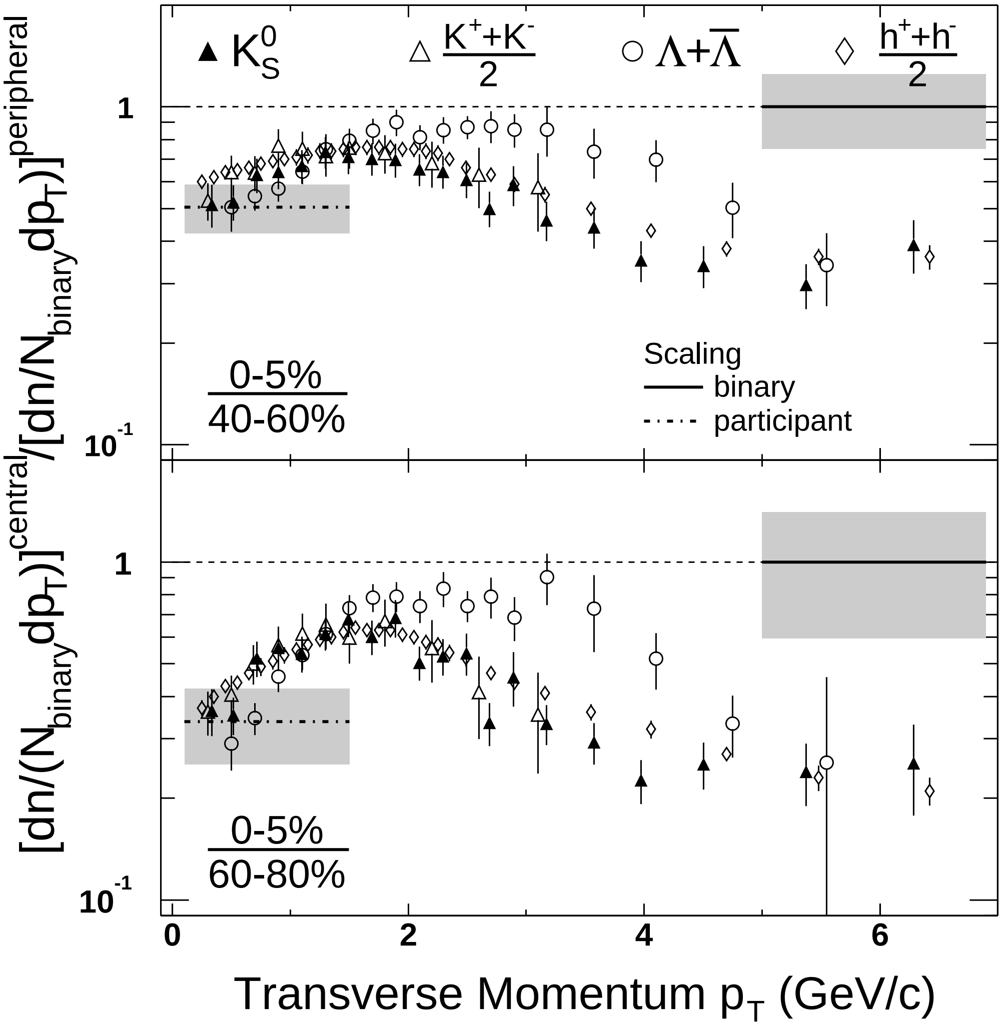

Figure 8.2: Ratio of identified particle yields within $|y| < 1$ for central over peripheral collisions, normalized to N_{coll}. The ratio for charged hadron is also shown.

son of the STAR Collaboration said on June 11, 2003:

“This is a very exciting result that clearly indicates we are on the right track to an important scientific discovery, but the case for having created quark-gluon plasma is not yet closed. We have four experiments looking for a number of different ‘signatures’ of this elusive form of extremely hot, dense nuclear matter.” said to the press by Tom Kirk [Kir03].

Tim Hallman sent an email to the whole STAR Collaboration to emphasize [Hal03]: ”The results presented ... _do not_ constitute proof for the existence of the quark-gluon plasma, and that further scientific research is ongoing/needed in this regard.”

The efforts to search for the quark-gluon plasma are continuing ...... I am very fortunate for having been involved in the search as a team member and am proud of contributing a little bit to such a big effort carried out by the entire relativistic heavy ion physics community.

APPENDIX A

Relativistic Kinematics

In this appendix, aspects of relativistic kinematics relevant to heavy ion physics are reviewed. The purpose of this appendix is to provide an introduction for the reader who is new to heavy ion physics, and to set forth the notations and conventions [Won94] used in this dissertation. The following derivations use the convention in which $\hbar = c = 1$. The following conversions are useful: $\hbar c = 197.3$ MeV-fm and $(\hbar c)^2 = 0.3894$ $(\mathrm{GeV})^2$-mb.

A.1 Lorentz Transformation

The energy E and 3-momentum $\mathbf{p}$ of a particle of mass m form the 4-vector $p = (E,\, \mathbf{p})$, whose square $p^2 \equiv E^2 - |\mathbf{p}|^2 = m^2$. The velocity of the particle is $\beta = \mathbf{p}/E$. The energy and momentum $(E^*, \mathbf{p}^*)$ viewed from a frame moving with a velocity β_f are given by

$$\begin{pmatrix} E^* \\ p_{\|}^* \end{pmatrix} = \begin{pmatrix} \gamma_f & -\gamma_f\beta_f \\ -\gamma_f\beta_f & \gamma_f \end{pmatrix} \begin{pmatrix} E \\ p_{\|} \end{pmatrix} ,\; p_T^* = p_T \tag{A.1}$$

where $\gamma_f = 1/\sqrt{1-\beta_f^2}$ and $p_T\,(p_{\|})$ are the components of $\mathbf{p}$ perpendicular (parallel) to β_f. Other 4-vectors, such as the space-time coordinates of events transform in the same manner. The scalar product of two 4-momenta $p_1 \cdot p_2 = E_1E_2 - \mathbf{p}_1 \cdot \mathbf{p}_2$ is invariant (frame independent).

A.2 Kinematic Variables

We consider collision systems with two bodies (particles or nuclei) in the initial state and define the z-axis to coincide with the axis of the collision. For the purposes of presenting single-particle differential multiplicities, it is convenient to describe particle trajectories using kinematic variables which are either Lorentz invariant or transform trivially under Lorentz boosts along this axis.

A.2.1 Transverse Momentum

The momentum components p_x and p_y are unchanged by a boost along z so we define and use the transverse momentum of a particle,

$$p_T = \sqrt{p_x^2 + p_y^2} \tag{A.2}$$

as one such variable. The transverse mass (or transverse energy) of a particle with mass m is defined as

$$m_T = \sqrt{p_T^2 + m^2} \tag{A.3}$$

such that the transverse kinetic energy of the particle is $m_T - m$.

A.2.2 Rapidity

The longitudinal variable most commonly used is rapidity,

$$y = \frac{1}{2} \ln \left(\frac{E + p_z}{E - p_z} \right) \tag{A.4}$$

which has the advantage of being additive under Lorentz transformations along z. This means that under Lorentz transformations along z, differences in rapidity, dy, are invariant and rapidity spectra, dN/dy, translate in y while their shapes are preserved. The expression for rapidity may also be written as

$$y = \ln\left(\frac{E+p_z}{m_T}\right). \tag{A.5}$$

From the above definitions, the relations

$$p_z = m_T \sinh y \tag{A.6}$$

$$E = m_T \cosh y \tag{A.7}$$

are obtained. Dividing these, we have

$$\beta_z = \tanh y \tag{A.8}$$

which is the longitudinal component of the velocity of a particle of rapidity y in the lab. Since rapidity is additive under Lorentz transformations, this suggests a form for the rapidity transformation corresponding to a boost along the z-axis. If a particle has a rapidity y in the lab and we want to know its rapidity y' in a system which has velocity β_z relative to the lab, then:

$$y' = y - \tanh^{-1}\beta_z. \tag{A.9}$$

A.2.3 Pseudorapidity

To characterize the rapidity of a particle, it is necessary to measure two quantities of the particle, such as its energy and its longitudinal momentum, or its particle identification (thus its mass) and the angle of the detected particle relative to the z-

axis. For inclusive charged particles, their masses cannot simply be assigned. If the measurement of particle energy is not available, the rapidities of inclusive particles are unknown. In that case, it is convenient to use pseudo-rapidity

$$\eta = -\ln\left[\tan(\theta/2)\right], \tag{A.10}$$

where θ is the angle between the particle momentum and the z-axis (polar angle). In terms of the momentum, the pseudorapidity can be written as

$$\eta = \frac{1}{2}\ln\left(\frac{|\mathbf{p}| + p_z}{|\mathbf{p}| - p_z}\right). \tag{A.11}$$

A.3 Jacobian Effect

By comparing Eq. A.4 and Eq. A.11, it is easy to see that for massless particles, $\eta = y$, and for particles with large momenta ($\beta \approx 1$), $\eta \approx y$.

Using Eq. A.6 and Eq. A.7, we can express the pseudorapidity η in terms of the rapidity y as

$$\eta = \frac{1}{2}\ln\left(\frac{\sqrt{m_T^2\cosh^2 y - m^2} + m_T\sinh y}{\sqrt{m_T^2\cosh^2 y - m^2} - m_T\sinh y}\right). \tag{A.12}$$

If the particles have a distribution $dN/dydp_T$ in terms of the rapidity, then the distribution in the pseudorapidity is

$$\frac{dN}{d\eta dp_T} = \sqrt{1 - \frac{m^2}{m_T^2\cosh^2 y - m^2}}\,\frac{dN}{dydp_T}. \tag{A.13}$$

The above expression is a Jacobian transformation. It can be seen from Eq. A.13

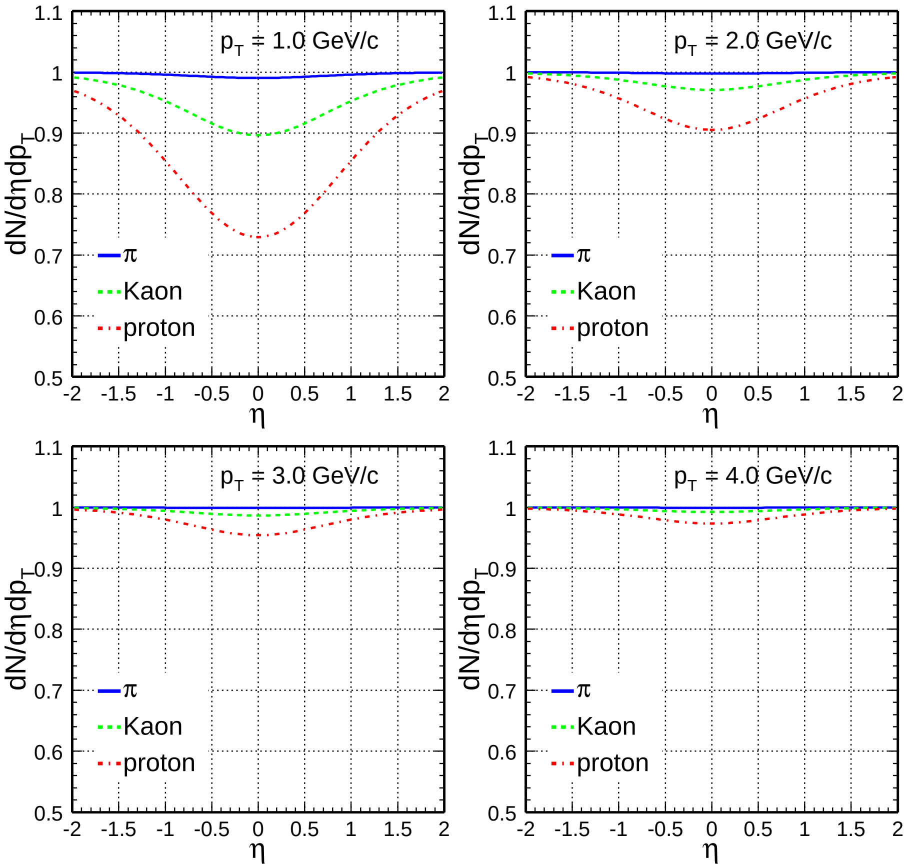

Figure A.1: Effects of the Jacobian transformations from rapidity density distributions to pseudorapidity density distributions for particle pion, kaon, and proton in selected p_T.

that Jacobian factors can be different for various particle types and/or in various p_T. Fig. A.1 demonstrates how large the effect of the Jacobian transformation could be. We assume flat unit $dN/dydp_T$ distributions within $-2 < y < 2$ for particle pion, kaon, and proton in selected $p_T = 1, 2, 3, 4$ GeV/c, then compute the corresponding $dN/d\eta dp_T$ distributions as the curves shown in Fig. A.1. As expected, the largest difference occurs in the most central rapidity region, for the heaviest particle, and at the lowest p_T. When $p_T > 2$ GeV/c the effect is less than 10% even for protons.

A.4 Phase Space and Invariant Yield

The purpose of this section is to come up with a form for differential cross sections and yields that are Lorentz invariant. When we speak of differential yields, we refer to the number of particles emitted into a particular region in momentum space per interaction. It is natural to assume at first that we refer to an object such as d^3N/dp^3. The total yield of a particular particle is the total number of such particles emitted into any point in momentum space per interaction,

$$N = \int \frac{d^3N}{dp^3} d^3p \tag{A.14}$$

which intuitively must be Lorentz invariant. The momentum-space volume element, d^3p, however, is not invariant since the differential momentum element along the direction of a boost between frames transforms as $dp' = \gamma dp$. If we choose to report differential yields in the form d^3N/dp^3, we have to be careful to state the frame in which they were measured. In order to compare the results from different experiments, we would have to explicitly transform the differential yields.

We can avoid such complexities if we find an expression for the differential yield which is manifestly invariant. Effectively this means adopting a Lorentz invariant definition of a momentum-space bin. The momentum-space volume element d^4p is invariant ($dE' = dE/\gamma$), but the set d^4p includes momentum-space bins in which particles are off-shell. Requiring particles to be on-shell, we obtain:

$$\int \delta(p \cdot p - m^2) d^4p = \int \delta(E^2 - |\mathbf{p}|^2 - m^2) d^3p \, dE = \frac{d^3p}{2E}. \tag{A.15}$$

The left hand side of this expression is invariant (the delta function is invariant since its argument is), and we have used $\delta(f(x)) = \sum_i \delta(x - x_i)/|f'(x)|$, where the x_i are the zeros of $f(x)$. We see that the momentum-space volume element d^3p/E is Lorentz invariant.

In any event, the momentum-space volume element d^3p/E is invariant. Therefore, so are the differential yield, Ed^3N/dp^3, and the total yield

$$N = \int E\frac{d^3N}{dp^3}\frac{d^3p}{E}. \tag{A.16}$$

We can write the momentum-space volume element using any variables we like. Using the Jacobian of the transformation between (p_x, p_y, p_z) and (p_T, y, ϕ), the result is:

$$\frac{dp_x dp_y dp_z}{E} = p_T\ dp_T\ dy\ d\phi. \tag{A.17}$$

The expression for total yield is then

$$N = \int \frac{d^3N}{p_T\ dp_T\ dy\ d\phi} p_T\ dp_T\ dy\ d\phi. \tag{A.18}$$

Finally, in many analyses in heavy ion physics, the reaction plane is not measured and the azimuthal distribution can be assumed to be isotropic. The integral in ϕ can thus be performed immediately. If, however, we want to use a form equivalent to Ed^3N/dp^3 for the presentation of different yields, we need to quote the average rather than the sum over ϕ. The expression for total yield becomes:

$$N = \int \frac{d^3N}{2\pi p_T\ dp_T\ dy} 2\pi p_T\ dp_T\ dy. \tag{A.19}$$

We further observe that $p_T\ dp_T = m_T\ dm_T$, so that Equation A.19, with m_T in place of p_T, is an equally valid form for the invariant yield.

The integrand of Equation A.19 is Lorentz invariant for boosts along the collision axis since N is dimensionless and p_T, dp_T, and dy are invariant for such boosts. With

y and p_T defined relative to the boost axis, the expression is invariant for boosts in any direction.

APPENDIX B

The STAR Collaboration

B.1 Author List

STAR Collaboration Author List

J. Adams[3], C. Adler[11], Z. Ahammed[24], C. Allgower[12], J. Amonett[14], B.D. Anderson[14],
M. Anderson[5], D. Arkhipkin[10], G.S. Averichev[9], J. Balewski[12], O. Barannikova[9,24],
L.S. Barnby[14], J. Baudot[13], S. Bekele[21], V.V. Belaga[9], R. Bellwied[33], J. Berger[11],
H. Bichsel[32], A. Billmeier[33], L.C. Bland[2], C.O. Blyth[3], B.E. Bonner[25], M. Botje[20],
A. Boucham[28], A. Brandin[18], A. Bravar[2], R.V. Cadman[1], X.Z. Cai[27], H. Caines[35],
M. Calderón de la Barca Sánchez[2], A. Cardenas[24], J. Carroll[15], J. Castillo[15], M. Castro[33],
D. Cebra[5], P. Chaloupka[21], S. Chattopadhyay[33], Y. Chen[6], S.P. Chernenko[9], M. Cherney[8],
A. Chikanian[35], B. Choi[30], W. Christie[2], J.P. Coffin[13], T.M. Cormier[33], M. Mora Corral[16],
J.G. Cramer[32], H.J. Crawford[4], A.A. Derevschikov[23], L. Didenko[2], T. Dietel[11], J.E. Draper[5],
V.B. Dunin[9], J.C. Dunlop[35], V. Eckardt[16], L.G. Efimov[9], V. Emelianov[18], J. Engelage[4],
G. Eppley[25], B. Erazmus[28], P. Fachini[2], V. Faine[2], J. Faivre[13], R. Fatemi[12], K. Filimonov[15],
E. Finch[35], Y. Fisyak[2], D. Flierl[11], K.J. Foley[2], J. Fu[15,34], C.A. Gagliardi[29], N. Gagunashvili[9],
J. Gans[35], L. Gaudichet[28], M. Germain[13], F. Geurts[25], V. Ghazikhanian[6], O. Grachov[33],
M. Guedon[13], S.M. Guertin[6], E. Gushin[18], T.D. Gutierrez[5], T.J. Hallman[2], D. Hardtke[15],
J.W. Harris[35], M. Heinz[35], T.W. Henry[29], S. Heppelmann[22], T. Herston[24], B. Hippolyte[13],
A. Hirsch[24], E. Hjort[15], G.W. Hoffmann[30], M. Horsley[35], H.Z. Huang[6], T.J. Humanic[21],
G. Igo[6], A. Ishihara[30], P. Jacobs[15], W.W. Jacobs[12], M. Janik[31], I. Johnson[15], P.G. Jones[3],
E.G. Judd[4], S. Kabana[35], M. Kaneta[15], M. Kaplan[7], D. Keane[14], J. Kiryluk[6], A. Kisiel[31],
J. Klay[15], S.R. Klein[15], A. Klyachko[12], T. Kollegger[11], A.S. Konstantinov[23], M. Kopytine[14],
L. Kotchenda[18], A.D. Kovalenko[9], M. Kramer[19], P. Kravtsov[18], K. Krueger[1], C. Kuhn[13],
A.I. Kulikov[9], G.J. Kunde[35], C.L. Kunz[7], R.Kh. Kutuev[10], A.A. Kuznetsov[9],
M.A.C. Lamont[3], J.M. Landgraf[2], S. Lange[11], C.P. Lansdell[30], B. Lasiuk[35], F. Laue[2],
J. Lauret[2], A. Lebedev[2], R. Lednický[9], V.M. Leontiev[23], M.J. LeVine[2], Q. Li[33],
S.J. Lindenbaum[19], M.A. Lisa[21], F. Liu[34], L. Liu[34], Z. Liu[34], Q.J. Liu[32], T. Ljubicic[2],
W.J. Llope[25], H. Long[6], R.S. Longacre[2], M. Lopez-Noriega[21], W.A. Love[2], T. Ludlam[2],
D. Lynn[2], J. Ma[6], Y.G. Ma[27], D. Magestro[21], R. Majka[35], S. Margetis[14], C. Markert[35],

L. Martin[28], J. Marx[15], H.S. Matis[15], Yu.A. Matulenko[23], T.S. McShane[8], F. Meissner[15],
Yu. Melnick[23], A. Meschanin[23], M. Messer[2], M.L. Miller[35], Z. Milosevich[7], N.G. Minaev[23],
J. Mitchell[25], C.F. Moore[30], V. Morozov[15], M.M. de Moura[33], M.G. Munhoz[26], J.M. Nelson[3],
P. Nevski[2], V.A. Nikitin[10], L.V. Nogach[23], B. Norman[14], S.B. Nurushev[23], G. Odyniec[15],
A. Ogawa[2], V. Okorokov[18], M. Oldenburg[16], D. Olson[15], G. Paic[21], S.U. Pandey[33],
Y. Panebratsev[9], S.Y. Panitkin[2], A.I. Pavlinov[33], T. Pawlak[31], V. Perevoztchikov[2], W. Peryt[31],
V.A Petrov[10], R. Picha[5], M. Planinic[12], J. Pluta[31], N. Porile[24], J. Porter[2], A.M. Poskanzer[15],
E. Potrebenikova[9], D. Prindle[32], C. Pruneau[33], J. Putschke[16], G. Rai[15], G. Rakness[12],
O. Ravel[28], R.L. Ray[30], S.V. Razin[9,12], D. Reichhold[24], J.G. Reid[32], G. Renault[28],
F. Retiere[15], A. Ridiger[18], H.G. Ritter[15], J.B. Roberts[25], O.V. Rogachevski[9], J.L. Romero[5],
A. Rose[33], C. Roy[28], V. Rykov[33], I. Sakrejda[15], S. Salur[35], J. Sandweiss[35], I. Savin[10],
J. Schambach[30], R.P. Scharenberg[24], N. Schmitz[16], L.S. Schroeder[15], K. Schweda[15],
J. Seger[8], P. Seyboth[16], E. Shahaliev[9], K.E. Shestermanov[23], S.S. Shimanskii[9], F. Simon[16],
G. Skoro[9], N. Smirnov[35], R. Snellings[20], P. Sorensen[6], J. Sowinski[12], H.M. Spinka[1],
B. Srivastava[24], E.J. Stephenson[12], R. Stock[11], A. Stolpovsky[33], M. Strikhanov[18],
B. Stringfellow[24], C. Struck[11], A.A.P. Suaide[33], E. Sugarbaker[21], C. Suire[2], M. Šumbera[21],
B. Surrow[2], T.J.M. Symons[15], A. Szanto de Toledo[26], P. Szarwas[31], A. Tai[6], J. Takahashi[26],
A.H. Tang[15], D. Thein[6], J.H. Thomas[15], M. Thompson[3], S. Timoshenko[18], M. Tokarev[9],
M.B. Tonjes[17], T.A. Trainor[32], S. Trentalange[6], R.E. Tribble[29], V. Trofimov[18], O. Tsai[6],
T. Ullrich[2], D.G. Underwood[1], G. Van Buren[2], A.M. Vander Molen[17], A.N. Vasiliev[23],
S.E. Vigdor[12], S.A. Voloshin[33], M. Vznuzdaev[18], F. Wang[24], Y. Wang[30], H. Ward[30],
J.W. Watson[14], R. Wells[21], G.D. Westfall[17], C. Whitten Jr. [6], H. Wieman[15], R. Willson[21],
S.W. Wissink[12], R. Witt[35], J. Wood[6], N. Xu[15], Z. Xu[2], A.E. Yakutin[23], E. Yamamoto[15],
J. Yang[6], P. Yepes[25], V.I. Yurevich[9], Y.V. Zanevski[9], I. Zborovský[9], H. Zhang[35],
W.M. Zhang[14], R. Zoulkarneev[10], J. Zoulkarneeva[10], A.N. Zubarev[9]

(STAR Collaboration)

[1]Argonne National Laboratory, Argonne, Illinois 60439
[2]Brookhaven National Laboratory, Upton, New York 11973
[3]University of Birmingham, Birmingham, United Kingdom
[4]University of California, Berkeley, California 94720
[5]University of California, Davis, California 95616
[6]University of California, Los Angeles, California 90095
[7]Carnegie Mellon University, Pittsburgh, Pennsylvania 15213
[8]Creighton University, Omaha, Nebraska 68178
[9]Laboratoryfor High Energy (JINR), Dubna, Russia
[10]Particle Physics Laboratory (JINR), Dubna, Russia
[11]University of Frankfurt, Frankfurt, Germany
[12]Indiana University, Bloomington, Indiana 47408
[13]Institut de Recherches Subatomiques, Strasbourg, France
[14]Kent State University, Kent, Ohio 44242
[15]LawrenceBerkeley National Laboratory, Berkeley, California 94720
[16]Max-Planck-Institut fuer Physik, Munich, Germany

[17]Michigan State University, East Lansing, Michigan 48825
[18]Moscow Engineering Physics Institute, Moscow Russia
[19]City College of New York, New York City, New York 10031
[20]NIKHEF, Amsterdam, The Netherlands
[21]Ohio State University, Columbus, Ohio 43210
[22]Pennsylvania State University, University Park, Pennsylvania 16802
[23]Institute of High Energy Physics, Protvino, Russia
[24]Purdue University, West Lafayette, Indiana 47907
[25]Rice University, Houston, Texas 77251
[26]Universidade de Sao Paulo, Sao Paulo, Brazil
[27]Shanghai Institute of Nuclear Research, Shanghai 201800, P.R. China
[28]SUBATECH, Nantes, France
[29]Texas A&M University, College Station, Texas 77843
[30]University of Texas, Austin, Texas 78712
[31]Warsaw University of Technology, Warsaw, Poland
[32]University of Washington, Seattle, Washington 98195
[33]Wayne State University, Detroit, Michigan 48201
[34]Institute of Particle Physics, CCNU (HZNU), Wuhan, 430079 China
[35]Yale University, New Haven, Connecticut 06520

B.2 Publications

STAR Collaboration Scientific Journal Publications

1. K.H. Ackermann *et al.*, STAR Collab., Phys. Rew. Lett. **86**, 402 (2001), Elliptic Flow in Au + Au Collisions at $\sqrt{s_{NN}} = 130$ GeV.

2. C. Adler *et al.*, STAR Collab., Phys. Rew. Lett. **86**, 4778 (2001), Midrapidity Antiproton-to-Proton Ratio from Au + Au Collisions at $\sqrt{s_{NN}} = 130$ GeV.

3. C. Adler *et al.*, STAR Collab., Phys. Rew. Lett. **87**, 082301 (2001), Pion Interferometry of $\sqrt{s_{NN}} = 130$ GeV Au + Au Collisions at RHIC.

4. C. Adler *et al.*, STAR Collab., Phys. Rew. Lett. **87**, 112303 (2001), Multiplicity Distribution and Spectra of Negatively Charged Hadrons in Au + Au Collisions at $\sqrt{s_{NN}} = 130$ GeV.

5. C. Adler *et al.*, STAR Collab., Phys. Rew. Lett. **87**, 182301 (2001), Identified Particle Elliptic Flow in Au + Au Collisions at $\sqrt{s_{NN}} = 130$ GeV.

6. C. Adler *et al.*, STAR Collab., Phys. Rew. Lett. **87**, 262301 (2001), $\overline{d}$ and $^{3}\overline{\mathrm{H}e}$ Production in $\sqrt{s_{NN}} = 130$ GeV Au + Au Collisions.

7. C. Adler *et al.*, STAR Collab., Phys. Rew. Lett. **87**, 262302 (2001), Measurement of Inclusive Antiprotons from Au + Au Collisions at $\sqrt{s_{NN}} = 130$ GeV.

8. C. Adler *et al.*, STAR Collab., Nucl. Phys. A **698**, 64c (2002), Results from the STAR Experiment.

9. C. Adler *et al.*, STAR Collab., J. Phys. G **28**, 1535 (2002),
   Strangeness in Au + Au collisions at $\sqrt{s_{NN}} = 130$ GeV observed with the STAR detector.

10. C. Adler *et al.*, STAR Collab., Phys. Rew. C **65**, 041901(R) (2002),
    Midrapidity Φ production in Au + Au collisions at $\sqrt{s_{NN}} = 130$ GeV.

11. C. Adler *et al.*, STAR Collab., Phys. Rew. Lett. **89**, 092301 (2002),
    Midrapidity Λ and $\overline{\Lambda}$ Production in Au + Au Collisions at $\sqrt{s_{NN}} = 130$ GeV.

12. C. Adler *et al.*, STAR Collab., Phys. Rew. Lett. **89**, 132301 (2002),
    Azimuthal Anisotropy of K_S^0 and $\Lambda + \overline{\Lambda}$ Production at Midrapidity from Au + Au Collisions at $\sqrt{s_{NN}} = 130$ GeV.

13. C. Adler *et al.*, STAR Collab., Phys. Rew. C **66**, 034904 (2002),
    Elliptic flow from two- and four-particle correlations in Au + Au collisions at $\sqrt{s_{NN}} = 130$ GeV.

14. C. Adler *et al.*, STAR Collab., Phys. Rew. Lett. **89**, 202301 (2002),
    Centrality Dependence of High-p_T Hadron Suppression in Au + Au Collisions at $\sqrt{s_{NN}} = 130$ GeV.

15. C. Adler *et al.*, STAR Collab., Phys. Rew. Lett. **89**, 272303 (2002),
    Coherent ρ^0 Production in Ultraperipheral Heavy-Ion Collisions.

16. C. Adler *et al.*, STAR Collab., Phys. Rew. C **66**, 061901(R) (2002),
    $K^*(892)^0$ production in relativistic heavy ion collisions at $\sqrt{s_{NN}} = 130$ GeV.

17. C. Adler *et al.*, STAR Collab., Phys. Rew. Lett. **90**, 032301 (2003),
    Azimuthal Anisotropy and Correlations in the Hard Scattering Regime at RHIC.

18. C. Adler *et al.*, STAR Collab., Phys. Rew. Lett. **90**, 082302 (2003),

Disappearance of Back-To-Back High-p_T Hadron Correlations in Central Au + Au Collisions at $\sqrt{s_{NN}} = 200$ GeV.

19. J. Adams *et al.*, STAR Collab., Phys. Rew. Lett. **90**, 172301 (2003), Narrowing of the Balance Function with Centrality in Au + Au Collisions at $\sqrt{s_{NN}} = 130$ GeV.

REFERENCES

[Abe89] F. Abe et al. *Phys. Rev. Lett.*, **62**:613, 1989.

[Abe90] F. Abe et al. *Phys. Rev. D*, **41**:2330, 1990.

[Acc02] A. Accardi. *hep-ph/0212148,* 2002.

[Ack99] K.H. Ackermann et al. *Nucl. Phys.*, **A661**:681c, 1999.

[Ack03a] K.H. Ackermann et al. *Nucl. Instrum. Meth. A*, **499**:624, 2003.

[Ack03b] K.H. Ackermann et al. *Nucl. Instrum. Meth. A*, **499**:713, 2003.

[Ada] J. Adams et al. "Centrality and pseudorapidity dependence of charged hadron production at moderate p_T in Au + Au collisions at $\sqrt{s_{NN}} = 130$ GeV." to be submitted to Phys. Rev. C.

[Ada03a] J. Adams et al. *nucl-ex/0305015*, 2003.

[Ada03b] J. Adams et al. *nucl-ex/0306024*, 2003.

[Ada03c] J. Adams et al. *nucl-ex/0306007,* 2003.

[Adc01] K. Adcox et al. *Phys. Rev. Lett.*, **86**:3500, 2001.

[Adc02] K. Adcox et al. *Phys. Rev. Lett.*, **88**:242301, 2002.

[Adc03] K. Adcox et al. *Phys. Lett. B*, **561**:82, 2003.

[Adl01a] C. Adler et al. *Nucl. Instrum. Meth. A*, **470**:488, 2001.

[Adl01b] C. Adler et al. *Phys. Rev. Lett.*, **87**:112303, 2001.

[Adl01c] C. Adler et al. *Phys. Rev. Lett.*, **87**:262302, 2001.

[Adl02a] C. Adler et al. *Phys. Rev. Lett.*, **89**:202301, 2002.

[Adl02b] C. Adler et al. *Phys. Rev. Lett.*, **89**:092301, 2002.

[Adl02c] C. Adler et al. *nucl-ex/0206008,* 2002.

[Adl03] C. Adler et al. *Nucl. Instrum. Meth. A*, **499**:778, 2003.

[Aga00] G. Agakishiev et al. *hep-ex/0003012,* 2000.

[Agg98] M.M. Aggarwal et al. *Phys. Rev. Lett.*, **81**:4087, 1998.

[AGP93] B. Andersson, G. Gustafson, and H. Pi. *Z. Phys. C*, **57**:485, 1993.

[Alb90] C. Albajar et al. *Nucl. Phys.*, **B335**:261, 1990.

[All03] C.E. Allgower et al. *Nucl. Instrum. Meth. A*, **499**:740, 2003.

[Aln86] G.J. Alner et al. *Z. Phys. C*, **33**:1, 1986.

[Alp75] B. Alper et al. *Nucl. Phys.*, **B100**:237, 1975.

[And83] B. Andersson et al. *Phys. Rep.*, **97**:31, 1983.

[And03a] M. Anderson et al. *Nucl. Instrum. Meth. A*, **499**:659, 2003.

[And03b] M. Anderson et al. *Nucl. Instrum. Meth. A*, **499**:679, 2003.

[Ant79] D. Antreasyan et al. *Phys. Rev. D*, **19**:764, 1979.

[App79] J.A. Appel et al. *Phys. Rev. D*, **20**:53, 1979.

[App99] H. Appelshauser et al. *Phys. Rev. Lett.*, **82**:2471, 1999.

[Arn83] G. Arnison et al. *Phys. Lett. B*, **123**:115, 1983.

[Arn90] M. Arneodo et al. *Nucl. Phys.*, **B333**:1, 1990.

[Bac02] B. Back et al. *Phys. Rev. C*, **65**:061901R, 2002.

[Bai95] R. Baier et al. *Phys. Lett. B*, **345**:277, 1995.

[Ban82] M. Banner et al. *Phys. Lett. B*, **118**:203, 1982.

[Bed03] M. Beddo et al. *Nucl. Instrum. Meth. A*, **499**:725, 2003.

[Bel03] R. Bellwied et al. *Nucl. Instrum. Meth. A*, **499**:640, 2003.

[Ber03] F. Bergsma et al. *Nucl. Instrum. Meth. A*, **499**:633, 2003.

[BFG01] L. Bourhis, M. Fontannaz, J.P. Guillet, and M. Werlen. *Eur. Phys. J.*, **C19**:89, 2001.

[Bie03] F.S. Bieser et al. *Nucl. Instrum. Meth. A*, **499**:766, 2003.

[BKK95] J. Binnewies, B.A. Kniehl, and G. Kramer. *Phys. Rev. D*, **52**:4947, 1995.

[BKW03] R. Baier, A. Kovner, and U.A. Wiedemann. *hep-ph/0305265*, 2003.

[Boc96] G. Bocquet et al. *Phys. Lett. B*, **336**:434, 1996.

[Bra03] A. Braem et al. *Nucl. Instrum. Meth. A*, **499**:720, 2003.

[BSZ00] R. Baier, D. Schiff, and B.G. Zakharov. *Annu. Rev. Nucl. Part. Sci.*, **50**:37, 2000.

[Cha79] D. Chaney et al. *Phys. Rev. D*, **19**:3210, 1979.

[Cle86] J. Cleymans et al. *Phys. Rep.*, **130**:217, 1986.

[Col92] The STAR Collaboration. "Conceptual Design Report for the Solonoid Tracker at RHIC." Technical report, STAR Collaboration, 1992.

[Cro75] J.W. Cronin et al. *Phys. Rev. D*, **11**:3105, 1975.

[DO84] D.W. Duke and J.F. Owens. *Phys. Rev. D*, **30**:50, 1984.

[EKS99] K.J. Eskola, V.J. Kolhinen, and C.A. Salgado. *Eur. Phys. J.*, **C9**:61, 1999.

[FMN03] R.J. Fries, B. Müller, C. Nonaka, and S.A. Bass. *nucl-th/0301087*, 2003.

[Fri83] H.J. Frisch et al. *Phys. Rev. D*, **27**:1001, 1983.

[Gar77] D.A. Garbutt et al. *Phys. Lett. B*, **67**:355, 1977.

[GGX03] K. Gallmeister, C. Greiner, and Z. Xu. *Phys. Rev. C*, **67**:044905, 2003.

[GLV00] M. Gyulassy, P. Levai, and I. Vitev. *Phys. Rev. Lett.*, **85**:5535, 2000.

[GP90] M. Gyulassy and M. Plümer. *Phys. Lett. B*, **243**:432, 1990.

[GRS01] M. Glueck, E. Reya, M. Stratmann, and W. Vogelsang. *Phys. Rev. D*, **63**:094005, 2001.

[GW94] M. Gyulassy and X.N. Wang. *Comput. Phys. Commun.*, **83**:307, 1994.

[Hag02] K. Hagiwara et al. *Phys. Rev. D*, **66**:010001, 2002.

[Hal03] T. Hallman. "Press-kit information." URL: http://lists.bnl.gov/mailman/listinfo/starmail-l, June 11, 2003.

[HKM01] M. Hirai, S. Kumano, and M. Miyama. *Phys. Rev. D*, **64**:034003, 2001.

[JI96] P. Jacobs and D. Irmscher. "GSTAR: A Geant-based detector simulation chain for STAR." *STAR Note 235*, 1996.

[JJS03] S. Jeon, J. Jalilian-Marian, and I. Sarcevic. *Phys. Lett. B*, **562**:45, 2003.

[Kir03] T. Kirk. “News Release Number 03 – 49 by Brookhaven National Laboratory.” URL: http://www.bnl.gov/bnlweb/pubaf/pr/2003/ bnlpr061103.htm, June 11, 2003.

[KKP00] B.A. Kniehl, G. Kramer, and B. Pötter. *Nucl. Phys.*, **B582**:514, 2000.

[KLM03] D. Kharzeev, E. Levin, and L. McLerran. *Phys. Lett. B*, **561**:93, 2003.

[KN01] D. Kharzeev and M. Nardi. *Phys. Lett. B*, **507**:121, 2001.

[Kot03] L. Kotchenda et al. *Nucl. Instrum. Meth. A*, **499**:703, 2003.

[Kre00] S. Kretzer. *Phys. Rev. D*, **62**:054001, 2000.

[Lan03] J.M. Landgraf et al. *Nucl. Instrum. Meth. A*, **499**:762, 2003.

[Lik92] D. Liko. “Track Fitting in the STAR Detector using the Kalman Filter Method.” *STAR Note 87*, 1992.

[Lon02] Hui Long. “Mid-rapidity Λ and $\overline{\Lambda}$ Production in Au+Au Collisions at the Relativistic Heavy Ion Collider.” *Ph.D. Thesis, UCLA*, 2002.

[LW95] G.D. Lafferty and T.R. Wyatt. *Nucl. Instrum. Meth. A*, **355**:541, 1995.

[LW02] S.Y. Li and X.N. Wang. *Phys. Lett. B*, **527**:85, 2002.

[M03] Berndt Müller. *nucl-th/0208038*, 2003.

[MC92] S. Margetis and D. Cebra. “Main Vertex Reconstruction in STAR.” *STAR Note 89*, 1992.

[MRS02] A.D. Martin, R.G. Roberts, W.J. Stirling, and R.S. Thorne. *Eur. Phys. J.*, **C23**:73, 2002.

[MS94] J.T. Mitchell and I.M. Sakrejda. “Tracking for the STAR TPC: Documentation and User’s Guide.” *STAR Note 190*, 1994.

[Owe78] J.F. Owens et al. *Phys. Rev. D*, **18**:1501, 1978.

[Pro] CERN RD44 Project. URL: http://wwwinfo.cern.ch/asd/geant/ geant4_public/G4UsersDocuments/Welcome/IntroductionToGeant4/ html/introductionToGeant4.html.

[Pum02] J. Pumplin et al. *hep-ph/0201195*, 2002.

[PY01] A. Polleri and F. Yuan. *nucl-th/0108056*, 2001.

[Ray99] L. Ray. “EVR: Event Vertex Reconstruction.” URL: http://www.star.bnl.gov/∼ray/evr/doc, 1999.

[Sa02] B.H. Sa et al. *Phys. Lett. B*, **537**:268, 2002.

[Sj01] T. Sjöstand et al. *Comput. Phys. Commun.*, **135**:238, 2001.

[VG02] I. Vitev and M. Gyulassy. *Phys. Rev. Lett.*, **89**:252301, 2002.

[Vit03] I. Vitev. *Phys. Lett. B*, **562**:36, 2003.

[Wan98] Xin-Nian Wang. *Phys. Rev. C*, **58**:2321, 1998.

[Wan00] Xin-Nian Wang. *Phys. Rev. C*, **61**:064910, 2000.

[Wan02a] Xin-Nian Wang. private communication, 2002.

[Wan02b] X.N. Wang. *Nucl. Phys.*, **A698**:296, 2002.

[Wan03] Xin-Nian Wang. *nucl-th/0305010*, 2003.

[Wer93] K. Werner. *Phys. Rep.*, **232**:87, 1993.

[WG91] X.N. Wang and M. Gyulassy. *Phys. Rev. D*, **44**:3501, 1991.

[WG92] X.N. Wang and M. Gyulassy. *Phys. Rev. Lett.*, **68**:1480, 1992.

[Won94] Cheuk-Yin Wong. *Introduction to High-Energy Heavy-Ion Collisions*. World Scientific Publishing Co. Pte. Ltd., Singapore, first edition, 1994.

[WW01a] E. Wang and X.N. Wang. *Phys. Rev. C*, **64**:034901, 2001.

[WW01b] E. Wang and X.N. Wang. *Phys. Rev. Lett.*, **87**:142301, 2001.

[WW02] E. Wang and X.N. Wang. *Phys. Rev. Lett.*, **89**:162301, 2002.